

Heteroatom Doped Materials for Li-S Battery Applications

by

Mr. Kumar S
10CC15J26019

A thesis submitted to the
Academy of Scientific & Innovative Research
for the award of the degree of
DOCTOR OF PHILOSOPHY

in

SCIENCE

Under the supervision of

Dr. Kothandam Krishnamoorthy



CSIR- National Chemical Laboratory, Pune



Academy of Scientific and Innovative Research
AcSIR Headquarters, CSIR-HRDC campus
Sector 19, Kamla Nehru Nagar
Ghaziabad, U.P. – 201 002, India

November-2022

Certificate

This is to certify that the work incorporated in this Ph.D. thesis entitled “**Heteroatom Doped Materials for Li-S Battery Applications**” submitted by **Mr. Kumar S** to Academy of Scientific and Innovative Research (AcSIR) in partial fulfillment of the requirements for the award of the Degree of *Doctor of Philosophy in Science*, embodies original research work under my guidance. We, further certify that this work has not been submitted to any other University or Institutions in part for the award of any degree or diploma. Research material(s) obtained from other source(s) and used in this research work has/have duly acknowledged in the thesis. Image(s), illustration(s), figure(s), table(s) etc., used in the thesis from other source(s), have also been duly cited and acknowledged.

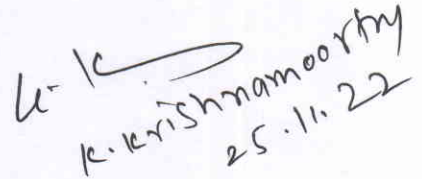


(Signature of the Student)

Name with date

Kumar S

25-11-2022



K. Krishnamoorthy
25.11.22

Signature of the Supervisor

Name with date

Statements of Academic Integrity

I, Kumar S, a Ph.D. student of the Academy of Scientific and Innovative Research (AcSIR) with Registration No. **10CC15J26019**, hereby undertake that, the thesis entitled “**Heteroatom Doped Materials for Li-S Battery Applications**” has been prepared by me and that the document reports original work carried out by me and is free of any plagiarism in compliance with the UGC Regulations on “*Promotion of Academic Integrity and Prevention of Plagiarism in Higher Educational Institutions (2018)*” and the CSIR Guidelines for “*Ethics in Research and in Governance (2020)*”.

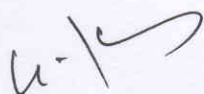


Date: 25-11-2022

Signature of the Student

Place: Pune

It is hereby certified that the work done by the student, under my supervision, is plagiarism-free in accordance with the UGC Regulations on “*Promotion of Academic Integrity and Prevention of Plagiarism in Higher Educational Institutions (2018)*” and the CSIR Guidelines for “*Ethics in Research and in Governance (2020)*”.



Signature of the Supervisor

Name: Dr. K. Krishnamoorthy

Date: 25-11-2022

Place: Pune

Dedicated to My Mother, Teachers,

&

All Well Wishers

Table of contents

List of Schemes	vii
List of Figures	viii
List of Tables	xi
List of Abbreviations	xii
1 Li-S Battery: An Overview, Working Principles, and Applications	1
1.1 Introduction.....	3
1.2 Working Principles of Li-S batteries	4
1.3 Challenges of Li-S batteries.....	5
1.3.1 Shuttle effect.....	6
1.3.2 Self-Discharge	6
1.4 Components of Li-S batteries	6
1.4.1 Cathode.....	6
1.4.1.1 Sulfur-Carbon composite materials.....	7
1.4.1.2 Sulfur-Inorganic composite materials	9
1.4.1.3 Organic Framework/Sulfur composite	11
1.4.1.4 MXene/Sulfur composites.....	11
1.4.1.5 Polymer/Sulfur composites	11
1.4.1.6 Sulfur.....	12
1.4.1.7 Binder.....	13
1.4.2 Anode.....	13
1.4.3 Electrolytes	14
1.4.4 Additives.....	16
1.4.5 Separator.....	16
1.5 References.....	17
2 Concurrent Polyvalent Interaction and Electrocatalysis to Improve Lithium-Sulfur Battery Performance	31

Table of contents

2.1	Introduction.....	33
2.2	Experimental Section.....	35
2.2.1	Materials	35
2.2.2	Instrumentations	36
2.2.3	Synthesis.....	36
2.3	Results and Discussion	37
2.3.1	Raman spectroscopy	37
2.3.2	X-ray diffraction analysis	39
2.3.3	X-ray photoelectron spectroscopy	39
2.3.4	Scanning electron microscope	40
2.3.5	Transmission electron microscope	42
2.3.6	Thermogravimetric analysis	43
2.3.7	Polysulfide adsorption test.....	43
2.4	Electrochemical studies	45
2.4.1	Electrode preparation.....	45
2.4.2	Li-S cell fabrication	45
2.4.3	Cyclic voltammetry	45
2.4.4	Charge-discharge experiments.....	46
2.4.5	Symmetric cell assembly and Tests.....	50
2.5	Conclusion	52
2.6	References.....	52
3	Can metal cations electrocatalyze sulfur redox reaction and suppress polysulfide shuttle?	57
3.1	Introduction.....	59
3.2	Experimental Section.....	60
3.2.1	Materials	60
3.2.2	Instrumentations	60

3.2.3 Synthesis	60
3.3 Results and Discussion	61
3.3.1 Raman spectroscopy	61
3.3.2 X-ray diffraction analysis	62
3.3.3 X-ray photoelectron spectroscopy	62
3.3.4 Transmission electron microscope	64
3.3.5 Thermogravimetric analysis	65
3.3.6 Polysulfide adsorption test.....	66
3.4 Electrochemical studies	67
3.4.1 Electrode preparation.....	67
3.4.2 Li-S cell fabrication	67
3.4.3 Cyclic voltammetry	67
3.4.4 Charge-discharge experiments.....	68
3.4.5 Symmetric cell assembly and Tests	72
3.5 Conclusion	73
3.6 References.....	73
4 Exploring the catalytic effect of Transition Metal Decorated Carbonized Phthalocyanine materials for Li-S Battery	79
4.1 Introduction.....	81
4.2 Experimental Section	82
4.2.1 Materials	82
4.2.2 Instrumentations	82
4.2.3 Synthesis	83
4.3 Results and Discussion	83
4.3.1 X-ray diffraction analysis	83
4.3.2 X-ray photoelectron spectroscopy	84
4.3.3 Scanning electron microscope	86

Table of contents

4.3.4 Thermogravimetric analysis	88
4.4 Electrochemical studies	88
4.4.1 Electrode preparation.....	88
4.4.2 Li-S cell fabrication	88
4.4.3 Cyclic voltammetry	89
4.4.4 Charge-discharge experiments.....	90
4.5 Conclusion	92
4.6 References.....	92
5 Summary and Future Directions.....	97
5.1 Summary.....	99
5.2 Future Directions	100
ABSTRACT.....	101

List of Schemes

Scheme 2.1. Cartoon showing the steps involved in the preparation of DLC-G.....	34
Scheme 2.2. Chemical Structures of exfoliators (Anthracene, Melamine, 3-Thiopheneacetic acid, Ni(II) phthalocyanine) and DPP-12.	34
Scheme 4.1. Structures of Metal-Phthalocyanines (Fe, Co, and Ni).	82

List of Figures

Figure 1.1. Ragone plot with respect to gravimetric and volumetric energy densities.[8]	4
Figure 1.2. Schematic diagram of Li-S cell (a), and typical charge-discharge profile with the state of Sulfur/LiPSs.[11].....	5
Figure 2.1. Raman spectra showing D, D', G and 2D bands for Graphite, G-A, G-M and G-M-T.	38
Figure 2.2. XRD pattern for Graphite, G-A, G-M and G-M-T.....	39
Figure 2.3. XPS spectra of pristine graphite, few-layer graphenes G-A, G-M and G-M-T (a), deconvoluted peaks of the Nitrogen region for G-M and G-M-T (b), and Sulfur deconvolution curves of G-M-T (c).....	40
Figure 2.4. XPS survey of G-NP (a), deconvolution peak of Carbon (b), Nitrogen (c) and Nickel (d).....	40
Figure 2.5. SEM imaging of G-A (a), mapping element (Carbon) on the same spot (b) and mapping of element Carbon (c). Scale bar is 20 μm	41
Figure 2.6. SEM imaging of G-M (a), overall mapping elements (Carbon and Nitrogen) on the same spot (b), mapping of corresponding elements C(c) and N(d). Scale bar is 20 μm	41
Figure 2.7. SEM imaging of G-M-T (a), overall mapping elements (Carbon, Nitrogen and Sulfur) on the same spot (b), mapping of corresponding elements C(c), N(d), S(e). Scale bar is 20 μm	41
Figure 2.8. SEM imaging of G-NP (a), mapping of corresponding elements C(b), N(c) and Ni(d). Scale bar is 20 μm	42
Figure 2.9. TEM image of Pristine Graphite (a) (scale bar is 20 nm), TEM images showing the few layers of graphene G-M (b), G-M-T (c), G-M-T/S (d), and G-NP (e).	43
Figure 2.10. TGA indicating the sulfur loading in G-A, G-M and G-M-T, (a) and G-NP (b).43	
Figure 2.11. UV-Vis spectra of Li_2S_6 solution in absence (Blank) and presence of G-A, G-M, G-M-T (a), and G-NP (b). The insert photographs show the color of Blank Li_2S_6 solution and the supernatant of adsorbed Li_2S_6 on DLC-Gs.	44
Figure 2.12. Cyclic voltammogram of Li-S battery comprising G-A, G-M, G-M-T (a), and G-NP (b) with scan rate of 0.1 mV s^{-1}	46
Figure 2.13. Charge-Discharge curves at 0.2 h^{-1} showing specific capacity fading while using G-A (a), G-M (b) in Li-S battery electrode, and Rate performance study of Li-S cell using G-M (c).....	47

Figure 2.14. Charge-discharge profile at 0.2 h⁻¹ rate (a), and Rate performance study (b) of Li-S cell comprising G-M-T.48

Figure 2.15. Charge-discharge profile at 0.2 h⁻¹ (a), and rate performance of Li-S cell comprising G-NP (b).....49

Figure 2.16. Plot showing variation in specific capacity for 500 cycles 0.2 h⁻¹ (a), and Ragone plot of Li-S batteries with various DLC-Gs (b).50

Figure 2.17. Cyclicvoltammograms of symmetric cells comprising G-A, G-M, G-M-T (a), and G-NP (b). The dashed plots are the experiments carried out without Li₂S₆.50

Figure 3.1. Raman spectra showing D, D', G and 2D bands of Graphite, G-Co and G-Ni.62

Figure 3.2. XRD pattern for Graphite, G-Co and G-Ni.62

Figure 3.3. XPS spectra of G-Co (a), deconvolution curves of C1s (b), Co2p (c) and Cl2p (d) spectra.63

Figure 3.4. XPS survey of G-Ni (a), C1s (b) Ni2p (c) S2p (d) and O1s (e) spectra.64

Figure 3.5. TEM imaging of Graphite (a) G-Co (b) and G-Ni (c).....65

Figure 3.6. TEM imaging and mapping of G-Co and (a) TEM imaging and mapping of G-Ni (b).....65

Figure 3.7. Thermogravimetric analysis of G-Co/S and G-Ni/S.66

Figure 3.8. Chemical structure of Diketopyrrolopyrrole (DPP).66

Figure 3.9. UV-Vis spectra of Li₂S₆ solution (Blank) with Graphite, G-Co and G-Ni. The insert shows the de-coloration of the solution due to attraction between Li₂S₆ and G-Ni.67

Figure 3.10. Cyclic voltammogram of Li-S cell with scan rate of 0.1 mV/s using G-Co/S and G-Ni/S.68

Figure 3.11. Charge/discharge profile of Li-S cell with G-Co/S at 0.1 C rate (a) and first cycle at various rates (0.1 C, 0.2 C, 0.5 C, 1 C and 2 C) (b), Rate performance studies (c), and percentage retention with respect to various C rates of Li-S battery using G-Co (d).....69

Figure 3.12. Charge/discharge profile of Li-S cell using G-Ni at 0.1 C rate for 100 cycles (a) and first cycle of different rates (0.1 C, 0.2 C, 0.5 C, 1 C and 2 C) (b), Rate performance studies of Li/S cell using G-Ni/S (c) Charge/Discharge profiles of Li-S cells at 500th cycle using G-Ni/S with different rates (0.1 C, 0.2 C and 2 C) (d).....70

Figure 3.13. Charge-discharge profile at 0.2 h⁻¹ (a), and rate performance of Li-S cell comprising G-NP (b).....71

Figure 3.14. Ragone plot for Li-S cell using G-Co and G-Ni comprised sulfur electrodes. ...72

Figure 3.15. Cyclicvoltmmogram of symmetric cells comprising G-A, G-M, G-M-T (a), and G-NP (b). The dashed plots are the experiments carried out without Li₂S₆.73

Figure 4.1. XRD pattern for Fe-Ph, Co-Ph, and Ni-Ph powders (a), and carbonized Fe-Ph, Co-Ph, and Ni-Ph samples.84

Figure 4.2. XPS survey of Fe-Ph (a), deconvolution curves of C1s (b), N1s (c), and Fe2p (d) spectra.85

Figure 4.3. XPS survey of Co-Ph (a), deconvolution curves of C1s (b), N1s (c), and Co2p (d) spectra.85

Figure 4.4. XPS survey of Ni-Ph (a), deconvolution curves of C1s (b), N1s (c), and Ni2p (d) spectra.86

Figure 4.5. FE-SEM imaging of Fe-Ph and mapping of C, N, and Fe.86

Figure 4.6. FE-SEM imaging of Co-Ph and mapping of C, N, and Co.87

Figure 4.7. FE-SEM imaging of Ni-Ph and mapping of C, N, and Ni.87

Figure 4.8. Energy-dispersive X-ray spectroscopy (EDAX) analysis of samples Fe-Ph (a), Co-Ph (b), and Ni-Ph (c).87

Figure 4.9. Thermogravimetric analysis of Fe-Ph/S, Co-Ph/S, and Ni-Ph/S.....88

Figure 4.10. Cyclic voltammogram of Li-S cells comprising Fe-Ph/S (a), Co-Ph/S (b), and Ni-Ph/S (c) with a scan rate of 0.1 mV/s.....89

Figure 4.11. Charge/discharge profile of Li-S cells comprised using Fe-Ph/S (a), Co-Ph/S (b), and Ni-Ph/S (c) at 0.5 C rate.....90

Figure 4.12. Charge/discharge profiles of Li-S cells using Ni-Ph/S-based material at the current rates of 0.1 C (a), 0.2 C (b), 1.0 C (c), and 2.0 C (d).91

Figure 4.13. Cyclic performances of Li-S cells at 0.5 C, using Fe-Ph/S, Co-Ph/S, and Ni-Ph/S based electrodes.91

List of Tables

Table 2.1. Milling conditions and obtained I_D/I_G and I_D/I_D' from Raman spectra and d-spacing from XRD pattern	38
Table 2.2. Li-S battery metrics of various materials.....	51
Table 4.1. Chemical compositions of elements in M-Phs obtained from EDAX analysis.....	87

List of Abbreviations

2D	Two-dimensional
3D	Three dimensional
AFG	Amino functional group
CNF	Carbon nanofiber
CNT	Carbon nanotube
COF	Covalent organic framework
CVs	Cyclicvoltammograms
D	Pore size
DLC-G	Doped layer comprising Graphene
DME	1,2-dimethoxy ethane
DMF	Dimethylformamide
DOL	1,3-dioxolane
DPP	Diketopyrrolopyrrole
E/S	Electrolyte/Solvent
EDAX	Energy dispersive X-ray analysis
EDAX	Energy-dispersive X-ray spectroscopy analysis
E-SEM	Environmental Scanning electron microscope
EV	Electric vehicles
F	Faraday constant
FE-SEM	Field emission Scanning electron microscope
FG	Functionalized Graphene
G-Co	Cobalt ion doped graphene
G-M	N-doped layer comprising graphene
G-M-T	N, S-doped layer comprising graphene
G-Ni	Nickel ion doped graphene
G-NP	Ni, N-doped layer comprising graphene
GO	Graphene oxide
HCl	Hydrochloric acid
HR-TEM	High resolution Transmission electron microscope
i_p	Peak current intensity

LCO	Lithium Cobalt oxide
Li	Lithium
LIBs	Li-ion batteries
LiPAA	Lithium polyacrylate
LiPSs	Lithium polysulfides
Li-S	Lithium-Sulfur
LiTFS	Lithium trifluoromethanesulfonate
LiTFSI	Bis(trifluoromethane)sulfonimide lithium salt
MOF	Metal-organic framework
M-Phs	Metal-Phthalocyanines
MWCNTs	Multi-walled carbon nanotubes
Ni-Cd	Nickel-Cadmium
Ni-MH	Nickel-Metal hydride
Ni-Ph	Nickel Phthalocyanine
NMP	N-Methyl-2-pyrrolidone
NPs	Nanoparticles
PANI	Polyaniline
PE	Polyethylene
PEG	Poly(ethylene glycol)
PEGDME	Polyethylene glycol dimethyl ether
PEO	Poly(ethylene oxide)
PP	Polypropylene
PTFE	Polytetrafluoroethylene
PVDF	Poly(vinylidene fluoride)
PVP	Polyvinylpyrrolidone
Q	Theoretical capacity
RPM	Revolutions per minute
RT	Room temperature
SACs	Single-atom catalysts
SEI	Solid electrolyte interface
SHE	Standard hydrogen electrode
Si	Silicon
TAA	3-Thiophene acetic acid

Table of contents

TEGDME	Triethylene glycol dimethyl ether
TEM	Transmission electron microscope
TGA	Thermogravimetric analysis
TM	Transition metal
XPS	X-ray photoelectron spectroscopy
XRD	X-ray diffraction

Chapter 1

1 Li-S Battery: An Overview, Working Principles, and Applications

1.1 Introduction

The battery is one of the most convenient energy-storage devices among the available devices. It is generally classified into two types, (i) primary batteries and (ii) secondary batteries. The primary batteries are non-rechargeable, while the secondary batteries can be rechargeable multiple times. Both kinds of batteries are in use depending on the applications. The Li-ion batteries (LIBs) are impacting the digital revolution of the 21st century, post-discovering LiCoO₂ (LCO) as cathode material in 1980.[1,2] Later, it was replaced by LiNi_xMn_yCo_zO₂ (NMC),[3,4] LiNi_xCo_yAl_zO₂ (NCA),[5] LiMn₂O₄ and LiFePO₄[6,7] in LIBs for the portable applications, such as electric vehicles (EV), even in large scale stationary devices. These cathodes work on the principles of intercalation mechanism during the charging-discharging process, and they deliver a capacity of ~250 mAh/g, and gravimetric energy density ranges between 50 to 260 Wh/kg[8] (Figure 1.1).

The Li-S battery was discovered earlier in the 1960s,[9,10] much more cost-effective than traditional LIBs. But, due to the series of challenges in controlling the lithium sulfides, which form while the lithiation and de-lithiation process, it was not succeeded. Meanwhile, LIBs took the lead in occupying the energy market. But, due to the increase in our demand for energy for the near future, it requires energy storage devices with high energy density, and Li-S battery is one of the promising devices. As increasing the demand for energy in the future, we are urged to find alternative storage devices with high energy density and reduce the cost of the materials. The Lithium-Sulfur (Li-S) batteries are promising due to Sulfur is one of the most abundant materials on earth, its high theoretical capacity (1675 mAh/g), and Li-S batteries have a theoretical energy density (~2600 Wh/kg). Since Li-S batteries offer a five-fold theoretical capacity than conventional Li-ion batteries, it gives faith in replacing the widespread metal-rich cathode of Li-ion batteries with highly cheap and one of the most abundant cathode materials. The higher theoretical capacity also promises to achieve lightweight batteries/batteries with maximum energy.

Sulfur is one of the most abundant elements and is widely available in the earth's crust, and can be used as active material in batteries. However, it is limited due to its insulating nature and requires blending with conductive materials. In addition, the volume changes occurred in Li-S systems. Unlike Li-ion batteries, it undergoes conventional mechanisms, where the various chain lengths of polysulfide form. Further, the forming intermediates of lithium polysulfides are also insulating in nature and soluble in the electrolytes developed as of now, are more challenging to create the system as reversible and more effective. However, considerable

developments have been in progress with Li-S batteries in the past decade by refining the conductive materials, separators, electrolytes, and solvents for commercial applications.

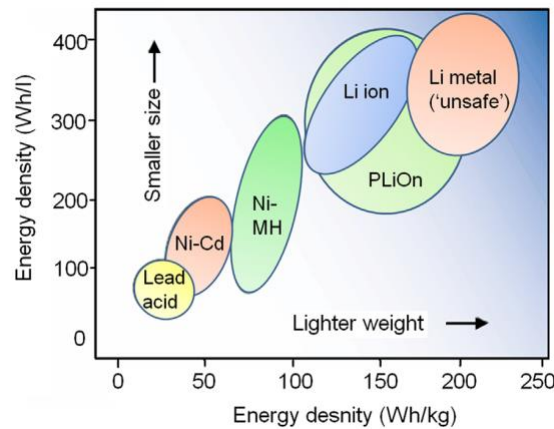


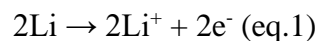
Figure 1.1. Ragone plot with respect to gravimetric and volumetric energy densities.[8]

1.2 Working Principles of Li-S batteries

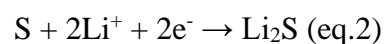
Li-S battery is an electrochemical energy-storage device where the electrical energy is stored in elemental Sulfur as an electrode. A schematic diagram of the Li-S battery, with its charge/discharge process, is shown in Figure 1.2a.

In general, Li-S batteries consist of Sulfur blended with conductive materials and a binder as a cathode, which are coated onto the current collector (Aluminum foil), Lithium metal as an anode, separator, and organic electrolyte in a mixture of organic solvents. Since the Sulfur is in the charged state, the process begins with discharge. When discharged, the lithium metal anode generates Li^+ ions and electrons. These Li^+ ions diffuse through the electrolyte towards the cathode side, and electrons travel to the sulfur cathode by an external circuit, and elemental sulfur will be reduced to Li_2S with potential vs. Li^+/Li , as shown in Figure 1.2b.[11] When charged, Li^+ ions moved towards the anode side and reduced to lithium metal. The reactions are,

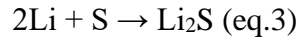
Anodic reaction (-):



Cathodic reaction (-):



The overall discharge reaction is,



The elemental Sulfur undergoes a reversible reaction (eq.3) during the charging process. The theoretical capacity of elemental Sulfur and Lithium metal has been calculated from the below formula:

$$Q \text{ (theoretical capacity)} = \frac{nF}{M}$$

Where Q is the theoretical capacity (mAh/g), n is the number of electron(s) transfer involved in the redox reaction, F stands for Faraday constant (96485 C/mol), and M is molecular weight (g/mol).

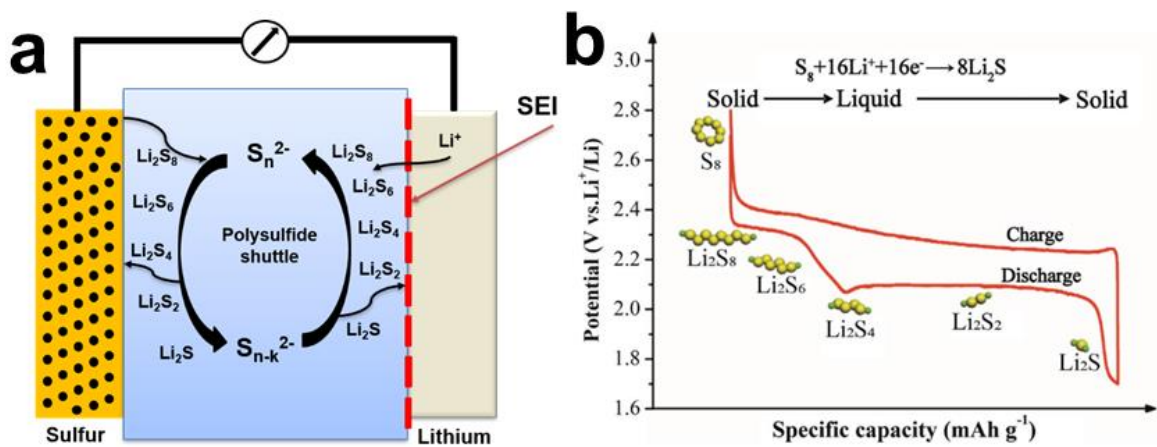


Figure 1.2. Schematic diagram of Li-S cell (a) and typical charge-discharge profile with the state of Sulfur/LiPSs.[11]

So, the theoretical capacity of elemental Sulfur is 1675 mAh/g, and Lithium metal is 3861 mAh/g, which provides the theoretical capacity of 1167 mAh/g for Li-S cells.

1.3 Challenges of Li-S batteries

There are several challenges with Li-S batteries, the materials used as well as the system. The elemental Sulfur, which is active material is highly insulative ($\sim 10^{-30}$ S/cm), and the LiPSs (Li_2S_n , $2 \leq n \leq 8$) form as intermediate are also insulative and structural changes that occur in the system are formidable. The intermediates leach out from the cathode, which is soluble in ether-based electrolytes. Further, it deposits on the anodic part, which leads to the internal resistance of the system. These above issues are the to the low utilization of active material, capacity fading during cycling, and poor efficacy of the system. The Sulfur undergoes the volumetric expansion of $\sim 80\%$, [12] and the Li dendrites form on the surface of the anode (Li metal) [13] during the cycling process, which further leads to loss of capacity.

1.3.1 Shuttle effect

At the earliest, Mikhaylik and Akridge evaluated the polysulfide shuttle behaviors in the Li/S system.[14] The high-order lithium polysulfides (Li_2S_n , $6 < n \leq 8$), which form as an intermediate product, are highly soluble in currently used ether-based solvents such as 1,3-dioxolane (DOL) and 1,2-dimethoxy ethane (DME), which leads to poor efficiency. The major reason is that there is no interaction between the Sulfur host and LiPSs. In general, the polysulfide shuttle mechanism involves five steps[15]. They are,

- (i) Formation of high-order lithium polysulfides (Li_2S_n , $6 < n \leq 8$),
- (ii) Leaching of polysulfides from the host materials,
- (iii) Dissolution of polysulfides into ether-based electrolytes,
- (iv) Passage of polysulfides towards anodic compartment (Lithium) and
- (v) Reaction of polysulfides with Lithium metal.

The polysulfides are negative in charge, migrating between cathode and anode, and deposit on Lithium, leading to capacity loss.

1.3.2 Self-Discharge

Self-discharge is when the battery loses its stored electrical energy without any external circuit. It is a battery characteristic; due to the chemical reactions in most batteries, there is a loss of capacity with time at rest.

Unfortunately, Li-S batteries undergo self-discharge like Nickel-Cadmium Nickel-Metal hydride batteries. As the dissolution of the elemental Sulfur and high-order, polysulfides are inevitable in Li-S batteries, the self-discharge accelerates, resulting in decreases in open circuit voltage and hence fading in capacity.[14,16-18]

1.4 Components of Li-S batteries

Li-S batteries consist of multiple components. They are (i) Cathode, (ii) Anode, (iii) Separator, (iv) Electrolytes, (v) Solvents, and (vi) Additives.

1.4.1 Cathode

In Li-S batteries, the elemental Sulfur functions as active cathode material. Unfortunately, Sulfur is insulative and alone does not hold on current collector due to weak interaction. So, it requires a host material to provide conductivity as well as withhold the active material during fabricating and cycling process. The porous carbon supported Sulfur composite was developed by E. Peled et al.[19] to improve the contact efficiency, as results in increasing the volumetric

energy density. Later Wang et al.[20] developed the porous carbon matrix for Sulfur composite improved the cyclic performance significantly. In 2009, Nazar and co-workers[21] developed highly ordered and nanostructured carbon materials from sucrose, and Sulfur was introduced into it by a melt-diffusion method. This composite material exhibits about 80% of the theoretical capacity (1320 mAh/g) of Sulfur.[21] This work provides the pathway to developing the cathode for Li-S batteries. Later, various types of carbon with functionalization developed with improved performances.[19,22-26]

1.4.1.1 Sulfur-Carbon composite materials

Conducting carbon materials have been used to prepare the composites, which not only act as conductive additives but also support to prevent the shuttling effect and protect the anode. Porous-conducting carbon-based materials are compatible with ether-based electrolytes and exhibit reasonable stability.[22,23]

Porous Carbon: The porous carbon with a high surface area adequately offers physical confinement, and it limits the dissoluble polysulfides and suppresses the shuttling factors. The electrochemical activity of Sulfur-carbon composites is based on the nature of the carbon. The porous carbons are generally classified into three categories according to their pore size (D) and structural morphology.[27] They are (i) Macro porous carbon ($D > 50$ nm) derived from carbon nanotube (CNT), carbon nanofiber (CNF), and spherical macropores are helped to the penetration of the Sulfur and provide sufficient porosity for the electrolytes and ion diffusion process.[28-30] (ii) Microporous carbon ($D < 2$ nm), the Sulfur encapsulates into the narrow micropores and restricts the dissolution of polysulfides into the ether-based organic solvents and dominant factor for the successful electrochemical reversibility.[22-24,31-33] (iii) Mesoporous carbon (2 nm $< D < 50$ nm) tolerates the Sulfur penetration and improves the ion transport, which results in high reversibility with the high Sulfur mass load.[34-42]

Hierarchical porous carbon: It is a multimodal pore size distribution of porous carbon (micro/meso/macro-porous carbon). Hence, the existence of almost all of the porous carbons' properties (physical and chemical) functions as successful electrode materials in energy storage devices.[21,43] It is widely produced from renewable resources or wastes treated under thermal and chemical processes.[44] The micropores provide a way to encapsulate the elemental Sulfur and immobilize the active material. Microporous structure helps electrolyte immersion, while mesopores select the active materials and it attracts the dissolved polysulfides, which suppress the Li-S batteries from capacity fade.[21,25,44-47]

Carbon Nanotubes (CNTs): In general, Multi-walled carbon nanotubes (MWCNTs) offer a high surface area and three-dimensional (3D) conducting network, which helps to adsorb the polysulfides.[48] The Sulfur with MWCNT composites is potentially supported by absorbing the electrolytes, which confine the polysulfides within the cathode compartment; as a result, the Li-S batteries are protected from the capacity fade.[29,48,49] Further, MWCNTs have been modified with heteroatoms or functional groups to achieve better performances for Li-S batteries. The composite using $\text{CoS}_2@\text{NC}/\text{MWCNT}$ and Sulfur has delivered a remarkable discharging capacity of 1133 mAh/g at 0.1C and 607 mAh/g at 2.0C rates.[50]

Hollow carbon spheres: It is also known as carbon capsules, are generally synthesized using hard templates as a result of carbon particles with a size of a millimeter or micron or nanometre. These materials are desirable due to their properties, such as the ability to encapsulate the Sulfur, chemical stabilities, surface functionality, and high surface/volume ratio.[51,52] The hollow carbon spheres are doped with various metals to electrocatalyst the redox system in Li-S batteries.[34,53-56]

Carbon Nanofibers (CNFs): The morphology of CNFs is similar to CNTs in the absence of a hollow cavity with a length of 5-100 microns and a diameter of 5-100 nm. Due to the high electrical conductivity of CNFs, it has been widely used in Li-ion batteries and Supercapacitors.[57-61] In the case of Li-S batteries, these CNFs are further modified with metal/metal oxides and serve as Sulfur hosts as well as conductive additives while the metals control the polysulfide shuttle.[53,62] It is generally synthesized through two methodologies, (i) the precipitation of carbon by an annealing process in a controlled atmosphere and (ii) electrospinning using carbon-containing liquids as a precursor.[63,64]

Graphene: Graphene is a well-known 2D (two-dimensional) carbon monolayer consisting of sp^2 hybridized carbon with several fascinating properties such as light-weight, excellent electrical and thermal conductivities, high mechanical strength (~ 1 TPa), tuneable surface area and chemical stability.[65-67] It can be prepared through various techniques. In 2004, Geim et al. demonstrated the preparation of monolayer graphene from raw graphite on an atomic scale.[68,69] Later, graphene becomes one of the promising candidates for many applications, especially in energy storage devices, due to the availability of raw components and its excellent properties.[70-72] Since graphite and graphene are highly stable in a wide range of chemicals and mechanical strength, they can be easily tuneable and introduce functionality through mechanical[73-76] as well as a wet chemical process.[77,78] The traditional wet chemical

process involves the chemical oxidation and functionalization process, which requires strong acids and hazardous oxidizing agents. Though these are energy-saving processes with high yields, but not eco-friendly due to the hazardous chemicals involved in the reactions.[79] Later, the intercalation and oxidation of graphite/graphene were carried out through electrochemical techniques, which are easily controllable methods.[80,81] Ester Vázquez et al. reported the preparation of a few layered graphene layers from pristine graphite materials by mechanical method (Ball-milled process) using melamine as an intercalator.[73] Since the less quantity of chemicals/solvents used in this method is green and highly scalable, also the intercalator can be tuned as required.

Graphene is a compatible candidate for the Sulfur host, and the functionalization/modification of graphene protects the Li-S batteries from the shuttle effect, as results prevent the capacity fading. The elemental Sulfur has been deposited/wrapped with Graphene/functionalized Graphene (FG) by melt-diffusion or wet chemical process, which is demonstrated for Li-S batteries with a high rate of charge/discharge.[82-87] The modified graphenes' in the form of Graphene oxides,[82,88-95] Graphene sponge,[96-98] Graphene aerogel,[99] exfoliated graphene layers,[100] Graphene nanosheets,[101] mixture of Graphene/CNT,[102,103] Graphene/Porous carbon,[104] N-doped,[105,106] N,S-doped,[98] Graphene/Metal or Metal oxides,[107-109] Graphene/MOF[50].

1.4.1.2 Sulfur-Inorganic composite materials

The Metal-based materials could serve as electrocatalysts in a wide range of applications in energy conversion and storage devices.[110-114] Even the Metals could act as an absorbing agent, providing the pathway to use it as a supporting additive in Li-S batteries. Unlike porous carbon, most metal-based materials could not serve as the Sulfur hosting materials unless the presence of voids due to their low surface area. We must note that the redox potential should not overlap between the 1.5 V – 3.0 V vs. Li^+/Li^0 . In contrast, the redox potential of Sulfur appears, which would lead to structural changes in the catalysts and unwanted electrochemical reactions in the systems. Also, density is an essential factor in case of metal-based materials; the higher density of materials or more quantity affects the energy density of batteries, where the energy density is indirectly proportional to the mass of loaded materials.[115,116]

Metal oxides: The Metal oxides could bind with the Lithium polysulfides, which form during the cycling, trap at the cathode, and potentially prevent the Li-S systems from capacity decay. A wide range of metal oxides is investigated for the Li-S batteries, such as TiO_2 , MnO_2 , SiO_2 ,

SnO₂, SiO₂, Al₂O₃, etc.[117,118] are, exhibited improved cycle life. The TiO₂ yolk-shell nano-architecture combined with internal void spaces demonstrated to Li-S batteries, where the void spaces allow to penetrate the Sulfur while the metal oxide traps the polysulfides.[119] The initial gravimetric capacity of 1030 mAh/g at 0.5 C rate with coulombic efficiency of 98.4% for thousand cycles and less capacity decay of 0.033% per cycle has been observed. The δ-MnO₂ has been synthesized by the green method, and Sulfur encapsulation was carried out using poly-dopamine, inhibiting the soluble Lithium polysulfide shuttle.[120] Wang et al. examined the interaction between Lithium polysulfides and Transition metal oxides through X-ray photoelectron spectroscopic (XPS) techniques and theoretical studies.[121] It has been concluded that the Metal oxides are reduced and change in the oxidation state of the metals, which is proved by the shift in binding energy in XPS studies. Significant metal-sulfur interactions were reported for the Co₃O₄, while observed negligible for Fe₂O₃ and Mn₃O₄.

Metal sulfides: In order to understand the crucial factors affecting the energy barrier for Li₂S oxidation and polysulfide adsorption, a variety of metal sulfides have been studied. Metal-Sulfides can produce lower overpotential compared to utilized carbon-based materials due to evidence that the Lithium sulfides breakdown energy barrier is linked to the interaction between isolated Li⁺ ions and the Sulfur in sulfides. The interaction between Li₂S₆ and Ni₃S₂, SnS₂, FeS, CoS₂, VS₂, and TiS₂ were demonstrated, and VS₂, TiS₂, and CoS₂ comprised electrodes exhibited the higher capacity, less overpotential, also less capacity decay as compared to other metal sulfides based electrodes.[122]

Single-atom catalysts: Recently, single-atom catalysts (SACs) have experienced rapid growth as a unique catalytic approach that has been used in numerous significant catalytic processes with great success. The low precious metal content, good selectivity, and easily tuneable features of SAC are advantages. SACs have been employed as electrocatalysts in several applications.[123-127] SACs with separate metal centers and atomic size levels often have the highest atom usage, unsaturated metal species, and distinctive electrical structures. As a result, they were frequently employed as catalysts in the conversion and storage of energy. The SACs are efficiently reduce the shuttle factors and accelerate the kinetics of the conversion in Li-S batteries. Manthiram et al. reported that the Fe-Ni catalyst promotes the Lithium polysulfide conversion with a low Electrolyte/Solvent (E/S) ratio of 4.5 μl/mgs.[128]

1.4.1.3 Organic Framework/Sulfur composite

The Covalent-organic frameworks (COFs) and Metal-organic frameworks (MOFs) have excellent attention to utilize in Evolution/Reduction reactions, energy conversion, and storage applications due to their abundant porosity with pores and remarkable surface area. The functional groups in the organic framework can be tuned as demand in certain applications.[129-132] The COFs/MOFs substantially bonding with Sulfur species and are involved in the potential electrochemical conversion reactions, also attract the polysulfides.[133] The hybridized MOFs with a heteroatom(s) doped materials or other chemicals which provide additional support to electrochemical reactions and polysulfide adsorption.[33,134] For example, MOF derived Cobalt disulfide along with N-rich MWCNTs were reported with a high specific capacity of 1133 mAh/g at 0.1 C rate and a remarkable capacity of 607 mAh/g at 2.0 C rate and cyclability with a decay rate of 0.078% per cycle.[50]

1.4.1.4 MXene/Sulfur composites

The MXenes have been discovered in the last decade and are widely researched work carried out for energy-based applications.[135] The Mxenes are defined in a general formula, $M_{n+1}X_nT_z$ (M = early transition metals, group 3 to 7, X = Carbon/Nitrogen, T = terminate surface groups -O, -OH, and -F, which replace the Al while etching). The surface chemistry of MXenes is an advantage to building Mxene-based materials. These Mxene family materials get great attention because of their structural variety, metallic conductivity, catalytic activity, and ability to adsorb the polysulfides. About 30 MXenes have been discovered to date, and limited methods are only available to exfoliate them. Further, very few Mxene-based materials (Ti_2C and Ti_3C_2) function in Li-S batteries as of now. These materials not only solve the fundamental issue but also help achieve increased energy density, mass loading, long life span, and areal capacity and reduce the E/S ratio.[136-138]

1.4.1.5 Polymer/Sulfur composites

The Sulfur species could be physically encapsulated with the conducting polymers and used along with mesoporous carbon as a promising cathode, while the carbon weakly interacts with polysulfides. The polyaniline with yolk-shell[139] and nanotube[140] structures have been reported with improved performances; it helps to confine the elemental Sulfur as well as lithium polysulfides and, as a result, reduces the volume expansion. The polymer-derived porous carbons are used as Sulfur hosts, the pores and porosity act as “lithophilic” sites, and the heteroatom present in these porous carbon act as “sulfiphilic” sites. Due to the presence of dual active sites, unprecedented control over the polysulfide shuttles was observed.[141,142]

1.4.1.6 Sulfur

The cathode part of Li-S batteries consists of elemental Sulfur confined with a conductive additive due to its highly insulative nature of Sulfur. Sulfur appears pale yellow in color, odorless, and brittle in nature. The majority of Sulfur is occurred from the earth as salts and is extracted by the Frasch process, and about 25% of Sulfur is obtained as a by-product in petroleum industries during the refining process. The Sulfur exists in the most significant number of solid allotropes, with over 30 forms[143]. The well-known form of Sulfur is S_8 in a ring structure; besides this form, S_n ($n = 6-26$) are also available.[144] In general, three broad forms of Sulfur exist (i) orthorhombic, (ii) monoclinic, and (iii) amorphous. The orthorhombic form is the most stable and naturally available among others; the monoclinic forms are obtained at 96 °C to 119 °C and revert to orthorhombic with time when it cooled down to room temperature. Amorphous forms exist while immediately cooled down to room temperature, which is soft and elastic in nature.

The Sulfur composites are generally synthesized through two methods. (i) In-filtration method, and (ii) Wet chemical method. The In-filtration process has been demonstrated by mixing the conductive additives such as porous carbon/Graphene-based materials and elemental Sulfur with a defined ratio and thermally treating them under an inert atmosphere (Argon), which allows encapsulation of the Sulfur in the molten state to the materials.[40] Also, it requires the solvent (Carbon disulfide or Toluene) to encapsulate the Sulfur in this process. While the wet chemical process, the Sulfur precursor solution was mixed with the dispersed conductive additives in an aqueous medium in the presence of surfactants such as Triton X-100[33], PVP[89], etc. Further, by adding the acid (HCl), the Sulfur was precipitated and wrapped with the materials.

The ultrafine nano-sulfur particles were synthesized by the ball-mill method and decorated on in-situ exfoliated graphene, which resulted in an increase in the electrical and ionic conductivity as well as alleviated the volume expansion.[100] The orthorhombic form of Sulfur has been widely used in Li-S batteries. Also, the novel phase of Sulfur (γ -monoclinic phase) has been synthesized and demonstrated in the Li-S batteries with carbonate-based electrolytes, a better specific capacity of 800 mAh/g, and a decay rate of 0.0375% for over 4000 cycles was achieved.[145]

1.4.1.7 Binder

The binder plays a vital role in the battery electrodes. The conventional binders PVDF and PTFE are widely used in Li-ion batteries and also function in Li-S batteries. Since the reaction varies in both types of batteries, Li-S batteries could perform with better efficacy while using the different binders or modifications in the conventional binders. Poly(ethylene oxide) (PEO) and poly(ethylene glycol) (PEG) were used as binder or polymer coating to uplift the sulfur utilization, electrochemical reversibility of Sulfur species, suppress the passivation of cathode materials at the end of discharge, as a result in increased reversible capacity.[146] The bifunctional PVP binders substantially provide strong Li-O interaction with Li_2S and Lithium polysulfides.[147] E. Peled et al. investigated the various binders in the cathode for Li-S cells and achieved a capacity of 500 to 1400 mAh/g, depending on the binders used. The order of functional group in the binder interacts with Lithium polysulfides, $\text{LiPAA} > \text{PVP:PEI} > \text{PVP} > \text{PVDF-HFP} > \text{PANI}$, which were confirmed from the reversible capacity.[148] The polar binder with the amino functional group and the 3D network has been reported for high-energy-density Li-S batteries. It shows a significant improvement in capacity retention (91.3%) over 600 cycles due to this binder exhibiting high binding strength with polysulfide intermediates, which effectively reduces polysulfide dissolution. Also, the enormous mechanical properties of amino functional group (AFG) binder offer the buffer in a volume change of the cathode materials.[149] The positively charged, PVP-based polycation binders are synthesized to effectively adsorb the negatively charged polysulfide species.[150] Mainak Majumder et al. reported the saccharide-based binder to regulate the consumption of electrolyte and polysulfide dissolution.[151] The water-soluble multi-functionalized binders were remarkably helpful to the Li^+ ion transfer.[152,153]

1.4.2 Anode

The anode plays a vital role in Li-S batteries because the cyclic stability of the system depends on it. Due to the low potential, high capacity, and high energy density of Li metal, is an excellent anode material for Li-ion and Li-S batteries. However, the Li metal reacts with the organic electrolytes, which is unsafe for the rechargeable batteries. A limited numbers of alternate anode materials are available and investigated for Li-S batteries.[13,154]

Lithium metal: The Li metal has a theoretical capacity of ~ 3860 mAh/g, extremely low electrode potential (-3.04 V vs. standard hydrogen electrode (SHE)), and high volumetric energy density (> 900 Wh/L).[155-157] Although it has excellent features, it still suffers with dendrite formation and poor cycling efficiency, which directly results in the low cyclic stability

and unsafety of Li batteries. The as-formed dendrites affect the passivation or solid electrolyte interface (SEI) layer on the Li metal anode. Further, the affected SEI layers lead to creating contact between fresh Li metal and organic electrolytes, which involves parasitic reactions, and results in poor cyclic efficiency.[158-161]

In Li-S batteries, the collective intermediate products involve and are soluble in organic-based electrolytes, leading to intense parasitic reactions on the anode and causing the degradation of Li metal.[162] Therefore, Silica and Silicon carbides decorated 3D carbon fiber current collectors were investigated for high-energy electrodes.[159] Also, to control the Lithium dendrite formation, graphene sheets could serve as a current collector.[160] Still, the Li metal could not function as an effective anode-type material, and it hindered the Li-S battery from commercialization.

Carbon: The graphite facilitates the Li^+ ion intercalation/deintercalation, due to its layered structure, so it successfully functions as an anode candidate for Li-ion batteries.[163] In Li-S battery systems, the graphite is failed to be an anode candidate because of the incompatibility of electrolyte systems. It undergoes for weak interaction between graphene planes in graphite, while ether-based solvents are used to cause the surface stability of graphite particles.[164] In 2013, Brückner et al. reported the hard carbon as a stable anode for 1300 cycles in Li-S full cell.[165] Also, high Sulfur utilization has been observed with the low volume of electrolytes in the ether solvent system, which promises carbon-based materials as an anode for Li-S batteries.

Silicon: Silicon (Si) has been examined as one of the most desirable anode candidates for LiBs due to enormous gravimetric (3600 mAh/g) and volumetric capacity values, abundance, low cost, and environmental friendliness.[166,167] But, the Si materials get the volumetric expansion of upto 300% due to mechanical failures during cycling, which cause the capacity fading.[168] The Lithiated Si-based materials were developed to boost the electronic conductivity and reduce the volumetric expansion. These Li metal-free, Silicon-Sulfur batteries exhibited a reversible capacity of about 300 mAh/g for 100 cycles with safety.[169,170]

1.4.3 Electrolytes

The electrolytes play a crucial role in Li-S batteries because the Li^+ ion transport occurs between the cathode and anode through it. The liquid phase electrolytes are commonly used in rechargeable batteries due to ionic conductivity as compared to solids. But, the as-formed lithium polysulfide intermediates are highly soluble in liquid electrolytes, causing the shuttle

phenomena. Hence, solid electrolytes could solve this issue. Unfortunately, solid electrolytes carry lack ionic conductivity.

Liquid electrolyte: Since the 1,3-Dioxolane (DOL) solvent was evaluated with high conductivity, the liquid electrolyte was developed in various stages to utilize the maximum amount of Sulfur.[171] Further, the ether-based solvent, Dimethoxy ethane (DME), was developed along with the lithium salts such as Lithium trifluoromethanesulfonate (LiTFS), Bis(trifluoromethane)sulfonimide lithium salt (LiTFSI), which are widely used. The mixture of Triethylene glycol dimethyl ether (TEGDME) and DOL (TEGDME: DOL) were found to be a better solvent system [172]; while TEGDME increases the solubility of Li salts, DOL helps to decrease the viscosity of the system, result in an increase in the transportation of Li^+ ions. Also, found negligible self-discharge behavior while using TEGDME as solvent.[173] A highly concentrated electrolyte (7 M of LiTFSI) was found to be Li^+ ion transference number of 0.73, which is even more than the lower concentration served in the Li batteries.[174] The highly fluorinated electrolytes suppress the formation of Li dendrite growth and enormously reduce the dissolution of high-ordered lithium polysulfides in the battery electrolyte system. Additionally, it also provides the pathway to lean electrolytes.[175,176]

Carbonate-based electrolyte: Towards the commercialization of Li-S batteries, carbonate-based electrolytes must be investigated because the ether solvents have significantly less boiling point, which affects the safety. In case of carbonate-based electrolytes, lithium metal as an anode can be replaced with graphite and etc. The difficulty in using these electrolytes is that the intermediate polysulfides react with carbonate, which results in the loss of reversibility of Sulfur.[177,178] Although a failure mechanism was found while using carbonate electrolytes, the research works have been parallelly carried out related to tuning the Sulfur host[31,179], developing the gel electrolyte membrane[20], and creating a new class of additives[180].

Solid-state electrolyte: The solid-state electrolytes are the predominant solution to control the solubility of polysulfides and shuttle factors. Further, it could potentially suppress the Li dendrite formation and metallic Li anode. But it is limited to the Li^+ ion transport (ionic conductivity) in the systems.[181,182] The polymers like triethylene glycol dimethylether (TEGDME) and polyethylene glycol dimethylether (PEGDME) were widely investigated for solid-state Li-S battery systems because of their ionic conductivities and other physical properties.[183] The conducting electrolyte ($\text{LiCF}_3\text{SO}_3\text{-TEGDME}$) has exhibited excellent electrochemical performances, the delivering capacity of 500 mAh/g at an even higher rate,

with an average potential of 2 V and gravimetric energy density of 1500 kWh/g.[184] Li_2S - P_2S_5 glass-ceramic electrolytes were evaluated with elemental Sulfur and Copper(II) sulfide (CuS) as cathode material, obtained 650 mAh/g for 20 cycles.[185] Later, MoS_2 decorated Li_2S - P_2S_5 glass-ceramic electrolyte was developed with a high reversible capacity of 1020 mAh/g.[186] The solid electrolyte of Ta-doped garnet ($\text{Li}_{6.4}\text{La}_3\text{Zr}_{1.4}\text{Ta}_{0.6}\text{O}_{12}$, LLZTO) developed along with Gold (Au) coating on the anode side to suppress the interfacial resistance, and P_2S_5 - Li_2S as an additive in liquid catholyte to boost the solubility of short-chain polysulfides and utilize the maximum amount of Sulfur. 3.2 and 5.3 mg_s/cm^2 of materials were loaded for coin and pouch cells, respectively, achieved the gravimetric reversible capacity of 1088 mAh/g and 799 mAh/g, and the areal capacity of 3.5 $\text{mAh}/\text{cm}^{-2}$, 4.23 $\text{mAh}/\text{cm}^{-2}$, respectively.[187] The bilayer (Polymer electrolyte, PEO+LiTFSI, and LCO) were developed to eliminate the flammable organic electrolytes, also resulting in less capacity loss.[188]

1.4.4 Additives

Although Li-S batteries were started in late 1960[189], it was suffered with huge capacity loss, till discover the additive in the liquid electrolyte to protect the Li anode.[190] It has been proved that N-O bond from Lithium nitrate (LiNO_3) leads to form the in-situ stable SEI layers on the surface of Li metal.[162,191] Further, it confirmed that a moderate concentration (0.4 M) of LiNO_3 is required to achieve better cyclic stability, without imparting any impact on suppressing the polysulfide dissolution process. Sheng S. Zhang proposed that although LiNO_3 protects the surface of the metallic Lithium, it plays a negative role at the cathode by affecting the carbon as a Sulfur host at a potential lower than 1.6 V, which cause the irreversibility of polysulfide formations.[192] Further, the LiNO_3 catholyte for Li-S system was evaluated and highly reversible capacity was achieved upto cut off at 1.8 V, which corresponds to the formation of insoluble Li_2S_2 . While discharging to lower than 1.8 V, Li_2S_2 reduces to Li_2S , and parallelly LiNO_3 reduces to irreversible species, which further stagnant the kinetics of reversible electrode reactions.[193] This work proposes that deep discharge of Li-S batteries must be avoided to achieve the improved cycle life, while using LiNO_3 as an additive or co-salts.

1.4.5 Separator

The polyolefin separators, polyethylene (PE), polypropylene (PP), and a combination of PE/PP with a range of micrometer pore sizes have been commercialized for Li-ion battery technology.[194] These are porous in nature, chemically stable, and economically low-cost. However, only these properties are insufficient to reduce the polysulfide dissolution and shuttle

effect. So, either functionalization of the polyolefin separator or the different separator with barrier property against the polysulfides could protect from shuttle factors.

The above-mentioned Sulfur host materials in section 1.4.1 can be used to modify the polypropylene separator, according to compatibility. In general, the slurry prepares with the as selected materials, with or without carbon black and binder, and coats onto one-side of Celgard separators. Further, it could be used with the coating towards the cathode part to reduce the shuttle phenomena. Various types of material have been investigated for Li-S system.

The bifunctional separator (Super P carbon on PP separator) has been demonstrated with elemental Sulfur cathode for Li-S batteries, and provides a discharge capacity of 1389 mAh/g for initial cycles with dynamic stability, and 828 mAh/g for 200 cycles.[195] Further, the heteroatom(s) doped carbon[54,196,197] or Graphene[198,199], inorganic components[107,200-207], Organic frameworks[208-211], and polymers[212] were developed for effective suppression of shuttle mechanism.

1.5 References

- [1] Mizushima, K.; Jones, P. C.; Wiseman, P. J.; Goodenough, J. B. Li_xCoO_2 ($0 < x < 1$): A new cathode material for batteries of high energy density. *Mater. Res. Bull.* **1980**, *15*, 783-789.
- [2] Mizushima, K.; Jones, P. C.; Wiseman, P. J.; Goodenough, J. B. Li_xCoO_2 ($0 < x \leq 1$): A new cathode material for batteries of high energy density. *Solid State Ionics* **1981**, *3-4*, 171-174.
- [3] Ohzuku, T.; Makimura, Y. Layered Lithium Insertion Material of $\text{LiCo}_{1/3}\text{Ni}_{1/3}\text{Mn}_{1/3}\text{O}_2$ for Lithium-Ion Batteries. *Chem. Lett.* **2001**, *30*, 642-643.
- [4] Lu, Z.; MacNeil, D. D.; Dahn, J. R. Layered $\text{Li}[\text{Ni}_x\text{Co}_{1-2x}\text{Mn}_x]\text{O}_2$ Cathode Materials for Lithium-Ion Batteries. *Electrochem. Solid-State Lett.* **2001**, *4*, A200.
- [5] Chen, C. H.; Liu, J.; Stoll, M. E.; Henriksen, G.; Vissers, D. R.; Amine, K. Aluminum-doped lithium nickel cobalt oxide electrodes for high-power lithium-ion batteries. *J. Power Sources* **2004**, *128*, 278-285.
- [6] Goodenough, J. B.; Kim, Y. Challenges for Rechargeable Li Batteries. *Chem. Mater.* **2010**, *22*, 587-603.
- [7] Manthiram, A. Materials Challenges and Opportunities of Lithium Ion Batteries. *J. Phys. Chem. Lett.* **2011**, *2*, 176-184.
- [8] Diouf, B.; Pode, R. Potential of lithium-ion batteries in renewable energy. *Renewable Energy* **2015**, *76*, 375-380.
- [9] Herbert, D.; Ulam, J. Electric dry cells and storage batteries. *U.S. Patent* **1962**, 3043896.
- [10] Nole, D. A.; Moss, V., Battery employing lithium-sulphur electrodes with non-aqueous electrolyte. *U.S. Patent*: **1970**.
- [11] Fang, R.; Zhao, S.; Sun, Z.; Wang, D.-W.; Cheng, H.-M.; Li, F. More Reliable Lithium-Sulfur Batteries: Status, Solutions and Prospects. *Adv. Mater.* **2017**, *29*, 1606823.
- [12] Wang, L.; Wang, D.; Zhang, F.; Jin, J. Interface Chemistry Guided Long-Cycle-Life Li-S Battery. *Nano Lett.* **2013**, *13*, 4206-4211.
- [13] Tao, T.; Lu, S.; Fan, Y.; Lei, W.; Huang, S.; Chen, Y. Anode Improvement in Rechargeable Lithium-Sulfur Batteries. *Adv. Mater.* **2017**, *29*, 1700542.

- [14] Mikhaylik, Y. V.; Akridge, J. R. Polysulfide Shuttle Study in the Li/S Battery System. *J. Electrochem. Soc.* **2004**, *151*, A1969.
- [15] Ren, W.; Ma, W.; Zhang, S.; Tang, B. Recent advances in shuttle effect inhibition for lithium sulfur batteries. *Energy Storage Mater.* **2019**, *23*, 707-732.
- [16] Ryu, H. S.; Ahn, H. J.; Kim, K. W.; Ahn, J. H.; Lee, J. Y.; Cairns, E. J. Self-discharge of lithium–sulfur cells using stainless-steel current-collectors. *J. Power Sources* **2005**, *140*, 365-369.
- [17] Lacey, M. J.; Yalamanchili, A.; Maibach, J.; Tengstedt, C.; Edström, K.; Brandell, D. The Li–S battery: an investigation of redox shuttle and self-discharge behaviour with LiNO₃⁻ containing electrolytes. *RSC Adv.* **2016**, *6*, 3632-3641.
- [18] Drvarič Talian, S.; Kapun, G.; Moškon, J.; Dominko, R.; Gaberšček, M. Transmission Line Model Impedance Analysis of Lithium Sulfur Batteries: Influence of Lithium Sulfide Deposit Formed During Discharge and Self-Discharge. *J. Electrochem. Soc.* **2022**, *169*, 010529.
- [19] Peled, E.; Gorenshtein, A.; Segal, M.; Sternberg, Y. Rechargeable lithium-sulfur battery (extended abstract). *J. Power Sources* **1989**, *26*, 269-271.
- [20] Wang, J. L.; Yang, J.; Xie, J. Y.; Xu, N. X.; Li, Y. Sulfur–carbon nano-composite as cathode for rechargeable lithium battery based on gel electrolyte. *Electrochem. Commun.* **2002**, *4*, 499-502.
- [21] Ji, X.; Lee, K. T.; Nazar, L. F. A highly ordered nanostructured carbon–sulphur cathode for lithium–sulphur batteries. *Nat. Mater.* **2009**, *8*, 500-506.
- [22] Rehman, S.; Gu, X.; Khan, K.; Mahmood, N.; Yang, W.; Huang, X.; Guo, S.; Hou, Y. 3D Vertically Aligned and Interconnected Porous Carbon Nanosheets as Sulfur Immobilizers for High Performance Lithium-Sulfur Batteries. *Adv. Energy Mater.* **2016**, *6*, 1502518.
- [23] Wu, H. B.; Wei, S.; Zhang, L.; Xu, R.; Hng, H. H.; Lou, X. W. Embedding Sulfur in MOF-Derived Microporous Carbon Polyhedrons for Lithium–Sulfur Batteries. *Chem. Eur. J.* **2013**, *19*, 10804-10808.
- [24] Zhang, W.; Qiao, D.; Pan, J.; Cao, Y.; Yang, H.; Ai, X. A Li⁺-conductive microporous carbon–sulfur composite for Li-S batteries. *Electrochim. Acta* **2013**, *87*, 497-502.
- [25] Liang, C.; Dudney, N. J.; Howe, J. Y. Hierarchically Structured Sulfur/Carbon Nanocomposite Material for High-Energy Lithium Battery. *Chem. Mater.* **2009**, *21*, 4724-4730.
- [26] Liang, J.; Sun, Z.-H.; Li, F.; Cheng, H.-M. Carbon materials for Li–S batteries: Functional evolution and performance improvement. *Energy Storage Mater.* **2016**, *2*, 76-106.
- [27] Dujearic-Stephane, K.; Gupta, M.; Kumar, A.; Sharma, V.; Pandit, S.; Bocchetta, P.; Kumar, Y., The Effect of Modifications of Activated Carbon Materials on the Capacitive Performance: Surface, Microstructure, and Wettability. *J. Compos. Sci.* **2021**; Vol. 5.
- [28] Zheng, W.; Liu, Y. W.; Hu, X. G.; Zhang, C. F. Novel nanosized adsorbing sulfur composite cathode materials for the advanced secondary lithium batteries. *Electrochim. Acta* **2006**, *51*, 1330-1335.
- [29] Su, Y.-S.; Fu, Y.; Manthiram, A. Self-weaving sulfur–carbon composite cathodes for high rate lithium–sulfur batteries. *Phys. Chem. Chem. Phys.* **2012**, *14*, 14495-14499.
- [30] Gueon, D.; Hwang, J. T.; Yang, S. B.; Cho, E.; Sohn, K.; Yang, D.-K.; Moon, J. H. Spherical Macroporous Carbon Nanotube Particles with Ultrahigh Sulfur Loading for Lithium–Sulfur Battery Cathodes. *ACS Nano* **2018**, *12*, 226-233.
- [31] Zhang, B.; Qin, X.; Li, G. R.; Gao, X. P. Enhancement of long stability of sulfur cathode by encapsulating sulfur into micropores of carbon spheres. *Energy Environ. Sci.* **2010**, *3*, 1531-1537.
- [32] Helen, M.; Diemant, T.; Schindler, S.; Behm, R. J.; Danzer, M.; Kaiser, U.; Fichtner, M.; Anji Reddy, M. Insight into Sulfur Confined in Ultramicroporous Carbon. *ACS Omega* **2018**, *3*, 11290-11299.

- [33] Chen, R.; Zhao, T.; Tian, T.; Cao, S.; Coxon, P. R.; Xi, K.; Fairen-Jimenez, D.; Vasant Kumar, R.; Cheetham, A. K. Graphene-wrapped sulfur/metal organic framework-derived microporous carbon composite for lithium sulfur batteries. *APL Mater.* **2014**, *2*, 124109.
- [34] Ma, S.; Wang, L.; Wang, Y.; Zuo, P.; He, M.; Zhang, H.; Ma, L.; Wu, T.; Yin, G. Palladium nanocrystals-embedded mesoporous hollow carbon spheres with enhanced electrochemical kinetics for high performance lithium sulfur batteries. *Carbon* **2019**, *143*, 878-889.
- [35] Sun, F.; Wang, J.; Long, D.; Qiao, W.; Ling, L.; Lv, C.; Cai, R. A high-rate lithium–sulfur battery assisted by nitrogen-enriched mesoporous carbons decorated with ultrafine La₂O₃ nanoparticles. *J. Mater. Chem. A* **2013**, *1*, 13283-13289.
- [36] Zhang, J.; Cai, Y.; Zhong, Q.; Lai, D.; Yao, J. Porous nitrogen-doped carbon derived from silk fibroin protein encapsulating sulfur as a superior cathode material for high-performance lithium–sulfur batteries. *Nanoscale* **2015**, *7*, 17791-17797.
- [37] Chung, S.-H.; Manthiram, A. Nano-cellular carbon current collectors with stable cyclability for Li–S batteries. *J. Mater. Chem. A* **2013**, *1*, 9590-9596.
- [38] Qu, Y.; Zhang, Z.; Zhang, X.; Ren, G.; Lai, Y.; Liu, Y.; Li, J. Highly ordered nitrogen-rich mesoporous carbon derived from biomass waste for high-performance lithium–sulfur batteries. *Carbon* **2015**, *84*, 399-408.
- [39] Zhao, T.; Ye, Y.; Peng, X.; Divitini, G.; Kim, H.-K.; Lao, C.-Y.; Coxon, P. R.; Xi, K.; Liu, Y.; Ducati, C.; Chen, R.; Kumar, R. V. Advanced Lithium–Sulfur Batteries Enabled by a Bio-Inspired Polysulfide Adsorptive Brush. *Adv. Funct. Mater.* **2016**, *26*, 8418-8426.
- [40] Kensy, C.; Leistenschneider, D.; Wang, S.; Tanaka, H.; Dörfler, S.; Kaneko, K.; Kaskel, S. The Role of Carbon Electrodes Pore Size Distribution on the Formation of the Cathode–Electrolyte Interphase in Lithium–Sulfur Batteries. *Batteries & Supercaps* **2021**, *4*, 612-622.
- [41] Li, X.; Cao, Y.; Qi, W.; Saraf, L. V.; Xiao, J.; Nie, Z.; Mietek, J.; Zhang, J.-G.; Schwenzler, B.; Liu, J. Optimization of mesoporous carbon structures for lithium–sulfur battery applications. *J. Mater. Chem.* **2011**, *21*, 16603-16610.
- [42] Borchardt, L.; Oschatz, M.; Kaskel, S. Carbon Materials for Lithium Sulfur Batteries—Ten Critical Questions. *Chem. Eur. J.* **2016**, *22*, 7324-7351.
- [43] Fu, R.-w.; Li, Z.-h.; Liang, Y.-r.; Li, F.; Xu, F.; Wu, D.-c. Hierarchical porous carbons: design, preparation, and performance in energy storage. *New Carbon Mater.* **2011**, *26*, 171-179.
- [44] Wei, S.; Zhang, H.; Huang, Y.; Wang, W.; Xia, Y.; Yu, Z. Pig bone derived hierarchical porous carbon and its enhanced cycling performance of lithium–sulfur batteries. *Energy Environ. Sci.* **2011**, *4*, 736-740.
- [45] He, G.; Ji, X.; Nazar, L. High “C” rate Li-S cathodes: sulfur imbibed bimodal porous carbons. *Energy Environ. Sci.* **2011**, *4*, 2878-2883.
- [46] Ding, B.; Yuan, C.; Shen, L.; Xu, G.; Nie, P.; Zhang, X. Encapsulating Sulfur into Hierarchically Ordered Porous Carbon as a High-Performance Cathode for Lithium–Sulfur Batteries. *Chem. Eur. J.* **2013**, *19*, 1013-1019.
- [47] Schuster, J.; He, G.; Mandlmeier, B.; Yim, T.; Lee, K. T.; Bein, T.; Nazar, L. F. Spherical Ordered Mesoporous Carbon Nanoparticles with High Porosity for Lithium–Sulfur Batteries. *Angew. Chem. Int. Ed.* **2012**, *51*, 3591-3595.
- [48] Han, S.-C.; Song, M.-S.; Lee, H.; Kim, H.-S.; Ahn, H.-J.; Lee, J.-Y. Effect of Multiwalled Carbon Nanotubes on Electrochemical Properties of Lithium/Sulfur Rechargeable Batteries. *J. Electrochem. Soc.* **2003**, *150*, A889.
- [49] Yuan, L.; Yuan, H.; Qiu, X.; Chen, L.; Zhu, W. Improvement of cycle property of sulfur-coated multi-walled carbon nanotubes composite cathode for lithium/sulfur batteries. *J. Power Sources* **2009**, *189*, 1141-1146.
- [50] Chen, C.-H.; Lin, S.-H.; Wu, Y.-J.; Su, J.-T.; Cheng, C.-C.; Cheng, P.-Y.; Ting, Y.-C.; Lu, S.-Y. MOF-derived cobalt Disulfide/Nitrogen-doped carbon composite polyhedrons linked

with Multi-walled carbon nanotubes as sulfur hosts for Lithium-Sulfur batteries. *Chem. Eng. J.* **2022**, *431*, 133924.

[51] Li, S.; Pasc, A.; Fierro, V.; Celzard, A. Hollow carbon spheres, synthesis and applications – a review. *J. Mater. Chem. A* **2016**, *4*, 12686-12713.

[52] Zhang, C.; Wu, H. B.; Yuan, C.; Guo, Z.; Lou, X. W. Confining Sulfur in Double-Shelled Hollow Carbon Spheres for Lithium–Sulfur Batteries. *Angew. Chem. Int. Ed.* **2012**, *51*, 9592-9595.

[53] Li, Q.; Zhang, Z.; Guo, Z.; Zhang, K.; Lai, Y.; Li, J. Coaxial-cable structure composite cathode material with high sulfur loading for high performance lithium–sulfur batteries. *J. Power Sources* **2015**, *274*, 338-344.

[54] Zhang, Z.; Wang, G.; Lai, Y.; Li, J.; Zhang, Z.; Chen, W. Nitrogen-doped porous hollow carbon sphere-decorated separators for advanced lithium–sulfur batteries. *J. Power Sources* **2015**, *300*, 157-163.

[55] Ye, H.; Yin, Y.-X.; Xin, S.; Guo, Y.-G. Tuning the porous structure of carbon hosts for loading sulfur toward long lifespan cathode materials for Li–S batteries. *J. Mater. Chem. A* **2013**, *1*, 6602-6608.

[56] Jayaprakash, N.; Shen, J.; Moganty, S. S.; Corona, A.; Archer, L. A. Porous Hollow Carbon@Sulfur Composites for High-Power Lithium–Sulfur Batteries. *Angew. Chem. Int. Ed.* **2011**, *50*, 5904-5908.

[57] Lee, T.; Kwon, W.; Kang, H.; Chae, S.; Kim, E.; Kim, J.; Chae, H. G.; Lee, A. S.; Jeong, E.; Lee, J. H.; Lee, S. G. Pyro-polymerization of organic pigments for superior lithium storage. *Carbon* **2022**, *188*, 187-196.

[58] Xu, Q.; Li, Y.; Wu, C.; Sun, X.; Li, Q.; Zhang, H.; Yu, L.; Pan, Y.; Wang, Y.; Guo, S.; Zhang, M.; Hu, H.; Wu, M. Kinetically accelerated and high-mass loaded lithium storage enabled by atomic iron embedded carbon nanofibers. *Nano Res.* **2022**.

[59] Denis, D. K.; Wang, G.; Hou, L.; Chen, G.; Yuan, C. Construction of conductive Ni-Co-molybdate solid-solution nanoparticles encapsulated in carbon nanofibers towards Li-ion batteries as high-rate anodes. *Electrochim. Acta* **2022**, *402*, 139564.

[60] Zhang, W.; Fu, Q.; Chen, X.; Yu, Z.; Jin, Y.; Liu, N.; Sheng, Y.; Xiao, L.; Chen, J. Facile yet versatile assembling of helical carbon nanofibers via metal-organic frameworks burned in ethanol flame and their electrochemical properties as electrode of supercapacitor. *J. Power Sources* **2022**, *521*, 230908.

[61] Peng, H.; Ma, G.; Sun, K.; Mu, J.; Luo, M.; Lei, Z. High-performance aqueous asymmetric supercapacitor based on carbon nanofibers network and tungsten trioxide nanorod bundles electrodes. *Electrochim. Acta* **2014**, *147*, 54-61.

[62] Huang, J.-Q.; Zhang, B.; Xu, Z.-L.; Abouali, S.; Akbari Garakani, M.; Huang, J.; Kim, J.-K. Novel interlayer made from Fe₃C/carbon nanofiber webs for high performance lithium–sulfur batteries. *J. Power Sources* **2015**, *285*, 43-50.

[63] Zhang, B.; Xu, Z.-L.; He, Y.-B.; Abouali, S.; Akbari Garakani, M.; Kamali Heidari, E.; Kang, F.; Kim, J.-K. Exceptional rate performance of functionalized carbon nanofiber anodes containing nanopores created by (Fe) sacrificial catalyst. *Nano Energy* **2014**, *4*, 88-96.

[64] Xu, Z.-L.; Zhang, B.; Kim, J.-K. Electrospun carbon nanofiber anodes containing monodispersed Si nanoparticles and graphene oxide with exceptional high rate capacities. *Nano Energy* **2014**, *6*, 27-35.

[65] Xia, J.; Chen, F.; Li, J.; Tao, N. Measurement of the quantum capacitance of graphene. *Nat. Nanotechnol.* **2009**, *4*, 505-509.

[66] Booth, T. J.; Blake, P.; Nair, R. R.; Jiang, D.; Hill, E. W.; Bangert, U.; Bleloch, A.; Gass, M.; Novoselov, K. S.; Katsnelson, M. I.; Geim, A. K. Macroscopic Graphene Membranes and Their Extraordinary Stiffness. *Nano Lett.* **2008**, *8*, 2442-2446.

- [67] Lee, C.; Wei, X.; Kysar, J. W.; Hone, J. Measurement of the Elastic Properties and Intrinsic Strength of Monolayer Graphene. *Science* **2008**, *321*, 385-388.
- [68] Novoselov, K. S.; Geim, A. K.; Morozov, S. V.; Jiang, D.; Zhang, Y.; Dubonos, S. V.; Grigorieva, I. V.; Firsov, A. A. Electric Field Effect in Atomically Thin Carbon Films. *Science* **2004**, *306*, 666-669.
- [69] Geim, A. K.; Novoselov, K. S. The rise of graphene. *Nat. Mater.* **2007**, *6*, 183-191.
- [70] Ke, Q.; Wang, J. Graphene-based materials for supercapacitor electrodes – A review. *J. Materiomics* **2016**, *2*, 37-54.
- [71] Geim, A. K. Graphene: Status and Prospects. *Science* **2009**, *324*, 1530-1534.
- [72] Geim, A. K. Graphene prehistory. *Phys. Scr.* **2012**, *T146*, 014003.
- [73] León, V.; Quintana, M.; Herrero, M. A.; Fierro, J. L. G.; Hoz, A. d. l.; Prato, M.; Vázquez, E. Few-layer graphenes from ball-milling of graphite with melamine. *Chem. Commun.* **2011**, *47*, 10936-10938.
- [74] León, V.; Rodríguez, A. M.; Prieto, P.; Prato, M.; Vázquez, E. Exfoliation of Graphite with Triazine Derivatives under Ball-Milling Conditions: Preparation of Few-Layer Graphene via Selective Noncovalent Interactions. *ACS Nano* **2014**, *8*, 563-571.
- [75] Teng, C.; Xie, D.; Wang, J.; Yang, Z.; Ren, G.; Zhu, Y. Ultrahigh Conductive Graphene Paper Based on Ball-Milling Exfoliated Graphene. *Adv. Funct. Mater.* **2017**, *27*, 1700240.
- [76] Zhu, Y.; Murali, S.; Cai, W.; Li, X.; Suk, J. W.; Potts, J. R.; Ruoff, R. S. Graphene and Graphene Oxide: Synthesis, Properties, and Applications. *Adv. Mater.* **2010**, *22*, 3906-3924.
- [77] Brodie, B. C. XIII. On the atomic weight of graphite. *Philos. Trans. R. Soc. London* **1859**, *149*, 249-259.
- [78] Hummers Jr, W. S.; Offeman, R. E. Preparation of graphitic oxide. *J. Am. Chem. Soc.* **1958**, *80*, 1339-1339.
- [79] Chen, H.; Li, C.; Qu, L. Solution electrochemical approach to functionalized graphene: History, progress and challenges. *Carbon* **2018**, *140*, 41-56.
- [80] You, X.; Chang, J.-H.; Ju, B. K.; Pak, J. J. An electrochemical route to graphene oxide. *J. Nanosci. Nanotechnol.* **2011**, *11*, 5965-5968.
- [81] Liu, F.; Xue, D. An Electrochemical Route to Quantitative Oxidation of Graphene Frameworks with Controllable C/O Ratios and Added Pseudocapacitances. *Chem. Eur. J.* **2013**, *19*, 10716-10722.
- [82] Ji, L.; Rao, M.; Zheng, H.; Zhang, L.; Li, Y.; Duan, W.; Guo, J.; Cairns, E. J.; Zhang, Y. Graphene Oxide as a Sulfur Immobilizer in High Performance Lithium/Sulfur Cells. *J. Am. Chem. Soc.* **2011**, *133*, 18522-18525.
- [83] Evers, S.; Nazar, L. F. Graphene-enveloped sulfur in a one pot reaction: a cathode with good coulombic efficiency and high practical sulfur content. *Chem. Commun.* **2012**, *48*, 1233-1235.
- [84] Wang, H.; Yang, Y.; Liang, Y.; Robinson, J. T.; Li, Y.; Jackson, A.; Cui, Y.; Dai, H. Graphene-Wrapped Sulfur Particles as a Rechargeable Lithium–Sulfur Battery Cathode Material with High Capacity and Cycling Stability. *Nano Lett.* **2011**, *11*, 2644-2647.
- [85] Li, N.; Zheng, M.; Lu, H.; Hu, Z.; Shen, C.; Chang, X.; Ji, G.; Cao, J.; Shi, Y. High-rate lithium–sulfur batteries promoted by reduced graphene oxide coating. *Chem. Commun.* **2012**, *48*, 4106-4108.
- [86] Zu, C.; Manthiram, A. Hydroxylated Graphene–Sulfur Nanocomposites for High-Rate Lithium–Sulfur Batteries. *Adv. Energy Mater.* **2013**, *3*, 1008-1012.
- [87] Luque, G. L.; Para, M. L.; Primo, E. N.; Bracamonte, M. V.; Otero, M.; Otero, M.; del Carmen Rojas, M.; Soriano, F. J. G.; Lener, G.; Calderón, A., Graphene in Lithium-Ion/Lithium-Sulfur Batteries. In *Advanced Battery Materials*, **2019**; 399-449.

- [88] Zhang, L.; Ji, L.; Glans, P.-A.; Zhang, Y.; Zhu, J.; Guo, J. Electronic structure and chemical bonding of a graphene oxide–sulfur nanocomposite for use in superior performance lithium–sulfur cells. *Phys. Chem. Chem. Phys.* **2012**, *14*, 13670-13675.
- [89] Zhou, W.; Chen, H.; Yu, Y.; Wang, D.; Cui, Z.; DiSalvo, F. J.; Abruña, H. D. Amylopectin Wrapped Graphene Oxide/Sulfur for Improved Cyclability of Lithium–Sulfur Battery. *ACS Nano* **2013**, *7*, 8801-8808.
- [90] Seh, Z. W.; Wang, H.; Liu, N.; Zheng, G.; Li, W.; Yao, H.; Cui, Y. High-capacity Li₂S–graphene oxide composite cathodes with stable cycling performance. *Chem. Sci.* **2014**, *5*, 1396-1400.
- [91] Zheng, S.; Wen, Y.; Zhu, Y.; Han, Z.; Wang, J.; Yang, J.; Wang, C. In Situ Sulfur Reduction and Intercalation of Graphite Oxides for Li-S Battery Cathodes. *Adv. Energy Mater.* **2014**, *4*, 1400482.
- [92] Lin, H.; Yang, L.; Jiang, X.; Li, G.; Zhang, T.; Yao, Q.; Zheng, G. W.; Lee, J. Y. Electrocatalysis of polysulfide conversion by sulfur-deficient MoS₂ nanoflakes for lithium–sulfur batteries. *Energy Environ. Sci.* **2017**, *10*, 1476-1486.
- [93] Huang, X.; Luo, B.; Knibbe, R.; Hu, H.; Lyu, M.; Xiao, M.; Sun, D.; Wang, S.; Wang, L. An Integrated Strategy towards Enhanced Performance of the Lithium–Sulfur Battery and its Fading Mechanism. *Chem. Eur. J.* **2018**, *24*, 18544-18550.
- [94] Jin, K.; Zhou, X.; Liu, Z. Graphene/Sulfur/Carbon Nanocomposite for High Performance Lithium-Sulfur Batteries. *Nanomaterials* **2015**, *5*, 1481-1492.
- [95] Du, W.-C.; Zhang, J.; Yin, Y.-X.; Guo, Y.-G.; Wan, L.-J. Sulfur Confined in Sub-Nanometer-Sized 2D Graphene Interlayers and Its Electrochemical Behavior in Lithium–Sulfur Batteries. *Chem. Asian J.* **2016**, *11*, 2690-2694.
- [96] Lu, S.; Chen, Y.; Wu, X.; Wang, Z.; Li, Y. Three-Dimensional Sulfur/Graphene Multifunctional Hybrid Sponges for Lithium-Sulfur Batteries with Large Areal Mass Loading. *Sci. Rep.* **2014**, *4*, 4629.
- [97] Ahn, W.; Seo, M. H.; Jun, Y.-S.; Lee, D. U.; Hassan, F. M.; Wang, X.; Yu, A.; Chen, Z. Sulfur Nanogranular Film-Coated Three-Dimensional Graphene Sponge-Based High Power Lithium Sulfur Battery. *ACS Appl. Mater. Interfaces* **2016**, *8*, 1984-1991.
- [98] Xing, L.-B.; Xi, K.; Li, Q.; Su, Z.; Lai, C.; Zhao, X.; Kumar, R. V. Nitrogen, sulfur-codoped graphene sponge as electroactive carbon interlayer for high-energy and -power lithium–sulfur batteries. *J. Power Sources* **2016**, *303*, 22-28.
- [99] Jiao, Z.; Chen, L.; Si, J.; Xu, C.; Jiang, Y.; Zhu, Y.; Yang, Y.; Zhao, B. Core-shell Li₂S@Li₃PS₄ nanoparticles incorporated into graphene aerogel for lithium-sulfur batteries with low potential barrier and overpotential. *J. Power Sources* **2017**, *353*, 167-175.
- [100] Ma, Z.; Tao, L.; Liu, D.; Li, Z.; Zhang, Y.; Liu, Z.; Liu, H.; Chen, R.; Huo, J.; Wang, S. Ultrafine nano-sulfur particles anchored on in situ exfoliated graphene for lithium–sulfur batteries. *J. Mater. Chem. A* **2017**, *5*, 9412-9417.
- [101] Zhang, Z.; Kong, L.-L.; Liu, S.; Li, G.-R.; Gao, X.-P. A High-Efficiency Sulfur/Carbon Composite Based on 3D Graphene Nanosheet@Carbon Nanotube Matrix as Cathode for Lithium–Sulfur Battery. *Adv. Energy Mater.* **2017**, *7*, 1602543.
- [102] Tang, C.; Zhang, Q.; Zhao, M.-Q.; Huang, J.-Q.; Cheng, X.-B.; Tian, G.-L.; Peng, H.-J.; Wei, F. Nitrogen-Doped Aligned Carbon Nanotube/Graphene Sandwiches: Facile Catalytic Growth on Bifunctional Natural Catalysts and Their Applications as Scaffolds for High-Rate Lithium-Sulfur Batteries. *Adv. Mater.* **2014**, *26*, 6100-6105.
- [103] Ding, Y.-L.; Kopold, P.; Hahn, K.; van Aken, P. A.; Maier, J.; Yu, Y. Facile Solid-State Growth of 3D Well-Interconnected Nitrogen-Rich Carbon Nanotube–Graphene Hybrid Architectures for Lithium–Sulfur Batteries. *Adv. Funct. Mater.* **2016**, *26*, 1112-1119.

- [104] Shan, J.; Liu, Y.; Su, Y.; Liu, P.; Zhuang, X.; Wu, D.; Zhang, F.; Feng, X. Graphene-directed two-dimensional porous carbon frameworks for high-performance lithium–sulfur battery cathodes. *J. Mater. Chem. A* **2016**, *4*, 314–320.
- [105] Han, K.; Shen, J.; Hao, S.; Ye, H.; Wolverton, C.; Kung, M. C.; Kung, H. H. Free-Standing Nitrogen-doped Graphene Paper as Electrodes for High-Performance Lithium/Dissolved Polysulfide Batteries. *ChemSusChem* **2014**, *7*, 2545–2553.
- [106] Qiu, Y.; Li, W.; Zhao, W.; Li, G.; Hou, Y.; Liu, M.; Zhou, L.; Ye, F.; Li, H.; Wei, Z.; Yang, S.; Duan, W.; Ye, Y.; Guo, J.; Zhang, Y. High-Rate, Ultralong Cycle-Life Lithium/Sulfur Batteries Enabled by Nitrogen-Doped Graphene. *Nano Lett.* **2014**, *14*, 4821–4827.
- [107] Liu, Y.; Qin, X.; Zhang, S.; Liang, G.; Kang, F.; Chen, G.; Li, B. Fe₃O₄-Decorated Porous Graphene Interlayer for High-Performance Lithium–Sulfur Batteries. *ACS Appl. Mater. Interfaces* **2018**, *10*, 26264–26273.
- [108] Sgroi, M. F.; Pullini, D.; Pruna, A. I. Lithium Polysulfide Interaction with Group III Atoms-Doped Graphene: A Computational Insight. *Batteries* **2020**, *6*.
- [109] Kannan, S. K.; Hareendrakrishnakumar, H.; Joseph, M. G. Efficient polysulfide shuttle mitigation by graphene-lithium cobalt vanadate hybrid for advanced lithium-sulfur batteries. *J. Electroanal. Chem.* **2021**, *899*, 115665.
- [110] Maity, A.; Samanta, S.; Chakravorty, D. Silver–Nickel Bimetallic Nanowire-Based Transparent Thin-Film Spin-Glass Systems for Magnetic Sensor Applications. *ACS Appl. Nano Mater.* **2022**.
- [111] Mahato, D.; Gurusamy, T.; Ramanujam, K.; Haridoss, P.; Thomas, T. Unravelling the role of interface of CuO_x-TiO₂ hybrid metal oxide in enhancement of oxygen reduction reaction performance. *Int. J. Hydrogen Energy* **2022**.
- [112] Han, G.; Liu, Y.; Zhang, L.; Kan, E.; Zhang, S.; Tang, J.; Tang, W. MnO₂ Nanorods Intercalating Graphene Oxide/Polyaniline Ternary Composites for Robust High-Performance Supercapacitors. *Sci. Rep.* **2014**, *4*, 4824.
- [113] Tajik, S.; Dubal, D. P.; Gomez-Romero, P.; Yadegari, A.; Rashidi, A.; Nasernejad, B.; Inamuddin; Asiri, A. M. Nanostructured mixed transition metal oxides for high performance asymmetric supercapacitors: Facile synthetic strategy. *Int. J. Hydrogen Energy* **2017**, *42*, 12384–12395.
- [114] Liu, F.; Zeng, L.; Chen, Y.; Zhang, R.; Yang, R.; Pang, J.; Ding, L.; Liu, H.; Zhou, W. Ni-Co-N hybrid porous nanosheets on graphene paper for flexible and editable asymmetric all-solid-state supercapacitors. *Nano Energy* **2019**, *61*, 18–26.
- [115] Li, J.; Du, Z.; Ruther, R. E.; An, S. J.; David, L. A.; Hays, K.; Wood, M.; Phillip, N. D.; Sheng, Y.; Mao, C.; Kalnaus, S.; Daniel, C.; Wood, D. L. Toward Low-Cost, High-Energy Density, and High-Power Density Lithium-Ion Batteries. *JOM* **2017**, *69*, 1484–1496.
- [116] Wu, Y.; Xie, L.; Ming, H.; Guo, Y.; Hwang, J.-Y.; Wang, W.; He, X.; Wang, L.; Alshareef, H. N.; Sun, Y.-K.; Ming, J. An Empirical Model for the Design of Batteries with High Energy Density. *ACS Energy Lett.* **2020**, *5*, 807–816.
- [117] Wang, R.; Luo, C.; Wang, T.; Zhou, G.; Deng, Y.; He, Y.; Zhang, Q.; Kang, F.; Lv, W.; Yang, Q.-H. Bidirectional Catalysts for Liquid–Solid Redox Conversion in Lithium–Sulfur Batteries. *Adv. Mater.* **2020**, *32*, 2000315.
- [118] Gao, L.; Cao, M.; Fu, Y. Q.; Zhong, Z.; Shen, Y.; Wang, M. Hierarchical TiO₂ spheres assisted with graphene for a high performance lithium–sulfur battery. *J. Mater. Chem. A* **2016**, *4*, 16454–16461.
- [119] Wei Seh, Z.; Li, W.; Cha, J. J.; Zheng, G.; Yang, Y.; McDowell, M. T.; Hsu, P.-C.; Cui, Y. Sulphur–TiO₂ yolk–shell nanoarchitecture with internal void space for long-cycle lithium–sulphur batteries. *Nat. Commun.* **2013**, *4*, 1331.
- [120] Cao, K.; Liu, H.; Li, Y.; Wang, Y.; Jiao, L. Encapsulating sulfur in δ-MnO₂ at room temperature for Li-S battery cathode. *Energy Storage Mater.* **2017**, *9*, 78–84.

- [121] Zhong, Y.; Yang, K. R.; Liu, W.; He, P.; Batista, V.; Wang, H. Mechanistic Insights into Surface Chemical Interactions between Lithium Polysulfides and Transition Metal Oxides. *J. Phys. Chem. C* **2017**, *121*, 14222-14227.
- [122] Zhou, G.; Tian, H.; Jin, Y.; Tao, X.; Liu, B.; Zhang, R.; Seh, Z. W.; Zhuo, D.; Liu, Y.; Sun, J.; Zhao, J.; Zu, C.; Wu, D. S.; Zhang, Q.; Cui, Y. Catalytic oxidation of Li₂S on the surface of metal sulfides for Li-S batteries. *Proc. Natl. Acad. Sci. U.S.A.* **2017**, *114*, 840-845.
- [123] Wang, A.; Li, J.; Zhang, T. Heterogeneous single-atom catalysis. *Nat. Rev. Chem.* **2018**, *2*, 65-81.
- [124] Chen, P.; Zhou, T.; Xing, L.; Xu, K.; Tong, Y.; Xie, H.; Zhang, L.; Yan, W.; Chu, W.; Wu, C.; Xie, Y. Atomically Dispersed Iron-Nitrogen Species as Electrocatalysts for Bifunctional Oxygen Evolution and Reduction Reactions. *Angew. Chem. Int. Ed.* **2017**, *56*, 610-614.
- [125] Fei, H.; Dong, J.; Arellano-Jiménez, M. J.; Ye, G.; Dong Kim, N.; Samuel, E. L. G.; Peng, Z.; Zhu, Z.; Qin, F.; Bao, J.; Yacaman, M. J.; Ajayan, P. M.; Chen, D.; Tour, J. M. Atomic cobalt on nitrogen-doped graphene for hydrogen generation. *Nat. Commun.* **2015**, *6*, 8668.
- [126] Yin, P.; Yao, T.; Wu, Y.; Zheng, L.; Lin, Y.; Liu, W.; Ju, H.; Zhu, J.; Hong, X.; Deng, Z.; Zhou, G.; Wei, S.; Li, Y. Single Cobalt Atoms with Precise N-Coordination as Superior Oxygen Reduction Reaction Catalysts. *Angew. Chem. Int. Ed.* **2016**, *55*, 10800-10805.
- [127] Alarawi, A.; Ramalingam, V.; He, J.-H. Recent advances in emerging single atom confined two-dimensional materials for water splitting applications. *Mater. Today Energy* **2019**, *11*, 1-23.
- [128] He, J.; Bhargav, A.; Manthiram, A. High-Energy-Density, Long-Life Lithium-Sulfur Batteries with Practically Necessary Parameters Enabled by Low-Cost Fe-Ni Nanoalloy Catalysts. *ACS Nano* **2021**, *15*, 8583-8591.
- [129] Lei, Z.; Yang, Q.; Xu, Y.; Guo, S.; Sun, W.; Liu, H.; Lv, L.-P.; Zhang, Y.; Wang, Y. Boosting lithium storage in covalent organic framework via activation of 14-electron redox chemistry. *Nat. Commun.* **2018**, *9*, 576.
- [130] Han, D.; Wang, P.; Li, P.; Shi, J.; Liu, J.; Chen, P.; Zhai, L.; Mi, L.; Fu, Y. Homogeneous and Fast Li-Ion Transport Enabled by a Novel Metal-Organic-Framework-Based Succinonitrile Electrolyte for Dendrite-Free Li Deposition. *ACS Appl. Mater. Interfaces* **2021**, *13*, 52688-52696.
- [131] Gong, L.; Yang, X.; Gao, Y.; Yang, G.; Yu, Z.; Fu, X.; Wang, Y.; Qi, D.; Bian, Y.; Wang, K.; Jiang, J. Two-dimensional covalent organic frameworks with p- and bipolar-type redox-active centers for organic high-performance Li-ion battery cathodes. *J. Mater. Chem. A* **2022**, *10*, 16595-16601.
- [132] Huang, K.-X.; Hua, J.; Chang, G.-G.; Li, Z.; Tian, G.; Chen, M.-J.; Li, J.-X.; Ke, S.-C.; Yang, X.-Y.; Chen, B. Confined Thermolysis for Oriented N-Doped Carbon Supported Pd toward Stable Catalytic and Energy Storage Applications. *Small* **2021**, *17*, 2002811.
- [133] Mao, Y.; Li, G.; Guo, Y.; Li, Z.; Liang, C.; Peng, X.; Lin, Z. Foldable interpenetrated metal-organic frameworks/carbon nanotubes thin film for lithium-sulfur batteries. *Nat. Commun.* **2017**, *8*, 14628.
- [134] Jiang, S.; Huang, S.; Yao, M.; Zhu, J.; Liu, L.; Niu, Z. Bimetal-organic frameworks derived Co/N-doped carbons for lithium-sulfur batteries. *Chin. Chem. Lett.* **2020**, *31*, 2347-2352.
- [135] Naguib, M.; Kurtoglu, M.; Presser, V.; Lu, J.; Niu, J.; Heon, M.; Hultman, L.; Gogotsi, Y.; Barsoum, M. W. Two-Dimensional Nanocrystals Produced by Exfoliation of Ti₃AlC₂. *Adv. Mater.* **2011**, *23*, 4248-4253.
- [136] Pai, R.; Natu, V.; Sokol, M.; Carey, M.; Barsoum, M. W.; Kalra, V. Tuning functional two-dimensional MXene nanosheets to enable efficient sulfur utilization in lithium-sulfur batteries. *Cell Rep. Phys. Sci.* **2021**, *2*, 100480.

- [137] Zhao, Q.; Zhu, Q.; Liu, Y.; Xu, B. Status and Prospects of MXene-Based Lithium–Sulfur Batteries. *Adv. Funct. Mater.* **2021**, *31*, 2100457.
- [138] Zhang, Y.; Ma, C.; He, W.; Zhang, C.; Zhou, L.; Wang, G.; Wei, W. MXene and MXene-based materials for lithium-sulfur batteries. *Prog. Nat. Sci.: Mater. Int.* **2021**, *31*, 501-513.
- [139] Zhou, W.; Yu, Y.; Chen, H.; DiSalvo, F. J.; Abruña, H. D. Yolk–Shell Structure of Polyaniline-Coated Sulfur for Lithium–Sulfur Batteries. *J. Am. Chem. Soc.* **2013**, *135*, 16736-16743.
- [140] Xiao, L.; Cao, Y.; Xiao, J.; Schwenzer, B.; Engelhard, M. H.; Saraf, L. V.; Nie, Z.; Exarhos, G. J.; Liu, J. A Soft Approach to Encapsulate Sulfur: Polyaniline Nanotubes for Lithium-Sulfur Batteries with Long Cycle Life. *Adv. Mater.* **2012**, *24*, 1176-1181.
- [141] Xiao, S.; Liu, S.; Zhang, J.; Wang, Y. Polyurethane-derived N-doped porous carbon with interconnected sheet-like structure as polysulfide reservoir for lithium–sulfur batteries. *J. Power Sources* **2015**, *293*, 119-126.
- [142] Lu, Y.; Qin, J.-L.; Shen, T.; Yu, Y.-F.; Chen, K.; Hu, Y.-Z.; Liang, J.-N.; Gong, M.-X.; Zhang, J.-J.; Wang, D.-L. Hypercrosslinked Polymerization Enabled N-Doped Carbon Confined Fe₂O₃ Facilitating Li Polysulfides Interface Conversion for Li–S Batteries. *Adv. Energy Mater.* **2021**, *11*, 2101780.
- [143] Steudel, R.; Eckert, B., Solid Sulfur Allotropes. In *Elemental Sulfur and Sulfur-Rich Compounds I*, Steudel, R., Ed. *Springer Berlin Heidelberg*: Berlin, Heidelberg, **2003**; 1-80.
- [144] Steudel, R., Homocyclic sulfur molecules. In *Inorganic Ring Systems*, *Springer Berlin Heidelberg*: Berlin, Heidelberg, **1982**; 149-176.
- [145] Pai, R.; Singh, A.; Tang, M. H.; Kalra, V. Stabilization of gamma sulfur at room temperature to enable the use of carbonate electrolyte in Li-S batteries. *Commun. Chem.* **2022**, *5*, 17.
- [146] Lacey, M. J.; Jeschull, F.; Edström, K.; Brandell, D. Why PEO as a binder or polymer coating increases capacity in the Li–S system. *Chem. Commun.* **2013**, *49*, 8531-8533.
- [147] Seh, Z. W.; Zhang, Q.; Li, W.; Zheng, G.; Yao, H.; Cui, Y. Stable cycling of lithium sulfide cathodes through strong affinity with a bifunctional binder. *Chem. Sci.* **2013**, *4*, 3673-3677.
- [148] Peled, E.; Goor, M.; Schektman, I.; Mukra, T.; Shoval, Y.; Golodnitsky, D. The Effect of Binders on the Performance and Degradation of the Lithium/Sulfur Battery Assembled in the Discharged State. *J. Electrochem. Soc.* **2016**, *164*, A5001-A5007.
- [149] Chen, W.; Qian, T.; Xiong, J.; Xu, N.; Liu, X.; Liu, J.; Zhou, J.; Shen, X.; Yang, T.; Chen, Y.; Yan, C. A New Type of Multifunctional Polar Binder: Toward Practical Application of High Energy Lithium Sulfur Batteries. *Adv. Mater.* **2017**, *29*, 1605160.
- [150] Su, H.; Fu, C.; Zhao, Y.; Long, D.; Ling, L.; Wong, B. M.; Lu, J.; Guo, J. Polycation Binders: An Effective Approach toward Lithium Polysulfide Sequestration in Li–S Batteries. *ACS Energy Lett.* **2017**, *2*, 2591-2597.
- [151] Huang, Y.; Shaibani, M.; Gamot, T. D.; Wang, M.; Jovanović, P.; Dilusha Cooray, M. C.; Mirshekarloo, M. S.; Mulder, R. J.; Medhekar, N. V.; Hill, M. R.; Majumder, M. A saccharide-based binder for efficient polysulfide regulations in Li-S batteries. *Nat. Commun.* **2021**, *12*, 5375.
- [152] Yang, Y.; Qiu, J.; Cai, L.; Liu, C.; Wu, S.; Wei, X.; Luo, D.; Zhang, B.; Yang, X.; Hui, K. N.; Liu, J.; Lin, Z. Water-Soluble Trifunctional Binder for Sulfur Cathodes for Lithium–Sulfur Battery. *ACS Appl. Mater. Interfaces* **2021**, *13*, 33066-33074.
- [153] Do, V.; Lee, S. H.; Jang, E.; Lee, J.-H.; Lee, J.-W.; Lee, J. T.; Cho, W. I. Aqueous Quaternary Polymer Binder Enabling Long-Life Lithium–Sulfur Batteries by Multifunctional Physicochemical Properties. *ACS Appl. Mater. Interfaces* **2022**.

- [154] Teki, R.; Datta, M. K.; Krishnan, R.; Parker, T. C.; Lu, T.-M.; Kumta, P. N.; Koratkar, N. Nanostructured Silicon Anodes for Lithium Ion Rechargeable Batteries. *Small* **2009**, *5*, 2236-2242.
- [155] Lee, Y.-G.; Fujiki, S.; Jung, C.; Suzuki, N.; Yashiro, N.; Omoda, R.; Ko, D.-S.; Shiratsuchi, T.; Sugimoto, T.; Ryu, S.; Ku, J. H.; Watanabe, T.; Park, Y.; Aihara, Y.; Im, D.; Han, I. T. High-energy long-cycling all-solid-state lithium metal batteries enabled by silver-carbon composite anodes. *Nat. Energy* **2020**, *5*, 299-308.
- [156] Karabelli, D.; Birke, K. P., Feasible Energy Density Pushes of Li-Metal vs. Li-Ion Cells. **2021**; Vol. 11.
- [157] Xie, J.; Lu, Y.-C. A retrospective on lithium-ion batteries. *Nat. Commun.* **2020**, *11*, 2499.
- [158] Peled, E. The Electrochemical Behavior of Alkali and Alkaline Earth Metals in Nonaqueous Battery Systems—The Solid Electrolyte Interphase Model. *J. Electrochem. Soc.* **1979**, *126*, 2047.
- [159] Ji, X.; Liu, D.-Y.; Prendiville, D. G.; Zhang, Y.; Liu, X.; Stucky, G. D. Spatially heterogeneous carbon-fiber papers as surface dendrite-free current collectors for lithium deposition. *Nano Today* **2012**, *7*, 10-20.
- [160] Zhamu, A.; Chen, G.; Liu, C.; Neff, D.; Fang, Q.; Yu, Z.; Xiong, W.; Wang, Y.; Wang, X.; Jang, B. Z. Reviving rechargeable lithium metal batteries: enabling next-generation high-energy and high-power cells. *Energy Environ. Sci.* **2012**, *5*, 5701-5707.
- [161] Kim, H.; Jeong, G.; Kim, Y.-U.; Kim, J.-H.; Park, C.-M.; Sohn, H.-J. Metallic anodes for next generation secondary batteries. *Chem. Soc. Rev.* **2013**, *42*, 9011-9034.
- [162] Aurbach, D.; Pollak, E.; Elazari, R.; Salitra, G.; Kelley, C. S.; Affinito, J. On the Surface Chemical Aspects of Very High Energy Density, Rechargeable Li-Sulfur Batteries. *J. Electrochem. Soc.* **2009**, *156*, A694.
- [163] Besenhard, J. O. The electrochemical preparation and properties of ionic alkali metal- and NR₄-graphite intercalation compounds in organic electrolytes. *Carbon* **1976**, *14*, 111-115.
- [164] Aurbach, D.; Markovsky, B.; Weissman, I.; Levi, E.; Ein-Eli, Y. On the correlation between surface chemistry and performance of graphite negative electrodes for Li ion batteries. *Electrochim. Acta* **1999**, *45*, 67-86.
- [165] Brückner, J.; Thieme, S.; Böttger-Hiller, F.; Bauer, I.; Grossmann, H. T.; Strubel, P.; Althues, H.; Spange, S.; Kaskel, S. Carbon-Based Anodes for Lithium Sulfur Full Cells with High Cycle Stability. *Adv. Funct. Mater.* **2014**, *24*, 1284-1289.
- [166] Kasavajjula, U.; Wang, C.; Appleby, A. J. Nano- and bulk-silicon-based insertion anodes for lithium-ion secondary cells. *J. Power Sources* **2007**, *163*, 1003-1039.
- [167] Park, C.-M.; Kim, J.-H.; Kim, H.; Sohn, H.-J. Li-alloy based anode materials for Li secondary batteries. *Chem. Soc. Rev.* **2010**, *39*, 3115-3141.
- [168] Li, H.; Wang, Z.; Chen, L.; Huang, X. Research on Advanced Materials for Li-ion Batteries. *Adv. Mater.* **2009**, *21*, 4593-4607.
- [169] Hassoun, J.; Kim, J.; Lee, D.-J.; Jung, H.-G.; Lee, S.-M.; Sun, Y.-K.; Scrosati, B. A contribution to the progress of high energy batteries: A metal-free, lithium-ion, silicon-sulfur battery. *J. Power Sources* **2012**, *202*, 308-313.
- [170] Yan, Y.; Yin, Y.-X.; Xin, S.; Su, J.; Guo, Y.-G.; Wan, L.-J. High-safety lithium-sulfur battery with prelithiated Si/C anode and ionic liquid electrolyte. *Electrochim. Acta* **2013**, *91*, 58-61.
- [171] Peled, E.; Sternberg, Y.; Gorenshstein, A.; Lavi, Y. Lithium-Sulfur Battery: Evaluation of Dioxolane-Based Electrolytes. *J. Electrochem. Soc.* **1989**, *136*, 1621.
- [172] Chang, D.-R.; Lee, S.-H.; Kim, S.-W.; Kim, H.-T. Binary electrolyte based on tetra(ethylene glycol) dimethyl ether and 1,3-dioxolane for lithium-sulfur battery. *J. Power Sources* **2002**, *112*, 452-460.

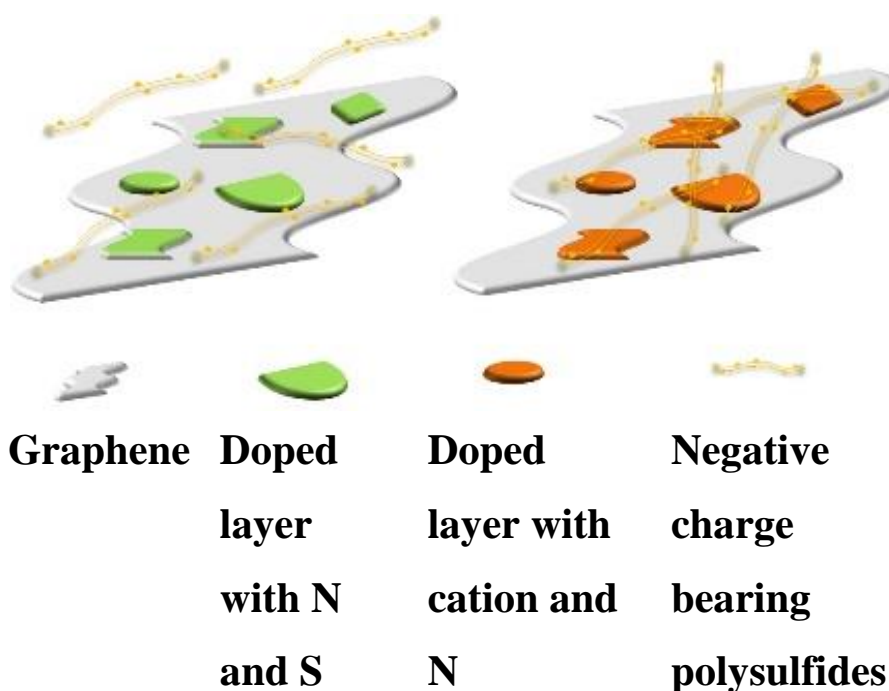
- [173] Ryu, H. S.; Ahn, H. J.; Kim, K. W.; Ahn, J. H.; Cho, K. K.; Nam, T. H. Self-discharge characteristics of lithium/sulfur batteries using TEGDME liquid electrolyte. *Electrochim. Acta* **2006**, *52*, 1563-1566.
- [174] Suo, L.; Hu, Y.-S.; Li, H.; Armand, M.; Chen, L. A new class of Solvent-in-Salt electrolyte for high-energy rechargeable metallic lithium batteries. *Nat. Commun.* **2013**, *4*, 1481.
- [175] Zheng, J.; Ji, G.; Fan, X.; Chen, J.; Li, Q.; Wang, H.; Yang, Y.; DeMella, K. C.; Raghavan, S. R.; Wang, C. High-Fluorinated Electrolytes for Li-S Batteries. *Adv. Energy Mater.* **2019**, *9*, 1803774.
- [176] Lin, Y.; Huang, S.; Zhong, L.; Wang, S.; Han, D.; Ren, S.; Xiao, M.; Meng, Y. Organic liquid electrolytes in Li-S batteries: actualities and perspectives. *Energy Storage Mater.* **2021**, *34*, 128-147.
- [177] Gao, J.; Lowe, M. A.; Kiya, Y.; Abruña, H. D. Effects of Liquid Electrolytes on the Charge-Discharge Performance of Rechargeable Lithium/Sulfur Batteries: Electrochemical and in-Situ X-ray Absorption Spectroscopic Studies. *J. Phys. Chem. C* **2011**, *115*, 25132-25137.
- [178] Barchasz, C.; Leprêtre, J.-C.; Patoux, S.; Alloin, F. Electrochemical properties of ether-based electrolytes for lithium/sulfur rechargeable batteries. *Electrochim. Acta* **2013**, *89*, 737-743.
- [179] Zhang, B.; Lai, C.; Zhou, Z.; Gao, X. P. Preparation and electrochemical properties of sulfur-acetylene black composites as cathode materials. *Electrochim. Acta* **2009**, *54*, 3708-3713.
- [180] Lin, F.; Wang, J.; Jia, H.; Monroe, C. W.; Yang, J.; NuLi, Y. Nonflammable electrolyte for rechargeable lithium battery with sulfur based composite cathode materials. *J. Power Sources* **2013**, *223*, 18-22.
- [181] Haruna, A. B.; Mofokeng, T. P.; Ogada, J. J.; Zoubir, O.; Lallaoui, A.; Cherkaoui El Moursli, F.; Edfouf, Z.; Ozoemena, K. I. Recent advances in the cathode materials and solid-state electrolytes for lithium sulfur batteries. *Electrochem. Commun.* **2022**, *136*, 107248.
- [182] Yang, X.; Luo, J.; Sun, X. Towards high-performance solid-state Li-S batteries: from fundamental understanding to engineering design. *Chem. Soc. Rev.* **2020**, *49*, 2140-2195.
- [183] Marmorstein, D.; Yu, T. H.; Striebel, K. A.; McLarnon, F. R.; Hou, J.; Cairns, E. J. Electrochemical performance of lithium/sulfur cells with three different polymer electrolytes. *J. Power Sources* **2000**, *89*, 219-226.
- [184] Kim, J.; Lee, D.-J.; Jung, H.-G.; Sun, Y.-K.; Hassoun, J.; Scrosati, B. An Advanced Lithium-Sulfur Battery. *Adv. Funct. Mater.* **2013**, *23*, 1076-1080.
- [185] Hayashi, A.; Ohtomo, T.; Mizuno, F.; Tadanaga, K.; Tatsumisago, M. All-solid-state Li/S batteries with highly conductive glass-ceramic electrolytes. *Electrochem. Commun.* **2003**, *5*, 701-705.
- [186] Xu, R.-c.; Xia, X.-h.; Wang, X.-l.; Xia, Y.; Tu, J.-p. Tailored Li₂S-P₂S₅ glass-ceramic electrolyte by MoS₂ doping, possessing high ionic conductivity for all-solid-state lithium-sulfur batteries. *J. Mater. Chem. A* **2017**, *5*, 2829-2834.
- [187] Lu, Y.; Huang, X.; Song, Z.; Rui, K.; Wang, Q.; Gu, S.; Yang, J.; Xiu, T.; Badding, M. E.; Wen, Z. Highly stable garnet solid electrolyte based Li-S battery with modified anodic and cathodic interfaces. *Energy Storage Mater.* **2018**, *15*, 282-290.
- [188] Elizalde-Segovia, R.; Irshad, A.; Zayat, B.; Narayanan, S. R. Solid-State Lithium-Sulfur Battery Based on Composite Electrode and Bi-layer Solid Electrolyte Operable at Room Temperature. *J. Electrochem. Soc.* **2020**, *167*, 140529.
- [189] Rao, M. L. B. Organic electrolyte cells. *U.S. Patent* **1968**, 3,413,154.
- [190] Mikhaylik, Y. V. Electrolytes for lithium sulfur cells. *U.S. Patent* **2008**, 7,352,680.

- [191] Liang, X.; Wen, Z.; Liu, Y.; Wu, M.; Jin, J.; Zhang, H.; Wu, X. Improved cycling performances of lithium sulfur batteries with LiNO₃-modified electrolyte. *J. Power Sources* **2011**, *196*, 9839-9843.
- [192] Zhang, S. S. Role of LiNO₃ in rechargeable lithium/sulfur battery. *Electrochim. Acta* **2012**, *70*, 344-348.
- [193] Zhang, S. S. Effect of Discharge Cutoff Voltage on Reversibility of Lithium/Sulfur Batteries with LiNO₃-Contained Electrolyte. *J. Electrochem. Soc.* **2012**, *159*, A920-A923.
- [194] Deimede, V.; Elmasides, C. Separators for Lithium-Ion Batteries: A Review on the Production Processes and Recent Developments. *Energy Technol.* **2015**, *3*, 453-468.
- [195] Chung, S.-H.; Manthiram, A. Bifunctional Separator with a Light-Weight Carbon-Coating for Dynamically and Statically Stable Lithium-Sulfur Batteries. *Adv. Funct. Mater.* **2014**, *24*, 5299-5306.
- [196] Balach, J.; Singh, H. K.; Gomoll, S.; Jaumann, T.; Klose, M.; Oswald, S.; Richter, M.; Eckert, J.; Giebeler, L. Synergistically Enhanced Polysulfide Chemisorption Using a Flexible Hybrid Separator with N and S Dual-Doped Mesoporous Carbon Coating for Advanced Lithium-Sulfur Batteries. *ACS Appl. Mater. Interfaces* **2016**, *8*, 14586-14595.
- [197] Lei, T.; Chen, W.; Lv, W.; Huang, J.; Zhu, J.; Chu, J.; Yan, C.; Wu, C.; Yan, Y.; He, W.; Xiong, J.; Li, Y.; Yan, C.; Goodenough, J. B.; Duan, X. Inhibiting Polysulfide Shuttling with a Graphene Composite Separator for Highly Robust Lithium-Sulfur Batteries. *Joule* **2018**, *2*, 2091-2104.
- [198] Zhou, G.; Li, L.; Wang, D.-W.; Shan, X.-y.; Pei, S.; Li, F.; Cheng, H.-M. A Flexible Sulfur-Graphene-Polypropylene Separator Integrated Electrode for Advanced Li-S Batteries. *Adv. Mater.* **2015**, *27*, 641-647.
- [199] Ponnada, S.; Kiai, M. S.; Gorle, D. B.; Nowduri, A. Application of Facile Graphene Oxide Binders with Nanocomposites for Efficient Separator Performance in Lithium Sulfur Batteries. *Energy Fuels* **2021**, *35*, 12619-12627.
- [200] Kong, L.; Peng, H.-J.; Huang, J.-Q.; Zhu, W.; Zhang, G.; Zhang, Z.-W.; Zhai, P.-Y.; Sun, P.; Xie, J.; Zhang, Q. Beaver-dam-like membrane: A robust and sulphidic MgBO₂(OH)/CNT/PP nest separator in Li-S batteries. *Energy Storage Mater.* **2017**, *8*, 153-160.
- [201] Chen, X.; Ding, X.; Wang, C.; Feng, Z.; Xu, L.; Gao, X.; Zhai, Y.; Wang, D. A multi-shelled CoP nanosphere modified separator for highly efficient Li-S batteries. *Nanoscale* **2018**, *10*, 13694-13701.
- [202] Wang, S.; Gao, F.; Ma, R.; Du, A.; Tan, T.; Du, M.; Zhao, X.; Fan, Y.; Wen, M. ZnO Nanoparticles Anchored on a N-Doped Graphene-Coated Separator for High Performance Lithium/Sulfur Batteries. *Metals* **2018**, *8*.
- [203] Wang, M.-Y.; Han, S.-H.; Chao, Z.-S.; Li, S.-Y.; Tan, B.; Lai, J.-X.; Guo, Z.-Y.; Wei, X.-L.; Jin, H.-G.; Luo, W.-B.; Yi, W.-J.; Fan, J.-C. Celgard-supported LiX zeolite membrane as ion-permselective separator in lithium sulfur battery. *J. Membr. Sci.* **2020**, *611*, 118386.
- [204] Yan, G.; Xu, C.; Meng, Z.; Hou, M.; Yan, W.; Lin, N.; Lai, L.; Zhan, D. A TiS₂/Celgard separator as an efficient polysulfide shuttling inhibitor for high-performance lithium-sulfur batteries. *Nanoscale* **2020**, *12*, 24368-24375.
- [205] Hong, X.-J.; Song, C.-L.; Wu, Z.-M.; Li, Z.-H.; Cai, Y.-P.; Wang, C.-X.; Wang, H. Sulfophilic and lithophilic sites in bimetal nickel-zinc carbide with fast conversion of polysulfides for high-rate Li-S battery. *Chem. Eng. J.* **2021**, *404*, 126566.
- [206] Zhou, H.-J.; Zhang, X.-L.; Zou, M.-Y.; Gu, S.-T.; Cai, Y.-P.; Hong, X.-J. MOF-Derived Bimetal ZnPd Alloy as a Separator Coating with Fast Catalysis of Lithium Polysulfides for Li-S Batteries. *ACS Appl. Energy Mater.* **2021**, *4*, 13183-13190.

- [207] Xie, F.; Xiong, M.; Liu, J.; Qian, J.; Mei, T.; Li, J.; Wang, J.; Yu, L.; Hofmann, J. P.; Wang, X. A multi-functional separator for Li-S batteries: WS₂@C nanoflowers catalyze the rapid recycling of lithium polysulfides by polar attraction. *ChemElectroChem* **2022**, *9*.
- [208] Bai, S.; Liu, X.; Zhu, K.; Wu, S.; Zhou, H. Metal–organic framework-based separator for lithium–sulfur batteries. *Nat. Energy* **2016**, *1*, 16094.
- [209] Freitag, A.; Langklotz, U.; Rost, A.; Stamm, M.; Ionov, L. Ionically conductive polymer/ceramic separator for lithium-sulfur batteries. *Energy Storage Mater.* **2017**, *9*, 105-111.
- [210] Hong, X.-J.; Song, C.-L.; Yang, Y.; Tan, H.-C.; Li, G.-H.; Cai, Y.-P.; Wang, H. Cerium Based Metal–Organic Frameworks as an Efficient Separator Coating Catalyzing the Conversion of Polysulfides for High Performance Lithium–Sulfur Batteries. *ACS Nano* **2019**, *13*, 1923-1931.
- [211] Xu, Q.; Zhang, K.; Qian, J.; Guo, Y.; Song, X.; Pan, H.; Wang, D.; Li, X. Boosting Lithium–Sulfur Battery Performance by Integrating a Redox-Active Covalent Organic Framework in the Separator. *ACS Appl. Energy Mater.* **2019**, *2*, 5793-5798.
- [212] Hareendrakrishnakumar, H.; Chulliyote, R.; Joseph, M. G. Ion-selective PEDOT:PSS-decorated separator as a potential polysulfide immobilizer for lithium-sulfur batteries. *Ionics* **2021**, *27*, 1087-1099.

Chapter 2

2 Concurrent Polyvalent Interaction and Electrocatalysis to Improve Lithium-Sulfur Battery Performance



The content in this chapter is published in the following article.

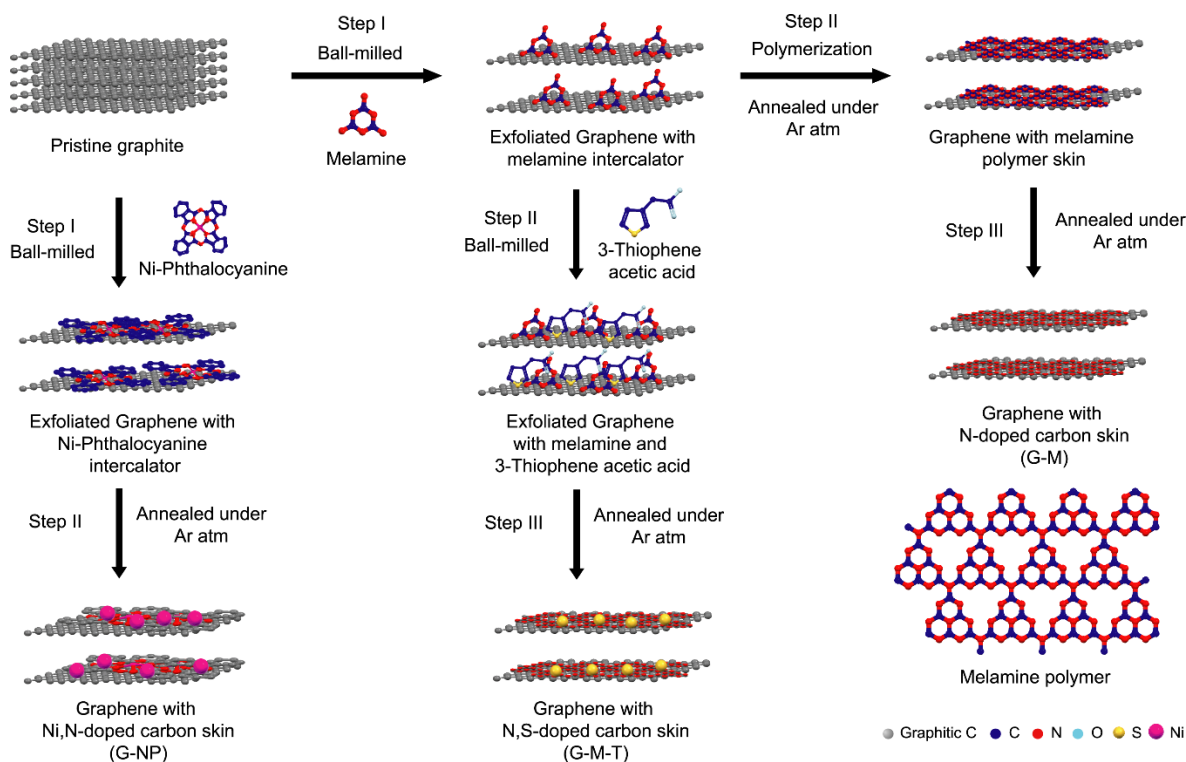
Kumar, S.; Krishnamoorthy, K. *Batteries & Supercaps* **2021**, *5*, e202100229.

(<https://chemistry-europe.onlinelibrary.wiley.com/doi/10.1002/batt.202100229>)

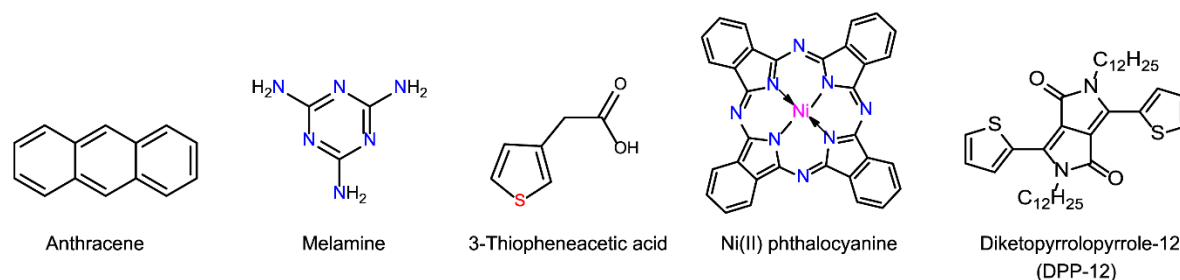
2.1 Introduction

Battery systems with significantly improved energy density and power density over the existing lithium-ion batteries are of great interest. Li-S batteries with theoretical specific capacity of 1675 mAh g⁻¹ and energy density up to 2600 Wh kg⁻¹ are attractive energy storage devices.[1-11] Despite the promise, Li-S batteries are plagued with issues such as poor electrical conductivity of sulfur (5 x 10⁻³⁰ S cm⁻¹), sluggish sulfur redox reaction and dissolution of polysulfide in the battery electrolyte.[12,13] The poor electrical conductivity issue is tackled by preparing carbon composite electrodes.[14-17] The sluggish redox reaction and dissolution of polysulfide remain as challenges.[18-20] The two major approaches to circumvent the dissolution of polysulfide, which is commonly known as the shuttle effect can be classified into, (i) separator modification and (ii) electrode modification. First, the separator membranes are modified with carbon allotropes, polymers and nanostructures. The modified membranes repel the polysulfides and suppress the deleterious shuttle effect.[21,22] In the second approach, porous structures of organic and inorganic materials have been used to confine the sulfur. The pores that are used to load the sulfur also render the possibility of diffusion of polysulfides from the confining material.[23-25] Thus, the confinement approach has its limitations. Li-S battery metrics of various materials are summarized in Table 2.2.

Usually, the battery electrode is prepared by blending sulfur, polymer binder and conducting carbon.[21] Neither the conducting carbon nor the binder is effective in suppressing the polysulfide dissolution.[26-28] Thus, an additive is required. The additive should be a material with properties to withhold the polysulfide from dissolving in the electrolyte. With its excellent properties and easy synthesis, graphene seems to be an attractive candidate.[29] However, the surface of graphene is hydrophobic; hence it is not suitable to withhold polysulfide.[30,31] Therefore, modification of graphene is required. Doped graphene is an option.[32-37] It has been used as additive in the Li-S batteries. All the doped graphene do not have the desired effect. For example, pyridinic and graphitic nitrogen comprising graphenes are better electrocatalysts than pyrrolic nitrogen-containing graphene.[38-40] The pyridinic and pyrrolic nitrogens are Lewis base and they can attract Lewis acid such as polysulfides. However, it has been shown that the pyridinic nitrogens are present either on the edges or at the defect sites of graphene, which is a limitation. Thus, an approach that renders the possibility of preparing



Scheme 2.1. Cartoon showing the steps involved in the preparation of DLC-G.



Scheme 2.2. Chemical Structures of exfoliators (Anthracene, Melamine, 3-Thiopheneacetic acid, Ni(II) phthalocyanine) and DPP-12.

graphene without defect but with pyridinic and graphitic nitrogen is essential. To accomplish this paradoxical objective, we resorted to an approach that mechanically peels off graphene from graphite in presence of exfoliator. The exfoliator molecules that adhere to the graphene surface have been judiciously chosen to have desired dopant atoms. The graphene preparation approach is mechanical; hence the graphene's basal plane is unaffected.[41-44] In the first set of experiments, melamine (Scheme 2.1) was used as exfoliator. Graphite and melamine are ball-milled in planetary ball milling equipment. After exfoliation, the samples were subjected to thermal treatment. During this process, melamine undergoes thermal polymerization leading to a cross-linked polymer that can act as a source of nitrogen-doped carbon.[45] Upon further heating, we envisioned graphenes with a layer comprising pyridinic and graphitic nitrogen (Scheme 2.1). We reiterate that a minimal amount of defects are anticipated in the basal plan

of graphene because the exfoliation is mechanical. Dual doping can enhance electrocatalysis,[46-48] hence we prepared graphenes with layers comprising S (Sulfur) and N (Nitrogen) atoms. These modified graphenes are expected to electrocatalyze the sluggish polysulfide redox reaction.[49] We understand that the N and S comprising graphene layer alter the surface properties, but the interaction between polysulfide and graphene is weak. The sulfur undergoes various structural changes; hence covalent immobilization is not an option. Therefore, we need to rely on non-covalent, yet strong interaction. The negative charges on polysulfide render the possibility to anchor them on graphenes' surface non-covalently. In order to achieve this objective, we must prepare graphene layer with positive charges. Our approach, mechanical exfoliation, renders the possibility of embedding cations on the layer of graphene. To embed cations on the layer of graphene, graphite was ball milled with Nickel Phthalocyanine (Scheme 2.1). During the milling process, Nickel-Ph molecules adhere to graphenes' surface. Subsequent heating of the sample resulted in the formation of graphenes with a carbon layer comprising nickel ions and nitrogens. The nitrogen-doped carbon layer is expected to catalyze the sulfur redox reactions[50-52], concurrently the nickel ions are expected to suppress polysulfide dissolution due to electrostatic polyvalent interaction.[53] Indeed, the Nickel (Ni) ion and N containing carbon layer exhibit superior battery performance that is reported in this research chapter.

2.2 Experimental Section

2.2.1 Materials

Graphite powder (Sigma-Aldrich, <20 μm), Melamine (Alfa Aesar, 99%), Anthracene (Alfa Aesar, 99%), Ni-Phthalocyanine (Sigma-Aldrich, Dye content ca. 85%), 3-Thiopheneacetic acid (Sigma-Aldrich, 99%), Dimethylformamide (DMF, Merck, AR grade), Triton X -100 (Sigma-Aldrich, LR grade), Sodium thiosulfate (anhydrous, 99%), Hydrochloric acid (HCl, Merck, AR grade, 37%), Super P carbon (Imerys Graphite & Carbon Switzerland Ltd., Switzerland), Poly(vinylidene fluoride) (PVDF, Kynar HSV900, Arkema Inc., USA), N-Methyl-2-pyrrolidone (NMP, Merck, AR grade), Celgard 2325 (Polypore, USA), Bis(trifluoromethane)sulfonimide lithium salt (LiTFSI, Sigma-Aldrich, 99.95%), Lithium nitrate (LiNO_3 , Sigma-Aldrich, 99.99%), 1,3-dioxolane (DOL, Sigma-Aldrich, 99.8%), 1,2-dimethoxyethane (DME, Sigma-Aldrich, 99.5%) and Chloroform (Merck, AR grade) were purchased and used without further purification.

2.2.2 Instrumentations

The TEM images were recorded with Tecnai G2 20 S-TWIN transmission electron microscope and HR-TEM images were recorded with a Jeol 1200 EX transmission electron microscope. The carbon-coated copper grids (400 grids) were obtained from Ted Pella. E-SEM images were recorded using Quanta 200 and FE-SEM images were recorded with Nova Nano 450, both the instruments from the FEI company. The sample preparation for TEM and SEM were performed by preparing the 1 mg of sample dispersed in DMF and drop cast on the carbon-coated copper grid and silicon wafer are respectively. After the solvent evaporation, the substrates were kept at 40 °C for 12 h and then performed the characterizations. The Raman spectroscopy measurements were performed with the help of a LabRam spectrometer (HJY, France) equipped with a laser wavelength of 632 nm. PANalytical instrument was operated using Cu K α radiation ($\lambda = 1.542 \text{ \AA}$) at a scanning rate of 2° min^{-1} and a step size of 0.02° in 2θ with operating voltage 40 kV and operating current 30 mA to acquire the X-ray diffraction spectra. XPS measurements for the materials were done on Thermo Kalpha+ spectrometer using Al K α radiation with an energy of 1486.6 eV. All the spectra were charge corrected with reference to C1s at 284.6 eV. The peak fittings were carried out using CasaXPS software. Thermogravimetric analyzes were carried out on SDTQ600 TG-DTA analyzer in a nitrogen environment with a ramp of $5^\circ \text{ C min}^{-1}$.

2.2.3 Synthesis

Graphite exfoliation: The few-layer Graphene was prepared through a mechanical exfoliation process using the planetary mill (*FRITSCH, PULVERISETTE 6*). The graphite powder was exfoliated using various exfoliating agents such as Melamine, Anthracene and Ni-Phthalocyanine (Scheme 2.2).

Sample 1-4: Graphite powder (1.5 g) and Melamine (7.5 g) were placed in an Agate ball mill grinder (250 mL) with six balls (1 cm diameter). The ball milling conditions are mentioned in Table 2.1 for respective samples. The as-prepared material was washed with a copious amount of Dimethylformamide (DMF) for an hour to remove the excess amount of melamine present in it and filtered and dried at 60 °C under vacuum for 16 h.

Sample 5-8: Graphite powder (1.5 g) and Anthracene (7.5 g) were chosen and followed the same procedure and the milling conditions were mentioned in Table 2.1.

Sample 9-12: Graphite powder (1.5 g) and Ni-Phthalocyanine (7.5 g) were used and followed the same procedure and the milling conditions were mentioned in Table 2.1.

Synthesis of G-M, G-M-T, G-A and G-NP: G-M was obtained by carbonizing sample 4 at 600 °C under inert atmosphere for 4 h with heat flow of 5 °C min⁻¹. For G-M-T, Sample 4 (9 g) was further ball milled with 3-Thiophene acetic acid (4.5 g) for 60 min with the speed of 200 rpm, washed with DMF, filtered and dried at 60 °C under vacuum for 16 h. Then carried out for carbonization at 600 °C under inert atmosphere for 4 h with heat flow of 5 °C min⁻¹. G-A was obtained by carbonizing sample 8 at 600 °C under an Argon atmosphere for 4 h with heat flow of 5 °C min⁻¹. For G-NP, Sample 12 was carbonized at 600 °C under inert atmosphere for 4 h with the heat flow of 5 °C min⁻¹.

Synthesis of Sulfur composite materials: The Sulfur particles were synthesized by the wet chemical process. In this method, 9 mL of Triton X -100 (1 wt %) was added into aqueous Sodium thiosulfate (300 mL, 0.05 M) and the solution was heated at 70 °C, followed by 10% HCl solution (30 mL) was drop-wise added into the above solution under vigorous magnetic stirring. The suspension of various doped layer comprising Graphenes' (DLC-Gs) (72 mg) in 100 mL of de-ionized water, was added drop-wise under magnetic stirring. After 15 min, the solution was cooled down to room temperature, filtered under vacuum with a substantial amount of de-ionized water, dried at 60 °C for 16 h.

2.3 Results and Discussion

Graphite was ball milled with melamine (exfoliator) at various revolutions per minute (RPM). We also varied the duration of the ball milling. In another set of experiments, anthracene (control molecule, Scheme 2.2) was used as an exfoliator (Table 2.1). To better understand the role of heteroatoms anthracene has been chosen as a control molecule due to absence of heteroatoms. After the ball milling, the samples were washed extensively with a DMF to remove excess exfoliators. The results and discussions are divided into four sections. First, we discuss the characterization of graphene with an exfoliator. In the next section, the preparation and characterization of DLC-Gs are discussed. Subsequently, battery fabrication and testing are discussed. In the fourth section, we will discuss the preparation and characterization of DLC-G with Ni (Nickel) ions and battery performance using the same material.

2.3.1 Raman spectroscopy

After ball milling and washing, the samples were subjected to Raman spectroscopic analysis. Intense G and 2D bands appeared at 1581 cm⁻¹ and 2676 cm⁻¹, respectively (Figure 2.1). D band appeared at 1335 cm⁻¹ and D' shoulder appeared at 1616 cm⁻¹. The intensity of D and G bands (I_D/I_G) ratio provides information about the graphene layers.[41,54] High I_D/I_G value is

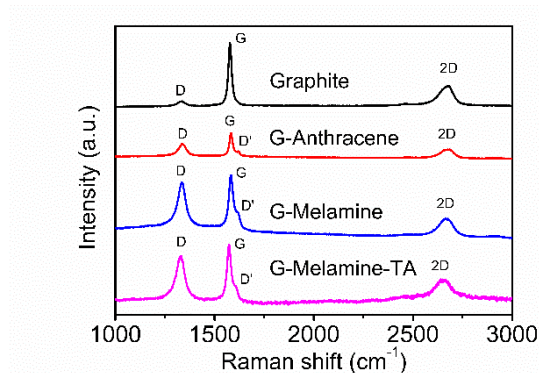


Figure 2.1. Raman spectra showing D, D', G and 2D bands for Graphite, G-A, G-M and G-M-T.

Table 2.1. Milling conditions and obtained I_D/I_G and $I_D/I_{D'}$ from Raman spectra and d-spacing from XRD pattern

Sample ^[a]	Milling conditions	I_D/I_G	$I_D/I_{D'}$	d-spacing
Sample 1	100 rpm, 30 min	0.57	1.3	3.34
Sample 2	100 rpm, 60 min	0.63	1.7	3.37
Sample 3	200 rpm, 30 min	0.72	1.3	3.36
Sample 4	200 rpm, 60 min	0.90	1.8	3.36
Sample 5	100 rpm, 30 min	0.27	1.5	3.48
Sample 6	100 rpm, 60 min	0.28	1.3	3.45
Sample 7	200 rpm, 30 min	0.55	1.5	3.48
Sample 8	200 rpm, 60 min	0.63	1.6	3.48
Sample 9	100 rpm, 30 min	0.10	0.7	3.38
Sample 10	100 rpm, 60 min	0.31	1.5	3.35
Sample 11	200 rpm, 30 min	0.51	0.9	3.36
Sample 12	200 rpm, 60 min	0.48	1.8	3.36

^[a]Samples 1-4 are (Graphite/Melamine), Samples 5-8 are (Graphite/Anthracene) and Samples 9-12 are (Graphite/Ni-Phthalocyanine)

an indication of fewer layer graphenes. The highest I_D/I_G of 0.90 was found while melamine was used as exfoliator with RPM of 200. The duration of the milling was 60 min. All the

parameters used for milling and the properties of resultant materials are listed in Table 2.1. The I_D/I_G provides information about defects in the graphene. I_D/I_G of 3.5 or lower indicates edge and boundary defects with no sp^3 defects.[55,56] All the samples showed I_D/I_G less than 3.5 indicating the formation of high-quality graphenes while using melamine and anthracene as exfoliators (Table 2.1).

2.3.2 X-ray diffraction analysis

The above prepared samples were subjected to X-ray diffraction (XRD) analysis, which is an effective method to identify the formation of graphene from graphite through the mechanical exfoliation process. Graphene shows an intense peak at 2θ of 26.6° that corresponds to 002 plane (Figure 2.2).[42] The d-spacing for graphite was found to be 3.347 \AA , which increased to 3.377 \AA while using melamine as an exfoliator. This was further increased to 3.384 \AA while using anthracene as an exfoliator. Thus, the exfoliators increase the distance between the layers of graphene.

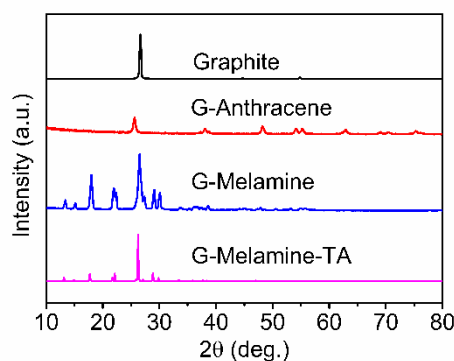


Figure 2.2. XRD pattern for Graphite, G-A, G-M and G-M-T.

2.3.3 X-ray photoelectron spectroscopy

After heating, the samples were subjected to X-ray photoelectron spectroscopic (XPS) analysis. The XPS spectra of graphite showed the presence of sp^2 C (284.6 eV). We also found a peak corresponding to $-C-O-$ (285.6 eV). The small peak at 283.8 eV is due to disordered carbon (Figure 2.3a).[57] The G-A also showed these peaks indicating the absence of any new heteroatoms due to the lack of them in anthracene. The XPS spectra of G-M showed N1s peak at 399 eV and other characteristic peaks as found in G-A. As mentioned in the introduction section, three types of nitrogens are present in doped graphenes. We anticipate those in the DLC-G. In the case of G-M, the pyridinic nitrogen is lowest at 24.8% , and the pyrrolic nitrogen is highest at 36.1% . In the case of G-M-T, the graphitic nitrogen is highest at 40.9% , and the

pyridinic nitrogen is 13.5%. The high graphitic nitrogen in G-M-T may lead to better electrocatalytic activity (Figure 2.3b).

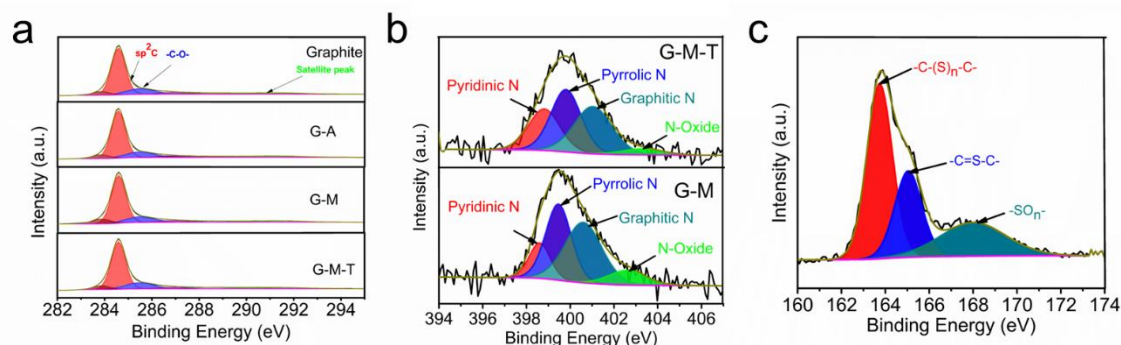


Figure 2.3. XPS spectra of pristine graphite, few-layer graphenes G-A, G-M and G-M-T (a), deconvoluted peaks of the Nitrogen region for G-M and G-M-T (b), and Sulfur deconvolution curves of G-M-T (c).

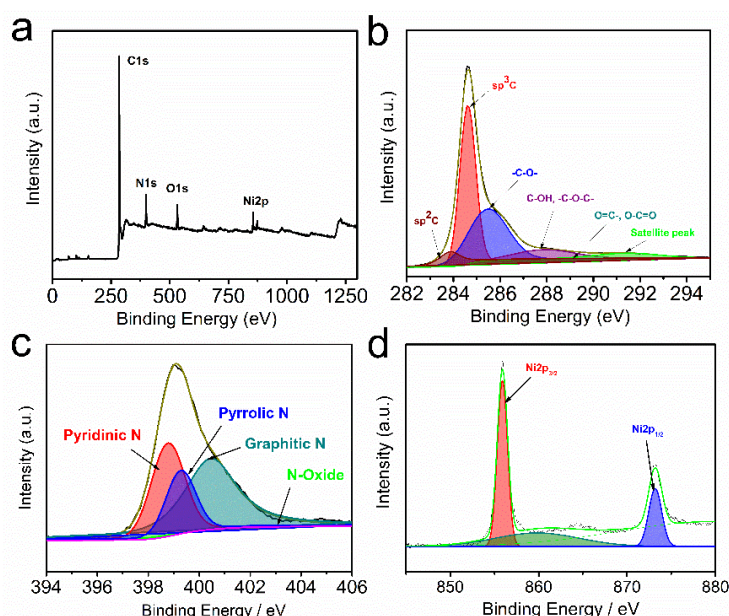


Figure 2.4. XPS survey of G-NP (a), deconvolution peak of Carbon (b), Nitrogen (c) and Nickel (d).

The G-M-T showed a peak at 165 eV that is characteristic of $-C=S-C-$ moieties (Figure 2.3c). These experiments have proven that the DLC-G with various dopants can be synthesized by changing the exfoliator molecules. The XPS spectra of the G-NP (Figure 2.4a) confirmed the presence of presence of sp^2 C (Figure 2.4b), pyridinic nitrogen (38.9%), pyrrolic nitrogen (28.6) and graphitic nitrogen (32.4%) (Figure 2.4c), and Ni2p (Figure 2.4d).

2.3.4 Scanning electron microscope

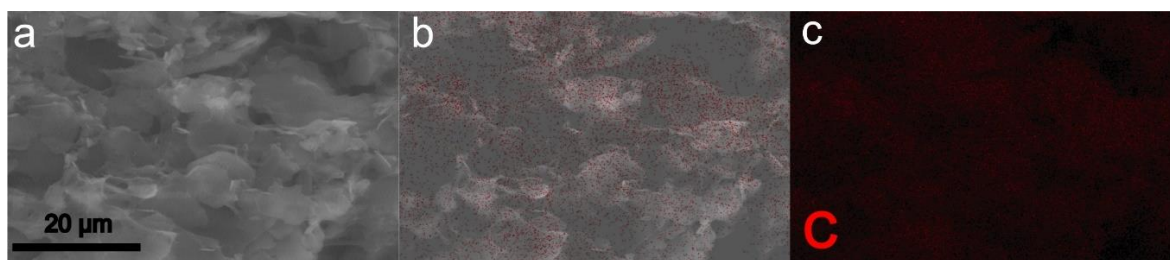


Figure 2.5. SEM imaging of G-A (a), mapping element (Carbon) on the same spot (b) and mapping of element Carbon (c). Scale bar is 20 μm.

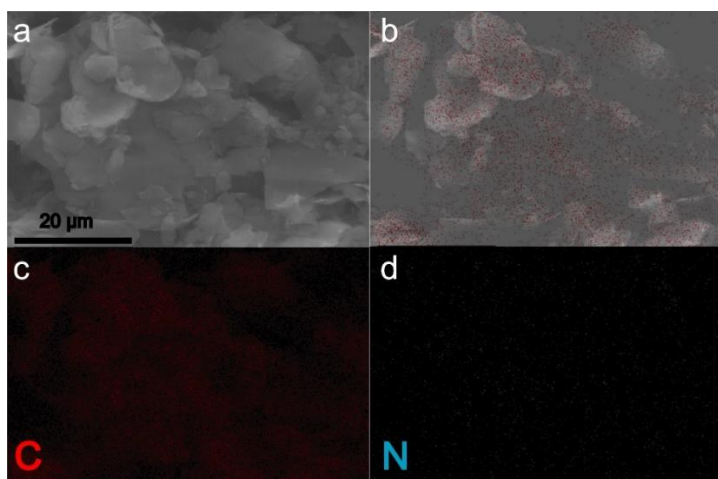


Figure 2.6. SEM imaging of G-M (a), overall mapping elements (Carbon and Nitrogen) on the same spot (b), mapping of corresponding elements C(c) and N(d). Scale bar is 20 μm.

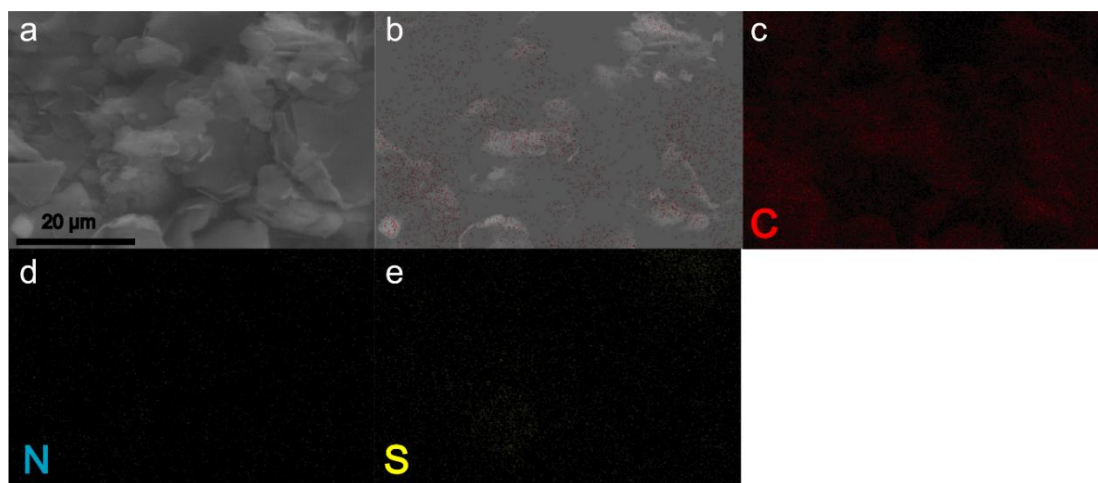


Figure 2.7. SEM imaging of G-M-T (a), overall mapping elements (Carbon, Nitrogen and Sulfur) on the same spot (b), mapping of corresponding elements C(c), N(d), S(e). Scale bar is 20 μm.

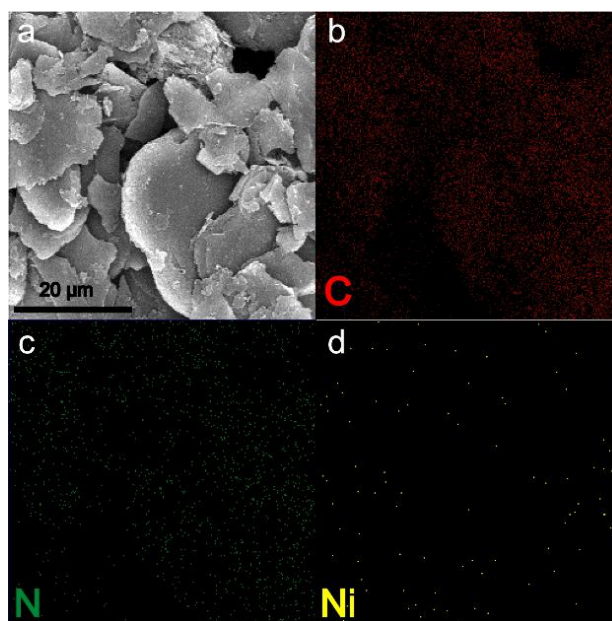


Figure 2.8. SEM imaging of G-NP (a), mapping of corresponding elements C(b), N(c) and Ni(d). Scale bar is 20 μm.

The Scanning electron microscope (SEM) characterization confirmed the morphology of sheet in the exfoliated graphene layer samples and atomic mapping was carried out to corroborate the presence of heteroatoms in the samples. The G-A samples demonstrated the presence of carbon throughout the sample (Figure 2.5).

In case of G-M, carbon and nitrogen were also present and they are distributed uniformly throughout the sample (Figure 2.6). We noticed the presence of sulfur along with C, and N in the samples of G-M-T (Figure 2.7). Further, found the uniform distribution of N and Ni ion throughout the samples (Figure 2.8).

2.3.5 Transmission electron microscope

The TEM images showed a clear difference in morphology between the graphite and graphene. The graphite comprises about 80 layers of graphene (Figure 2.9a). About ten and five layers are found in G-M (Figure 2.9b) and G-M-T (Figure 2.9c), respectively. TEM imaging was carried out for samples blended with sulfur. The sulfur loading did make the graphene opaque (Figure 2.9d). The opaqueness is due to presence of a large amount of sulfur along with DLC-G. We hypothesized that the DLC-G would withhold sulfur better than that of graphite. The TEM image of G-NP showed about five layers of graphene in the samples of G-NP (Figure 2.9e).

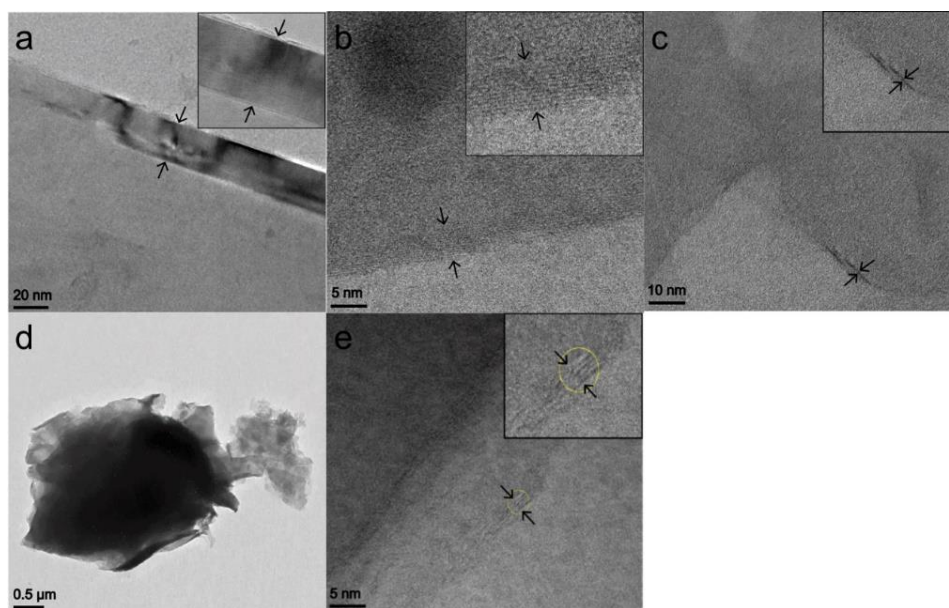


Figure 2.9. TEM image of Pristine Graphite (a) (scale bar is 20 nm), TEM images showing the few layers of graphene G-M (b), G-M-T (c), G-M-T/S (d), and G-NP (e).

2.3.6 Thermogravimetric analysis

To test this hypothesis, the samples were subjected to TGA analysis. The sulfur loading was 85.8% while sulfur was blended with G-A. It increased to 87.2%, and 89.5% for G-M, G-M-T and G-NP respectively (Figure 2.10a). Also, found and 89.4% of Sulfur loading in G-NP (Figure 2.10b).

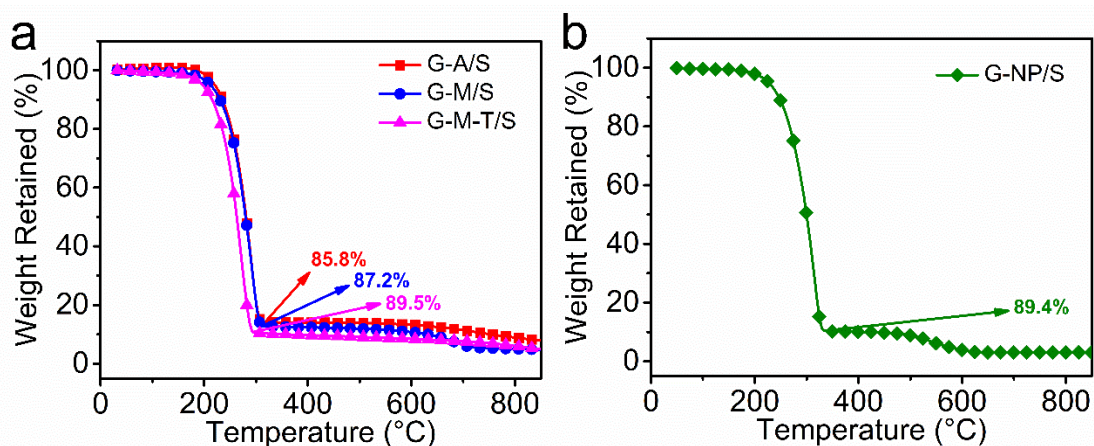


Figure 2.10. TGA indicating the sulfur loading in G-A, G-M and G-M-T, (a) and G-NP (b).

2.3.7 Polysulfide adsorption test

We also carried out polysulfide adsorption experiment to find out the interaction between DLC-G and polysulfides. A 5 mM Li_2S_6 was prepared by following the reported procedure.[58,59] 5 mg of DLC-Gs were dropped into the 5 mM solution of Li_2S_6 . The solutions were left quiescent for 12 hrs. The color of the solution with G-A didn't vary significantly, indicating the

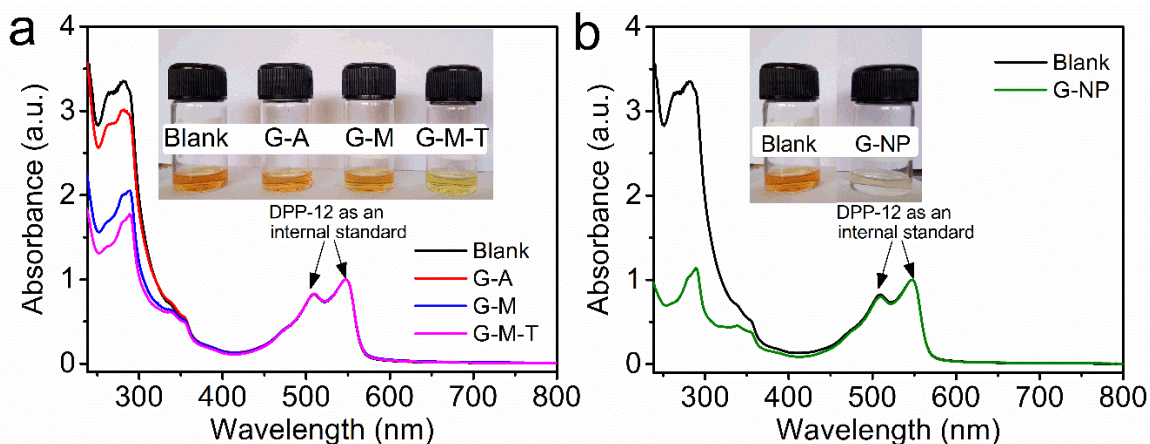


Figure 2.11. UV-Vis spectra of Li_2S_6 solution in absence (Blank) and presence of G-A, G-M, G-M-T (a), and G-NP (b). The insert photographs show the color of Blank Li_2S_6 solution and the supernatant of adsorbed Li_2S_6 on DLC-Gs.

weak interaction between polysulfide and G-A. In case of G-NP, appeared colorless to the naked eyes compared to other DLC-Gs indicating that the polysulfide is adhered to the positive charge bearing G-NP (insert photograph, Figure 2.11a and b).

An aliquot of the polysulfide adsorption test solution of all the samples were taken to record UV-vis absorption spectra. The absorption peaks corresponding to S_6^{2-} showed the lowest absorption among all the DLC-G. In that solution, an internal standard Diketopyrrolopyrrole (DPP) was added. To quantify the interaction, an aliquot was taken to record UV-vis absorption spectra. The Li_2S_6 solution showed three peaks at 263, 281 and 338 nm. The solution with DPP (internal standard) showed two additional peaks at 510 and 547 nm. The UV-vis absorption spectra of the aliquot solution are shown in Figure 2.11a. The absorption maxima (S_6^{2-}) decreased in the following order $\text{G-A} > \text{G-M} > \text{G-M-T}$. This trend indicates that the G-A has weak and G-M-T has strong interaction with polysulfides. In case of G-A, there is no specific interaction between the hydrophobic surface of G-A and negative charge bearing polysulfides. On the other hand, polysulfide interacts with G-M due to Lewis acid base interaction. In case of G-M-T, Lewis acid base interaction and sulfur sulfur interaction is in operation. Due to the strong interaction, polysulfide adhered well on to the surface of G-M-T. The extremely low absorbance has been observed for G-NP (Figure 2.11b). It proves that the excellent polyvalent interaction between the Ni cations of G-NP with that of polysulfides. This experiment corroborates our hypothesis that the few layer graphene with heteroatom increases the interaction between polysulfide and graphene.

2.4 Electrochemical studies

2.4.1 Electrode preparation

The Sulfur composite materials were used for battery application. The slurry for the cathode was prepared using the DLC-Gs, conducting carbon and PVDF are mixed with the mass ratio of 60:30:10. The N-Methyl-2-pyrrolidone (NMP) was used as a solvent. The slurry was coated onto carbon-coated aluminum foil, allowed to dry at room temperature and dried at 60 °C for 16 h.

2.4.2 Li-S cell fabrication

The above-prepared electrode was used as a working electrode, Li foil as counter and reference electrode and Celgard 2325 as separator. 1.0 M LiTFSI in 1,3-dioxolane and 1,2-dimethoxyethane (volume ratio 1:1) and 0.4 M LiNO₃ was used as an electrolyte. The 2032 type coin cells were fabricated in an Argon filled glovebox (MBRAUN, O₂ < 0.1 ppm, H₂O < 0.1 ppm).

2.4.3 Cyclic voltammetry

The cyclic voltammetry was carried out using a multichannel Autolab MAC80038 instrument with the potential range of 1.5 V – 3.0 V vs Li⁺/Li. The first peak appeared at 2.3 V, which corresponds to the conversion of S₈ to Li₂S_n (4 < n ≤ 8).[1] Subsequently, conversion of Li₂S_n to Li₂S₂/Li₂S occurred at 2 V. In the reverse sweep, conversion of Li₂S to S₈ occurred at 2.4 V (Figure 2.12a).[60] These are typical peaks observed in Li-S batteries. It is worth noting the variation in peak current intensity (*i_p*) as a function of cycle number. At the end of the 5th cycle, the *i_p* decreased by 25% while using G-A. The corresponding change was 10% while using G-M as electrode. Based on this trend, we anticipated a lower change while using G-M-T as electrode. Contrary to this expectation, the decrease in peak intensity was 29%, which is the highest among the DLC-G. This indicates that the polysulfide dissolution has increased while the electrodes are prepared with G-M-T. Although the absorption studies (Figure 2.11) indicate strong interaction between G-M-T and polysulfides in quiescent solution, the polysulfide dissolution is not suppressed during potential sweep. The *i_p* was found to be 1.08×10⁻³ mA for G-A, which increased to 1.15×10⁻³ mA for G-M and increased further to 1.87×10⁻³ mA for G-M-T after fifth cycles. The significant increase in *i_p* of sulfur redox in G-M-T based electrodes is an indication of electrocatalysis. The cyclic voltammetry of the batteries fabricated using G-NP, sulfur, binder and conducting carbon showed typical redox peaks expected of sulfur. The decrease in peak current intensity (*i_p*) after five cycles is 5.8% (Figure 2.12b). This *i_p* decrease

is the lowest among all the DLC-Gs studied in this work. The sharp peaks at 2.43 V in the cyclic voltammogram also indicates the electrocatalytic property of G-NP. The electrocatalytic

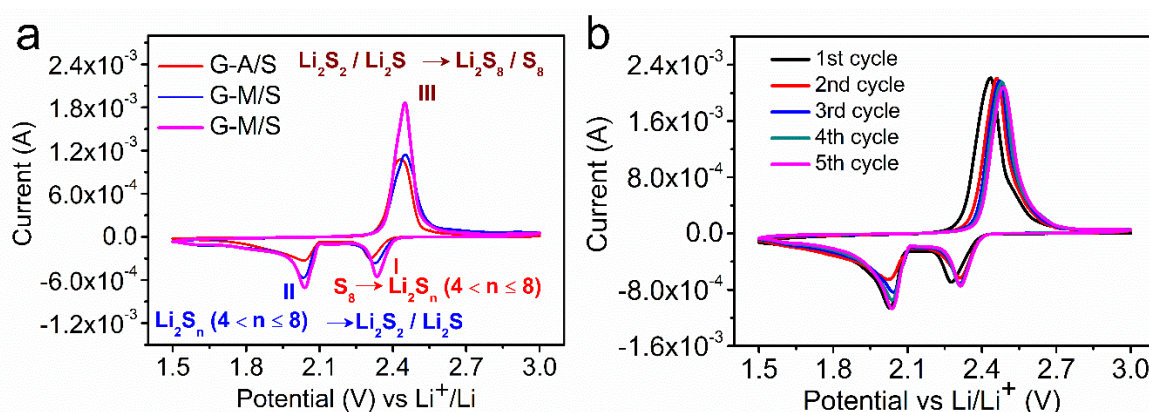


Figure 2.12. Cyclic voltammogram of Li-S battery comprising G-A, G-M, G-M-T (a), and G-NP (b) with scan rate of 0.1 mV s^{-1} .

activity is attributed to the presence of high percentage of pyridinic (38.9%) and graphitic nitrogen (32.4%) (Figure 2.4).

2.4.4 Charge-discharge experiments

The batteries fabricated using DLC-G were subjected to charge-discharge experiments. The experiments were carried out between 1.5 and 3 V vs Li^+/Li . The discharge curve showed two plateaus corresponding to the following reactions, $\text{S}_8 \rightarrow \text{Li}_2\text{S}_n$ ($4 < n \leq 8$), Li_2S_n ($4 < n \leq 8$) \rightarrow $\text{Li}_2\text{S}_2/\text{Li}_2\text{S}$ at 2.3 V and 2.0 V, respectively.[1] The reactions corresponding to various regions of the curve are shown in Figure 2.12. The specific capacity of the first cycle of the battery with G-A was 372 mAh g^{-1} (0.2 h^{-1}) (Figure 2.13a). Please note that the specific capacity is a mere 22% of theoretical capacity (1675 mAh g^{-1}). This decreased to 186 mAh g^{-1} at 100th cycle, decreasing 54% compared to the first cycle. A similar decrease in specific capacity as a function of hundred charge-discharge cycles was observed for other C rates. The reduction in specific capacity compared to the first charge-discharge cycle was 35% (1 h^{-1}), 14% (2 h^{-1}) and 44% (5 h^{-1}). These experiments indicate the poor efficacy of DLC-G devoid of heteroatoms in Li-S batteries. Furthermore, the polarization of the discharge curve means poor electrocatalysis while using G-A as electrode material. In the case of G-M, the specific capacity of the first cycle was 535 mAh g^{-1} (0.2 h^{-1}), which is 163 mAh g^{-1} higher than that of G-A based batteries (Figure 2.13b). We attribute the marginal performance increase to the presence of 24.8% of pyridinic nitrogen in G-M. The decrease in specific capacity as a function of hundred charge-discharge cycling was found to be 42% (311 mAh g^{-1} at 100th cycle). Thus, the performance of N-doped layer comprising graphene (G-M) is better than G-A based batteries. The improved

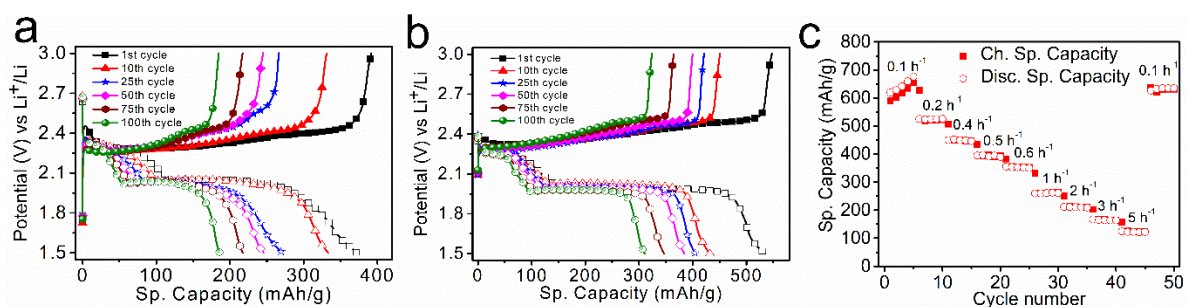


Figure 2.13. Charge-Discharge curves at 0.2 h^{-1} showing specific capacity fading while using G-A (a), G-M (b) in Li-S battery electrode, and Rate performance study of Li-S cell using G-M (c).

performance is attributed to heteroatoms that are present in G-M. At higher C rates, the decrease in specific capacity as function of hundred charge-discharge cycling was found to be 25% (1 h^{-1}), 14% (2 h^{-1}) and 31% (5 h^{-1}). So far, a battery is subjected to charge-discharge cycling at a particular C rate for hundred cycles. To test a battery's efficacy as a function of various C rates, rate performance studies were conducted. In this experiment, a battery was subjected to charge-discharge cycling at 0.1 h^{-1} and the C rate was gradually increased up to 5 h^{-1} . While increasing the C rate, the specific capacity decreases. At 5 h^{-1} , the specific capacity decreased by 82% compared to 0.1 h^{-1} . This result raises the question, is the massive decrease due to sulfide dissolution? To test this, the battery that was discharged at 5 h^{-1} , was subjected to charge-discharge experiment at 0.1 h^{-1} . In this experiment, specific capacity bounced back to 634 mAh g^{-1} , which is very close to the specific capacity observed at the start of the experiment (Figure 2.13c). Please recall the specific capacity at 5 h^{-1} was 124 mAh g^{-1} , which was observed in the previous experiment. Thus, the bounce-back of specific capacity at 0.1 h^{-1} indicates that the polysulfide dissolution is low during charge-discharge experiments, while using G-M.

In the next set of experiments, G-M-T was used to prepare the battery electrodes. The specific capacity of batteries prepared using G-M-T was 1270 mAh g^{-1} , while charge-discharge experiment was carried out at 0.2 h^{-1} (Figure 2.14a). This value is 898 mAh g^{-1} higher than the control experiment (G-A based batteries). The impressive performance enhancement is attributed to the presence of 40.9% pyridinic nitrogen. The decrease in specific capacity as a function of hundred charge-discharge cycling was found to be 39%. This data indicate the improvement in battery performance imparted by doping the carbon layer with N and S. The rate performance study was conducted by following the procedure adapted for G-M based batteries. At 0.1 h^{-1} , the specific capacity was found to be 1426 mAh g^{-1} . Upon increase in C rate, the specific capacity decreased. The lowest specific capacity of 513 mAh g^{-1} was found at 5 h^{-1} . The decrease is 64%. After the charge-discharge experiments at 5 h^{-1} , the batteries

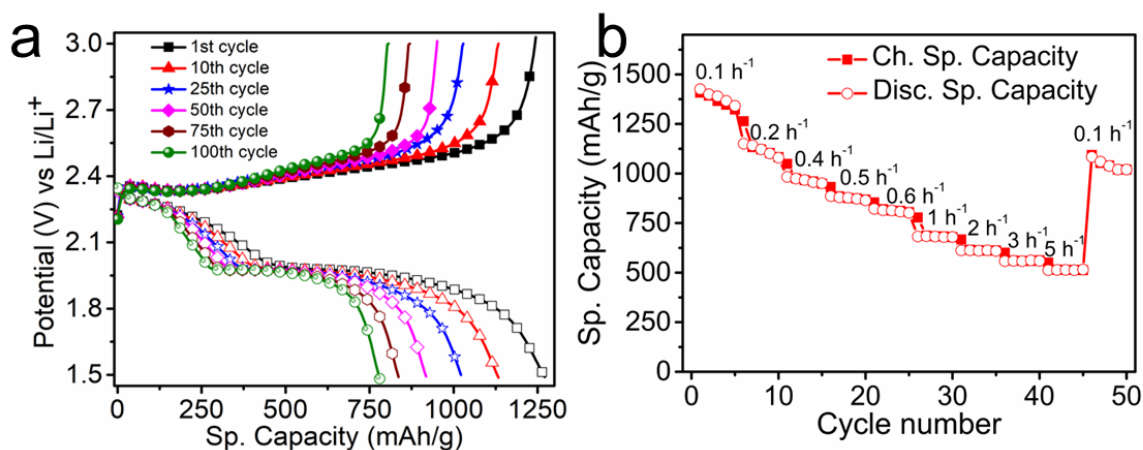


Figure 2.14. Charge-discharge profile at 0.2 h^{-1} rate (a), and Rate performance study (b) of Li-S cell comprising G-M-T.

were cycled at 0.1 h^{-1} . The specific capacity was found to be 1083 mAh g^{-1} (Figure 2.14b). This is 75% of the specific capacity observed at the same C rate (0.1 h^{-1}) during the start of the experiment. Thus, the battery didn't recover fully probably due to polysulfide dissolution. Thus, the polysulfide dissolution is higher in case of G-M-T based batteries compared to G-M based batteries. This correlates well with the observation of decrease in peak current intensity in cyclic voltammograms of G-M-T based batteries (Figure 2.12a).

In the charge-discharge experiment using G-NP comprised Li-S cells, the specific capacity at the first cycle was 1345 mAh g^{-1} (0.2 h^{-1}). This specific capacity is 80% of theoretical maximum (Figure 2.15a). At the 100th cycle, the specific capacity decreased to 1084 mAh g^{-1} . The decrease is mere 20%. Unlike other DLC-G, the specific capacity of the first cycle remained above 1000 mAh g^{-1} at C rates of 0.2 h^{-1} (1218 mAh g^{-1}). Furthermore, the decrease in specific capacity as a function of hundred charge-discharge cycles varied as follows, 13% (0.5 h^{-1}), 21% (1 h^{-1}), 20% (2 h^{-1}), 7% (5 h^{-1}). The lowest specific capacity of 815 mAh g^{-1} was found for batteries cycled at 5 h^{-1} . This impressive performance is due to polyvalent attraction between Ni ions on the layer of graphene with polysulfide. Please note that the discharge curves don't show any polarization due to electrocatalysis and suppressed dissolution of polysulfide. To further test the efficacy of batteries comprising G-NP, rate performance experiments were conducted. The specific capacity was 1279 mAh g^{-1} (0.1 h^{-1}) at the start of the experiment, which decreased to 324 mAh g^{-1} (5 h^{-1}). Immediately after cycling at 5 h^{-1} , the experiment was conducted at 0.1 h^{-1} . In this experiment, the specific capacity bounced back to 1214 mAh g^{-1} (Figure 2.15b). The loss of specific capacity is a mere 6% while going from 0.1 h^{-1} to 0.1 h^{-1} through 0.2 h^{-1} , 0.4 h^{-1} , 0.5 h^{-1} , 0.6 h^{-1} , 1 h^{-1} , 2 h^{-1} , 3 h^{-1} and 5 h^{-1} . The data corroborates our

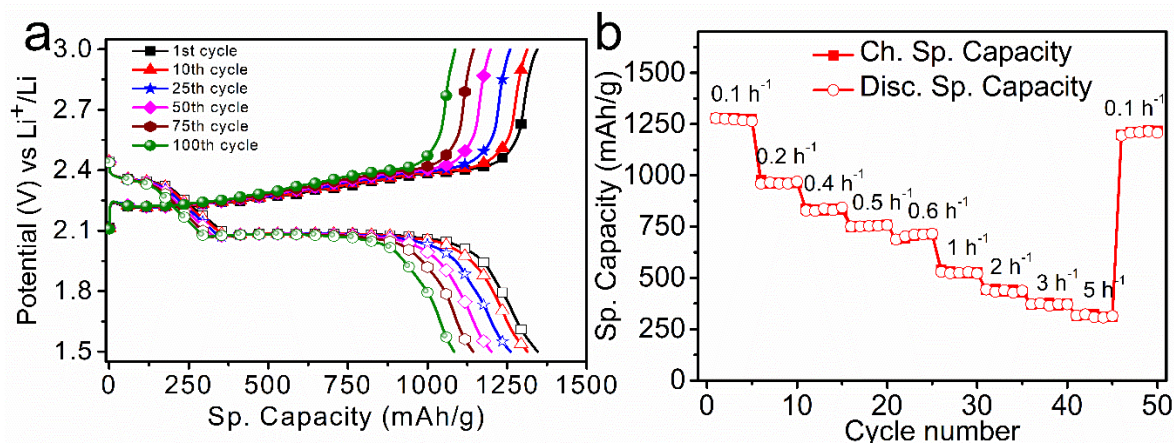


Figure 2.15. Charge-discharge profile at 0.2 h⁻¹ (a), and rate performance of Li-S cell comprising G-NP (b).

hypothesis that the Ni ions on the layer of graphene withhold the polysulfide during the charge-discharge cycling experiments.

To further study the cyclic stability of G-NP based batteries, they were subjected to five hundred charge-discharge cycles. The G-NP based batteries' specific capacity decreased by 39% and the exact value of specific capacity was 748 mAh g⁻¹ (Figure 2.16a). Contrary to this, G-M-T based batteries exhibited initial specific capacity comparable to that of G-NP based batteries. However, at the end of five hundred charge-discharge cycles, the absolute specific capacity was 156 mAh g⁻¹, which is 4.7 times lower than that observed for G-NP based batteries. The decrease is a massive 88% for G-M-T based batteries. In the case of G-M and G-A based batteries, the initial specific capacity was low. Their specific capacity fading over 500 charge-discharge cycling is also comparable. G-M batteries show a slightly better performance than the G-A based batteries. The performance enhancement in case of G-M-T based batteries at the beginning of charge discharge experiment is impressive. But the fading in specific capacity as a function of cycle number is very high. Thus, the overall battery performance of G-M-T batteries is moderate. However, the overall performance of G-NP based batteries is very impressive. From the available data, we computed Ragone plot by calculating specific power and energy. The G-A and G-M based batteries showed very high specific power but exhibited poor specific energy. Contrary to this, the G-M-T and G-NP based batteries exhibited high specific energy. Specific energy equals the multiplication of cell voltage and amount of charge stored. The cell voltage is very close for all the batteries. However, the amount of charge stored is high for G-M-T and G-NP. Therefore, the batteries based on G-M-T and G-NP also showed high specific energy (Figure 2.16b). In addition, the batteries with G-

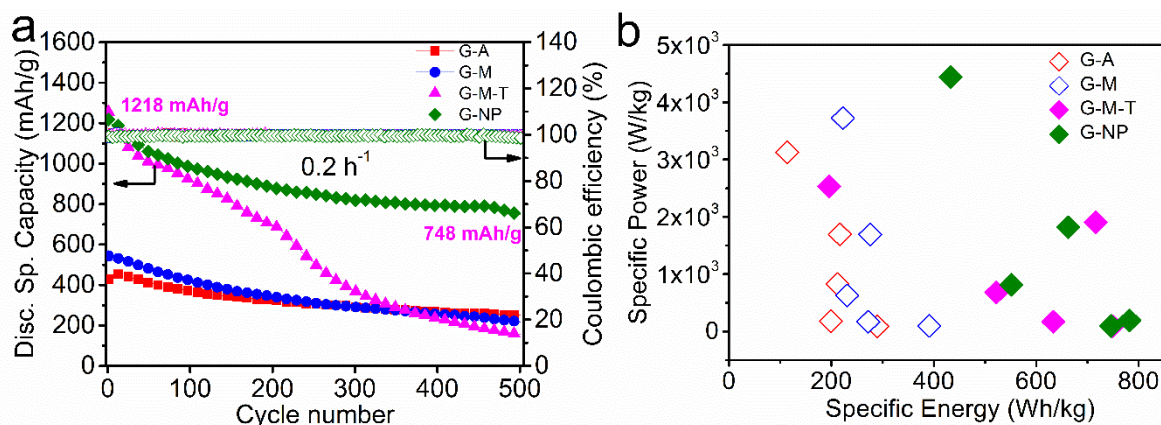


Figure 2.16. Plot showing variation in specific capacity for 500 cycles 0.2 h^{-1} (a), and Ragone plot of Li-S batteries with various DLC-Gs (b).

NP exhibited high specific power (4437 W kg^{-1}) and the specific energy is 782 Wh kg^{-1} (Figure 2.16b).

2.4.5 Symmetric cell assembly and Tests

In order to study the electrocatalysis of DLC-G, symmetric cells were fabricated. The working and counter electrodes comprise DLC-G, conducting carbon and binder. The electrolyte comprises Li_2S_6 . A $0.2 \text{ M Li}_2\text{S}_6$ solution was prepared by dissolving elemental sulfur and Li_2S (5:1 molar ratio) in a mixture of DOL and DME (volume ratio of 1:1) under vigorous stirring at $50 \text{ }^\circ\text{C}$. The symmetrical cells were fabricated using identical DLC-Gs. The cells were assembled inside an Argon filled glovebox and cyclicvoltammograms (CVs) were recorded between -1 and $+1 \text{ V}$ at a scan rate of 5 mV/s .

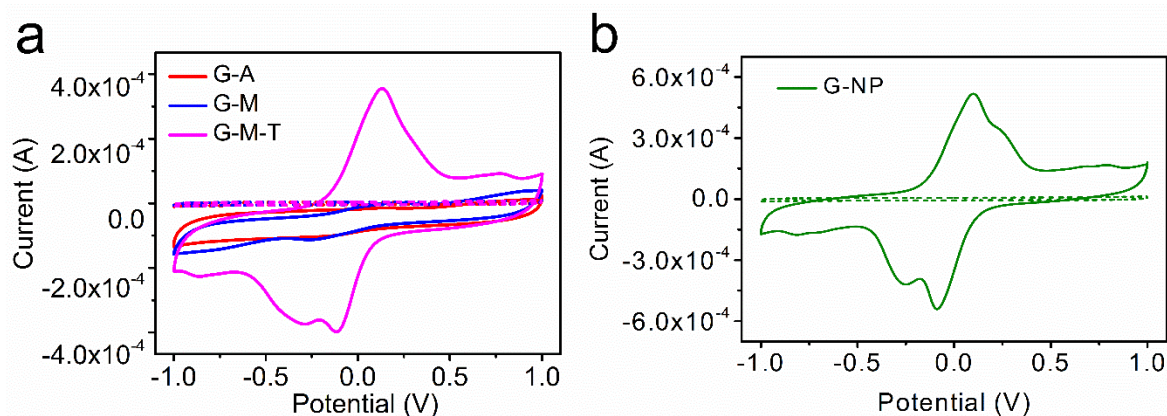


Figure 2.17. Cyclicvoltammograms of symmetric cells comprising G-A, G-M, G-M-T (a), and G-NP (b). The dashed plots are the experiments carried out without Li_2S_6 .

The CV of G-A showed extremely weak oxidation (0.11 V) and reduction (-0.11 V) wave. G-M also showed oxidation and reduction waves at 0.24 V and -0.24 V , respectively (Figure 2.17a). This indicate poor electrocatalysis by these two DLC-G(s). Indeed, the CV of

Table 2.2. Li-S battery metrics of various materials

Materials	Percentage of Sulfur (wt %)	Methodology	Performance	Ref
DLC-G with Ni cations and N/S	89.4	Mechanical exfoliation	1218 mAh/g at 0.2 C and 748 mAh/g after 500 cycles	This work
Vertical graphene on TiC nanofiber/S	85.7	Chemical vapour deposition	971 mAh/g at 2 C, 600 mAh/g at 0.5 C after 800 cycles	[8]
S@CoP/rGO	50-90	Hydrothermal method and Gas-Solid reaction	504 mAh/g after 1200 cycles	[61]
3D Nitrogen-doped Graphene/S	87.6	One-pot solvothermal process	792 mAh/g after 145 cycles at 600 mA/g and 671 mAh/g after 200 cycles at 1500 mA/g	[62]
MOF-derived Co ₉ S ₈ on Graphene foam	86.9	Chemical vapour deposition	736 mAh/g after 500 cycles at 1 C	[59]
Nitrogen-doped tubular/porous carbon channels on Graphene	62	Double-template method	563 mAh/g after 600 cycles at 6 C	[51]
N-doped porous carbon layers/Graphene	60	Hydrothermal process	625 mAh/g at 2 C and remains at 461 mAh/g after 200 cycles	[50]
Boron-doped Graphene Aerogel	59	One-pot hydrothermal method	994 mAh/g at 0.2 C after 100 cycles	[36]
rGO: poly(anthraquinonyl sulfide):Nano Sulfur	48	Vacuum filtration	1255 mAh/g at 0.5 C and decay rate of 0.0046% per cycles over 1200 cycles	[34]

symmetric cells without Li₂S₆ (dashed lines) in the electrolyte didn't show oxidation and reduction waves (Figure 2.17a). Thus, the oxidation and reduction waves in the CV of G-A and G-M based symmetric cells originate from Li₂S₆. The CV of G-M-T showed a sharp oxidation

peak at 0.12 V. This peak corresponds to the conversion of lithium sulfide to lithium polysulfide and sulfur. Two peaks were observed during the reverse scan at -0.12 V and -0.29 V. The peak at -0.12 V corresponds to the conversion of Li_2S_6 to short chain lithium polysulfide. The peak at -0.29 V corresponds to the formation of lithium sulfide.[63]

In case G-NP based symmetric cells, two well defined oxidation and reduction peaks were observed. The first oxidation peak centered at 0.09 V, indicates the oxidation of Li_2S to Li_2S_6 and the second oxidation peak at 0.25 V is due to the conversion of Li_2S_6 to sulfur. The two reduction peaks observed at -0.09V and -0.25V are due to conversion of sulfur to Li_2S_6 and Li_2S_6 to Li_2S (Figure 2.17b).[63-66]

2.5 Conclusion

In conclusion, we have developed an approach to prepare graphene with few layers by employing a mechanical exfoliation process. The process utilizes exfoliators during the exfoliation of graphene from the pristine graphite. By judicious choice of exfoliator, DLC-G with nitrogen and DLC-G with nitrogen and sulfur are prepared. The battery with DLC-G comprising nitrogen and sulfur showed improved specific capacity compared to battery comprising DLC-G with nitrogen alone. However, the polysulfide dissolution is not suppressed. The DLC-G with Ni cations and nitrogen showed impressive specific capacity, power, and energy density. This has been attributed to electrocatalysis facilitated by high percentage of pyridinic nitrogen. The suppression of sulfur dissolution is attributed to electrostatic polyvalent attraction between Ni cations and polysulfide.

2.6 References

- [1] Bruce, P. G.; Freunberger, S. A.; Hardwick, L. J.; Tarascon, J.-M. Li–O₂ and Li–S batteries with high energy storage. *Nat. Mater.* **2012**, *11*, 19-29.
- [2] Manthiram, A.; Chung, S.-H.; Zu, C. Lithium–Sulfur Batteries: Progress and Prospects. *Adv. Mater.* **2015**, *27*, 1980-2006.
- [3] Manthiram, A.; Fu, Y.; Chung, S.-H.; Zu, C.; Su, Y.-S. Rechargeable Lithium–Sulfur Batteries. *Chem. Rev.* **2014**, *114*, 11751-11787.
- [4] Yin, Y.-X.; Xin, S.; Guo, Y.-G.; Wan, L.-J. Lithium–Sulfur Batteries: Electrochemistry, Materials, and Prospects. *Angew. Chem. Int. Ed.* **2013**, *52*, 13186-13200.
- [5] Kim, J.; Lee, D.-J.; Jung, H.-G.; Sun, Y.-K.; Hassoun, J.; Scrosati, B. An Advanced Lithium-Sulfur Battery. *Adv. Funct. Mater.* **2013**, *23*, 1076-1080.
- [6] Rosenman, A.; Markevich, E.; Salitra, G.; Aurbach, D.; Garsuch, A.; Chesneau, F. F. Review on Li-Sulfur Battery Systems: an Integral Perspective. *Adv. Energy Mater.* **2015**, *5*, 1500212.
- [7] Cerdas, F.; Titscher, P.; Bogner, N.; Schmuck, R.; Winter, M.; Kwade, A.; Herrmann, C. Exploring the Effect of Increased Energy Density on the Environmental Impacts of Traction Batteries: A Comparison of Energy Optimized Lithium-Ion and Lithium-Sulfur Batteries for Mobility Applications. *Energies* **2018**, *11*, 150.

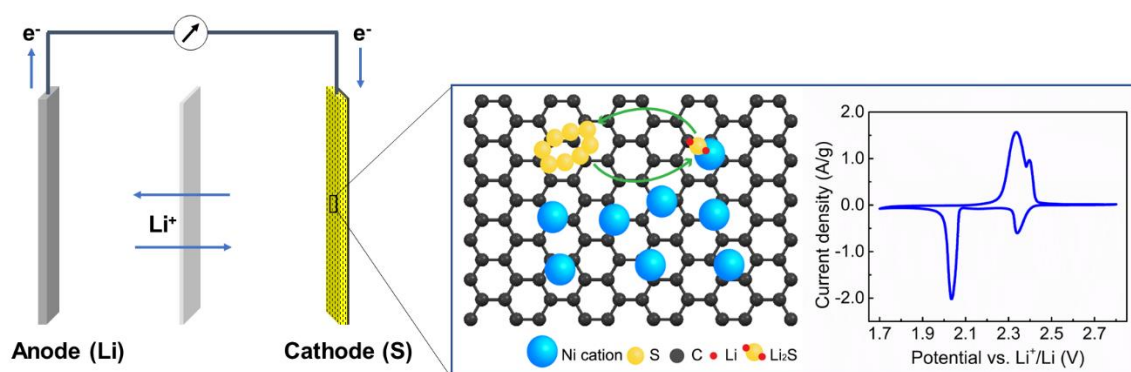
- [8] Zhang, Y.; Zhang, P.; Zhang, S.; Wang, Z.; Li, N.; Silva, S. R. P.; Shao, G. A flexible metallic TiC nanofiber/vertical graphene 1D/2D heterostructured as active electrocatalyst for advanced Li–S batteries. *InfoMat.* **2021**, *3*, 790-803.
- [9] Zhang, C.; Cui, L.; Abdolhosseinzadeh, S.; Heier, J. Two-dimensional MXenes for lithium-sulfur batteries. *InfoMat.* **2020**, *2*, 613-638.
- [10] Yao, Y.-X.; Zhang, X.-Q.; Li, B.-Q.; Yan, C.; Chen, P.-Y.; Huang, J.-Q.; Zhang, Q. A compact inorganic layer for robust anode protection in lithium-sulfur batteries. *InfoMat.* **2020**, *2*, 379-388.
- [11] Wei, Z.; Ren, Y.; Sokolowski, J.; Zhu, X.; Wu, G. Mechanistic understanding of the role separators playing in advanced lithium-sulfur batteries. *InfoMat.* **2020**, *2*, 483-508.
- [12] Liang, C.; Dudney, N. J.; Howe, J. Y. Hierarchically Structured Sulfur/Carbon Nanocomposite Material for High-Energy Lithium Battery. *Chem. Mater.* **2009**, *21*, 4724-4730.
- [13] Zhang, S. S. Liquid electrolyte lithium/sulfur battery: Fundamental chemistry, problems, and solutions. *J. Power Sources* **2013**, *231*, 153-162.
- [14] Liang, J.; Sun, Z.-H.; Li, F.; Cheng, H.-M. Carbon materials for Li–S batteries: Functional evolution and performance improvement. *Energy Storage Mater.* **2016**, *2*, 76-106.
- [15] Jeong, S.; Bresser, D.; Buchholz, D.; Winter, M.; Passerini, S. Carbon coated lithium sulfide particles for lithium battery cathodes. *J. Power Sources* **2013**, *235*, 220-225.
- [16] Schuster, J.; He, G.; Mandlmeier, B.; Yim, T.; Lee, K. T.; Bein, T.; Nazar, L. F. Spherical Ordered Mesoporous Carbon Nanoparticles with High Porosity for Lithium–Sulfur Batteries. *Angew. Chem. Int. Ed.* **2012**, *51*, 3591-3595.
- [17] Ji, X.; Lee, K. T.; Nazar, L. F. A highly ordered nanostructured carbon–sulphur cathode for lithium–sulphur batteries. *Nat. Mater.* **2009**, *8*, 500-506.
- [18] Manthiram, A.; Fu, Y.; Su, Y.-S. Challenges and Prospects of Lithium–Sulfur Batteries. *Acc. Chem. Res.* **2013**, *46*, 1125-1134.
- [19] Li, M.; Frerichs, J. E.; Kolek, M.; Sun, W.; Zhou, D.; Huang, C. J.; Hwang, B. J.; Hansen, M. R.; Winter, M.; Bieker, P. Solid-State Lithium–Sulfur Battery Enabled by Thio-LiSICON/Polymer Composite Electrolyte and Sulfurized Polyacrylonitrile Cathode. *Adv. Funct. Mater.* **2020**, *30*, 1910123.
- [20] Mikhaylik, Y. V.; Akridge, J. R. Polysulfide Shuttle Study in the Li/S Battery System. *J. Electrochem. Soc.* **2004**, *151*, A1969.
- [21] Chung, S.-H.; Manthiram, A. A Polyethylene Glycol-Supported Microporous Carbon Coating as a Polysulfide Trap for Utilizing Pure Sulfur Cathodes in Lithium–Sulfur Batteries. *Adv. Mater.* **2014**, *26*, 7352-7357.
- [22] Yao, H.; Yan, K.; Li, W.; Zheng, G.; Kong, D.; Seh, Z. W.; Narasimhan, V. K.; Liang, Z.; Cui, Y. Improved lithium–sulfur batteries with a conductive coating on the separator to prevent the accumulation of inactive S-related species at the cathode–separator interface. *Energy Environ. Sci.* **2014**, *7*, 3381-3390.
- [23] Kim, H. M.; Sun, H.-H.; Belharouak, I.; Manthiram, A.; Sun, Y.-K. An Alternative Approach to Enhance the Performance of High Sulfur-Loading Electrodes for Li–S Batteries. *ACS Energy Lett.* **2016**, *1*, 136-141.
- [24] Zhang, B.; Qin, X.; Li, G. R.; Gao, X. P. Enhancement of long stability of sulfur cathode by encapsulating sulfur into micropores of carbon spheres. *Energy Environ. Sci.* **2010**, *3*, 1531-1537.
- [25] Jayaprakash, N.; Shen, J.; Moganty, S. S.; Corona, A.; Archer, L. A. Porous Hollow Carbon@Sulfur Composites for High-Power Lithium–Sulfur Batteries. *Angew. Chem. Int. Ed.* **2011**, *50*, 5904-5908.
- [26] Liang, X.; Hart, C.; Pang, Q.; Garsuch, A.; Weiss, T.; Nazar, L. F. A highly efficient polysulfide mediator for lithium–sulfur batteries. *Nat. Commun.* **2015**, *6*, 5682.
- [27] Tsao, Y.; Chen, Z.; Rondeau-Gagné, S.; Zhang, Q.; Yao, H.; Chen, S.; Zhou, G.; Zu, C.; Cui, Y.; Bao, Z. Enhanced Cycling Stability of Sulfur Electrodes through Effective Binding of Pyridine-Functionalized Polymer. *ACS Energy Lett.* **2017**, *2*, 2454-2462.
- [28] Yang, Y.; Yu, G.; Cha, J. J.; Wu, H.; Vosgueritchian, M.; Yao, Y.; Bao, Z.; Cui, Y. Improving the Performance of Lithium–Sulfur Batteries by Conductive Polymer Coating. *ACS Nano* **2011**, *5*, 9187-9193.
- [29] Wu, Z.; Wang, W.; Wang, Y.; Chen, C.; Li, K.; Zhao, G.; Sun, C.; Chen, W.; Ni, L.; Diao, G. Three-dimensional graphene hollow spheres with high sulfur loading for high-performance lithium-sulfur batteries. *Electrochim. Acta* **2017**, *224*, 527-533.

- [30] Zheng, G.; Zhang, Q.; Cha, J. J.; Yang, Y.; Li, W.; Seh, Z. W.; Cui, Y. Amphiphilic Surface Modification of Hollow Carbon Nanofibers for Improved Cycle Life of Lithium Sulfur Batteries. *Nano Lett.* **2013**, *13*, 1265-1270.
- [31] Wang, H.; Yang, Y.; Liang, Y.; Robinson, J. T.; Li, Y.; Jackson, A.; Cui, Y.; Dai, H. Graphene-Wrapped Sulfur Particles as a Rechargeable Lithium–Sulfur Battery Cathode Material with High Capacity and Cycling Stability. *Nano Lett.* **2011**, *11*, 2644-2647.
- [32] Zu, C.; Manthiram, A. Hydroxylated Graphene–Sulfur Nanocomposites for High-Rate Lithium–Sulfur Batteries. *Adv. Energy Mater.* **2013**, *3*, 1008-1012.
- [33] Lee, J. S.; Manthiram, A. Hydroxylated N-doped carbon nanotube-sulfur composites as cathodes for high-performance lithium-sulfur batteries. *J. Power Sources* **2017**, *343*, 54-59.
- [34] Chen, H.; Wang, C.; Dai, Y.; Qiu, S.; Yang, J.; Lu, W.; Chen, L. Rational Design of Cathode Structure for High Rate Performance Lithium–Sulfur Batteries. *Nano Lett.* **2015**, *15*, 5443-5448.
- [35] Shi, P.; Wang, Y.; Liang, X.; Sun, Y.; Cheng, S.; Chen, C.; Xiang, H. Simultaneously Exfoliated Boron-Doped Graphene Sheets To Encapsulate Sulfur for Applications in Lithium–Sulfur Batteries. *ACS Sustainable Chem. Eng.* **2018**, *6*, 9661-9670.
- [36] Xie, Y.; Meng, Z.; Cai, T.; Han, W.-Q. Effect of Boron-Doping on the Graphene Aerogel Used as Cathode for the Lithium–Sulfur Battery. *ACS Appl. Mater. Interfaces* **2015**, *7*, 25202-25210.
- [37] Liu, D.; Zhang, C.; Zhou, G.; Lv, W.; Ling, G.; Zhi, L.; Yang, Q.-H. Catalytic Effects in Lithium–Sulfur Batteries: Promoted Sulfur Transformation and Reduced Shuttle Effect. *Adv. Sci.* **2018**, *5*, 1700270.
- [38] Gomez-Martin, A.; Martinez-Fernandez, J.; Rutttert, M.; Winter, M.; Placke, T.; Ramirez-Rico, J. An electrochemical evaluation of nitrogen-doped carbons as anodes for lithium ion batteries. *Carbon* **2020**, *164*, 261-271.
- [39] Zhu, P.; Song, J.; Lv, D.; Wang, D.; Jaye, C.; Fischer, D. A.; Wu, T.; Chen, Y. Mechanism of Enhanced Carbon Cathode Performance by Nitrogen Doping in Lithium–Sulfur Battery: An X-ray Absorption Spectroscopic Study. *J. Phys. Chem. C* **2014**, *118*, 7765-7771.
- [40] Pei, F.; An, T.; Zang, J.; Zhao, X.; Fang, X.; Zheng, M.; Dong, Q.; Zheng, N. From Hollow Carbon Spheres to N-Doped Hollow Porous Carbon Bowls: Rational Design of Hollow Carbon Host for Li-S Batteries. *Adv. Energy Mater.* **2016**, *6*, 1502539.
- [41] León, V.; Quintana, M.; Herrero, M. A.; Fierro, J. L. G.; Hoz, A. d. I.; Prato, M.; Vázquez, E. Few-layer graphenes from ball-milling of graphite with melamine. *Chem. Commun.* **2011**, *47*, 10936-10938.
- [42] León, V.; Rodríguez, A. M.; Prieto, P.; Prato, M.; Vázquez, E. Exfoliation of Graphite with Triazine Derivatives under Ball-Milling Conditions: Preparation of Few-Layer Graphene via Selective Noncovalent Interactions. *ACS Nano* **2014**, *8*, 563-571.
- [43] Teng, C.; Xie, D.; Wang, J.; Yang, Z.; Ren, G.; Zhu, Y. Ultrahigh Conductive Graphene Paper Based on Ball-Milling Exfoliated Graphene. *Adv. Funct. Mater.* **2017**, *27*, 1700240.
- [44] Dong, Y.; Zhang, S.; Du, X.; Hong, S.; Zhao, S.; Chen, Y.; Chen, X.; Song, H. Boosting the Electrical Double-Layer Capacitance of Graphene by Self-Doped Defects through Ball-Milling. *Adv. Funct. Mater.* **2019**, *29*, 1901127.
- [45] Pang, Q.; Nazar, L. F. Long-Life and High-Areal-Capacity Li–S Batteries Enabled by a Light-Weight Polar Host with Intrinsic Polysulfide Adsorption. *ACS Nano* **2016**, *10*, 4111-4118.
- [46] Zhou, G.; Paek, E.; Hwang, G. S.; Manthiram, A. Long-life Li/polysulphide batteries with high sulphur loading enabled by lightweight three-dimensional nitrogen/sulphur-codoped graphene sponge. *Nat. Commun.* **2015**, *6*, 7760.
- [47] Balach, J.; Singh, H. K.; Gomoll, S.; Jaumann, T.; Klose, M.; Oswald, S.; Richter, M.; Eckert, J.; Giebeler, L. Synergistically Enhanced Polysulfide Chemisorption Using a Flexible Hybrid Separator with N and S Dual-Doped Mesoporous Carbon Coating for Advanced Lithium–Sulfur Batteries. *ACS Appl. Mater. Interfaces* **2016**, *8*, 14586-14595.
- [48] Zhou, X. Y.; Liao, Q. C.; Bai, T.; Yang, J. Rational design of graphene @ nitrogen and phosphorous dual-doped porous carbon sandwich-type layer for advanced lithium-sulfur batteries. *J. Mater. Sci.* **2017**, *52*, 7719-7732.
- [49] Kong, L.; Li, B.-Q.; Peng, H.-J.; Zhang, R.; Xie, J.; Huang, J.-Q.; Zhang, Q. Porphyrin-Derived Graphene-Based Nanosheets Enabling Strong Polysulfide Chemisorption and Rapid Kinetics in Lithium–Sulfur Batteries. *Adv. Energy Mater.* **2018**, *8*, 1800849.

- [50] Niu, S.; Lv, W.; Zhang, C.; Li, F.; Tang, L.; He, Y.; Li, B.; Yang, Q.-H.; Kang, F. A carbon sandwich electrode with graphene filling coated by N-doped porous carbon layers for lithium–sulfur batteries. *J. Mater. Chem. A* **2015**, *3*, 20218-20224.
- [51] Zhang, M.; Yu, C.; Yang, J.; Zhao, C.; Ling, Z.; Qiu, J. Nitrogen-doped tubular/porous carbon channels implanted on graphene frameworks for multiple confinement of sulfur and polysulfides. *J. Mater. Chem. A* **2017**, *5*, 10380-10386.
- [52] Shi, J.-L.; Tang, C.; Huang, J.-Q.; Zhu, W.; Zhang, Q. Effective exposure of nitrogen heteroatoms in 3D porous graphene framework for oxygen reduction reaction and lithium–sulfur batteries. *J. Energy Chem.* **2018**, *27*, 167-175.
- [53] Koshy, D. M.; Chen, S.; Lee, D. U.; Stevens, M. B.; Abdellah, A. M.; Dull, S. M.; Chen, G.; Nordlund, D.; Gallo, A.; Hahn, C.; Higgins, D. C.; Bao, Z.; Jaramillo, T. F. Understanding the Origin of Highly Selective CO₂ Electroreduction to CO on Ni,N-doped Carbon Catalysts. *Angew. Chem. Int. Ed.* **2020**, *59*, 4043-4050.
- [54] Eckmann, A.; Felten, A.; Mishchenko, A.; Britnell, L.; Krupke, R.; Novoselov, K. S.; Casiraghi, C. Probing the Nature of Defects in Graphene by Raman Spectroscopy. *Nano Lett.* **2012**, *12*, 3925-3930.
- [55] George, G.; Sisupal, S. B.; Tomy, T.; Pottammal, B. A.; Kumaran, A.; Suvekbala, V.; Gopimohan, R.; Sivaram, S.; Ragupathy, L. Thermally conductive thin films derived from defect free graphene-natural rubber latex nanocomposite: Preparation and properties. *Carbon* **2017**, *119*, 527-534.
- [56] George, G.; Sisupal, S. B.; Tomy, T.; Kumaran, A.; Vadivelu, P.; Suvekbala, V.; Sivaram, S.; Ragupathy, L. Facile, environmentally benign and scalable approach to produce pristine few layers graphene suitable for preparing biocompatible polymer nanocomposites. *Sci. Rep.* **2018**, *8*, 11228.
- [57] Blume, R.; Rosenthal, D.; Tessonnier, J.-P.; Li, H.; Knop-Gericke, A.; Schlögl, R. Characterizing Graphitic Carbon with X-ray Photoelectron Spectroscopy: A Step-by-Step Approach. *ChemCatChem* **2015**, *7*, 2871-2881.
- [58] Li, W.; Qian, J.; Zhao, T.; Ye, Y.; Xing, Y.; Huang, Y.; Wei, L.; Zhang, N.; Chen, N.; Li, L.; Wu, F.; Chen, R. Boosting High-Rate Li–S Batteries by an MOF-Derived Catalytic Electrode with a Layer-by-Layer Structure. *Adv. Sci.* **2019**, *6*, 1802362.
- [59] He, J.; Chen, Y.; Manthiram, A. MOF-derived Cobalt Sulfide Grown on 3D Graphene Foam as an Efficient Sulfur Host for Long-Life Lithium-Sulfur Batteries. *iScience* **2018**, *4*, 36-43.
- [60] Tian, D.; Song, X.; Wang, M.; Wu, X.; Qiu, Y.; Guan, B.; Xu, X.; Fan, L.; Zhang, N.; Sun, K. MoN Supported on Graphene as a Bifunctional Interlayer for Advanced Li-S Batteries. *Adv. Energy Mater.* **2019**, *9*, 1901940.
- [61] Zhou, J.; Liu, X.; Zhu, L.; Zhou, J.; Guan, Y.; Chen, L.; Niu, S.; Cai, J.; Sun, D.; Zhu, Y.; Du, J.; Wang, G.; Qian, Y. Deciphering the Modulation Essence of p Bands in Co-Based Compounds on Li-S Chemistry. *Joule* **2018**, *2*, 2681-2693.
- [62] Wang, C.; Su, K.; Wan, W.; Guo, H.; Zhou, H.; Chen, J.; Zhang, X.; Huang, Y. High sulfur loading composite wrapped by 3D nitrogen-doped graphene as a cathode material for lithium–sulfur batteries. *J. Mater. Chem. A* **2014**, *2*, 5018-5023.
- [63] Zhang, L.; Liu, D.; Muhammad, Z.; Wan, F.; Xie, W.; Wang, Y.; Song, L.; Niu, Z.; Chen, J. Single Nickel Atoms on Nitrogen-Doped Graphene Enabling Enhanced Kinetics of Lithium–Sulfur Batteries. *Adv. Mater.* **2019**, *31*, 1903955.
- [64] Wang, R.; Luo, C.; Wang, T.; Zhou, G.; Deng, Y.; He, Y.; Zhang, Q.; Kang, F.; Lv, W.; Yang, Q.-H. Bidirectional Catalysts for Liquid–Solid Redox Conversion in Lithium–Sulfur Batteries. *Adv. Mater.* **2020**, *32*, 2000315.
- [65] Liang, Z.; Yang, D.; Tang, P.; Zhang, C.; Jacas Biendicho, J.; Zhang, Y.; Llorca, J.; Wang, X.; Li, J.; Heggen, M.; David, J.; Dunin-Borkowski, R. E.; Zhou, Y.; Morante, J. R.; Cabot, A.; Arbiol, J. Atomically dispersed Fe in a C₂N Based Catalyst as a Sulfur Host for Efficient Lithium–Sulfur Batteries. *Adv. Energy Mater.* **2021**, *11*, 2003507.
- [66] He, J.; Bhargav, A.; Manthiram, A. High-Energy-Density, Long-Life Lithium–Sulfur Batteries with Practically Necessary Parameters Enabled by Low-Cost Fe–Ni Nanoalloy Catalysts. *ACS Nano* **2021**, *15*, 8583-8591.

Chapter 3

3 Can metal cations electrocatalyze sulfur redox reaction and suppress polysulfide shuttle?



3.1 Introduction

The sulfur undergoes various structural changes during the charging and discharging of Li-S batteries. In fact, it switches between cyclic sulfur and linear polysulfide. The charge also varies between neutral and negative charge-bearing states. During this process, the sulfur, as well as polysulfide, dissolve in the battery electrolyte. This leads to the deterioration of battery performance upon charge-discharge cycling of the Li-S battery[1-4]. Various approaches have been developed to confine the sulfur into a porous architecture, which in turn was expected to suppress the polysulfides dissolution[5-8]. Some of these porous materials were able to retain large quantities of polysulfides in the pores, which improved the charge-discharge stability. However, it must be noted that the interaction between the pore walls and sulfur/polysulfide is weak. Therefore, leaching is not controlled to a great extent[8-11]. Various other non-porous materials have been synthesized to attract sulfur and polysulfide. They include metal carbides, metal nanoparticles, and carbon materials[12-18]. Several hosts that have Lewis acid-Lewis base interaction, glucose-sulfur interaction, electrostatic attraction, and chalcogen-sulfur interaction have been designed and synthesized[19-24]. Among the non-covalent interactions, polyvalent electrostatic attraction is stronger than most other interactions, hence they have been explored in Li-S batteries. For example, a Nickel based metal-organic framework has been used as a host in Li-S batteries[25,26]. We used Nickel phthalocyanine exfoliated Graphene as a host[27]. In these cases, heteroatoms are also present in addition to the cation. The heteroatoms can impart Lewis acid-Lewis base interaction[24,25,28-33].

To understand the impact of electrostatic interaction in suppressing sulfur/polysulfide dissolution, we need to have materials that are devoid of any other type of interaction. At least, the other interaction must be very weak. Polyvalent electrostatic attraction is much stronger than monovalent and divalent electrostatic interaction. Therefore, we cannot use metal salts alone as a host. The metal cations must be part of a host that leads to polyvalent electrostatic attraction with negative charge-bearing polysulfide. Towards this objective, we have chosen Graphene as a host because, we found that Graphene without heteroatoms is not an effective host[27]. Therefore, we have chosen to decorate the graphene surface with metal cations. The next question is how do we immobilize metal cations on Graphene?

3.2 Experimental Section

3.2.1 Materials

The following chemicals were used as procured. Graphite powder (Sigma-Aldrich, < 20 μm), $\text{NiSO}_4 \cdot 6\text{H}_2\text{O}$ (Sigma-Aldrich), $\text{CoCl}_2 \cdot 6\text{H}_2\text{O}$ (Sigma-Aldrich), Dimethylformamide (DMF, Merck, AR grade), N-Methyl-2-pyrrolidone (NMP, Merck, AR grade), Super P carbon (Imerys Graphite & Carbon Switzerland Ltd., Switzerland), Poly(vinylidene fluoride) (PVDF, Kynar HSV900, Arkema Inc., USA), Li metal (Global nanotech), Celgard 2325 (Polypore, USA), Bis(trifluoromethane)sulfonimide lithium salt (LiTFSI, Sigma-Aldrich, 99.95%), Lithium nitrate (LiNO_3 , Sigma-Aldrich, 99.99%), 1,3-dioxolane (DOL, Sigma Aldrich, 99.8%), and 1,2-dimethoxyethane (DME, Sigma-Aldrich, 99.5 %).

3.2.2 Instrumentations

The TEM images were recorded using Tecnai G2 20 S-TWIN transmission electron microscope. The carbon-coated copper grids (200) were obtained from Ted Pella. The samples for TEM imaging were prepared by dispersing 1 mg of material in DMF, drop-casted onto the carbon-coated copper grid, and dried at 80 $^\circ\text{C}$ for 24 h. The Raman spectroscopy measurements were performed with LabRam spectrometer (HJY, France) equipped with a laser wavelength of 632 nm. The X-ray diffraction spectra were recorded with PANalytical instrument was operated using $\text{Cu K}\alpha$ radiation ($\lambda=1.542 \text{ \AA}$) at a scanning rate of 2° min^{-1} and a step size of 0.02° in 2θ with an operating voltage 40 kV and operating current 30 mA to acquire the X-ray diffraction spectra. The X-ray photoelectron spectroscopy measurements were done on Thermo Kalpha+ spectrometer using $\text{Al K}\alpha$ radiation with an energy of 1486.6 eV. All the spectra were charge corrected with reference to C1s at 284.6 eV. The peak fittings were carried out using CasaXPS software. And the thermogravimetric analyzes were carried out on SDTQ600 TG-DTA analyzer in a nitrogen environment with a ramp of $5^\circ \text{C min}^{-1}$.

3.2.3 Synthesis

Preparation of G-Co and G-Ni:

The graphite powder was exfoliated using Ni^{2+} or Co^{2+} salts as an intercalator. The Graphite (0.5 g) and NiSO_4 or CoCl_2 (2.5 g), were treated for mechanical ball-milling process in an Agate ball mill grinder (250 mL) and six balls with diameter of 1 cm have been used. The milling was carried out at 200 rpm for 60 min. The as-exfoliated materials were washed with copious amount of DMF and dried at 120 $^\circ\text{C}$ under vacuum for 24 h.

Preparation of G-Co/S and G-Ni/S:

The sulfur encapsulation was carried out using melt-diffusion method. The cation doped graphene layers were dried well before the process. The elemental sulfur and cation doped graphene (G/Co or G-Ni) (80:20 ratio) were grinded well and transferred into alumina crucible and heated at 155 °C under an argon atmosphere for 16 h.

3.3 Results and Discussion

We envisioned that the cation- π interaction will facilitate the immobilization of metal cations on the surface of Graphene[34,35]. Nickel salts were ball milled with the Graphite, which led to the formation of few-layer Graphenes with Nickel cations adhering to the surface. Thus, the resultant material comprises positive charges for polyvalent interaction with polysulfides. In our previous work, Nickel cations with heteroatoms have been shown to perform well as hosts in Li-S batteries. Is Nickel unique or does any cation work? To address this question, Graphite was ball-milled with Cobalt salt. The Cobalt cations decorated Graphene has been used as a host in Li-S batteries. Herein, we present the results that corroborate that the Nickel decorated Graphenes are an efficient electrocatalyst for sulfur redox reaction. Please note that the metal cation that is not comprising any ligand acts as an efficient electrocatalyst and suppresses the polysulfide dissolution. Graphite was ball-milled with NiSO₄ salt. We envisioned that the Nickel cations will intercalate into the layers of Graphite. The intercalated cations are expected to adhere on the surface of the Graphenes due to cation- π interaction[34]. Furthermore, the cations are expected to repel each other leading to the exfoliation of Graphene from Graphite. After the ball-milling, the samples were washed with a copious amount of dimethylsulfoxide and dried. This sample will be mentioned as G-Ni in the forthcoming discussions. Graphite was also ball-milled with CoCl₂. This sample will be mentioned as G-Co.

3.3.1 Raman spectroscopy

Extensively washed and dried samples were subjected to Raman analysis.. For G-Ni and G-Co, G and 2D bands appeared at 1570 cm⁻¹ and 2653 cm⁻¹, respectively. The D and D' bands appeared at 1330 cm⁻¹ and 1610 cm⁻¹, respectively (Figure 3.1). The ratio of intensities of D and G bands (I_D/I_G) provides information about the Graphene layers[35]. The I_D/I_G for G-Ni and G-Co are 0.45 and 0.35, respectively. On the other hand, I_D/I_G is 0.08 for Graphite. The high I_D/I_G observed in case of G-Ni and G-Co indicates the presence of few-layer Graphenes in these two samples. The $I_D/I_{D'}$ provides information about the defects in the Graphenes[35,36]. The $I_D/I_{D'}$ were found to be 1.05 for both G-Ni and G-Co. $I_D/I_{D'}$ less than

3.5 indicates the absence of sp^3 and basal plane defects. This indicates that the Graphenes exfoliated using metal salts are of high quality.

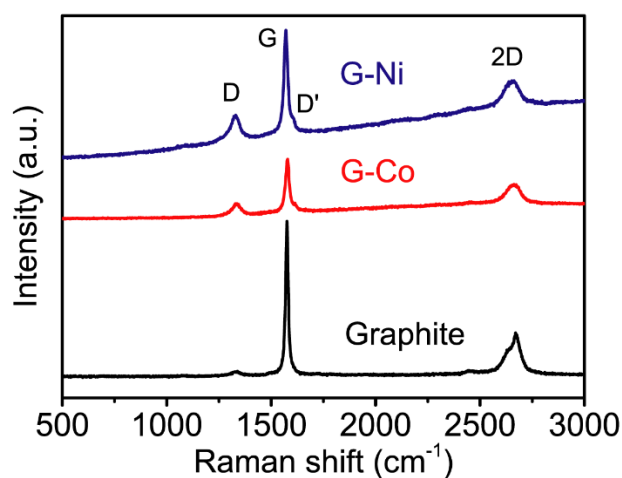


Figure 3.1. Raman spectra showing D, D', G and 2D bands of Graphite, G-Co and G-Ni.

3.3.2 X-ray diffraction analysis

The d spacing of pristine graphite was found to be 3.31 Å (Figure 3.2a), which increased to 3.34 Å for G-Co (Figure 3.2b). The d-spacing further increased to 3.37 Å for G-Ni (Figure 3.2c) due to Ni-Phthalocyanine.

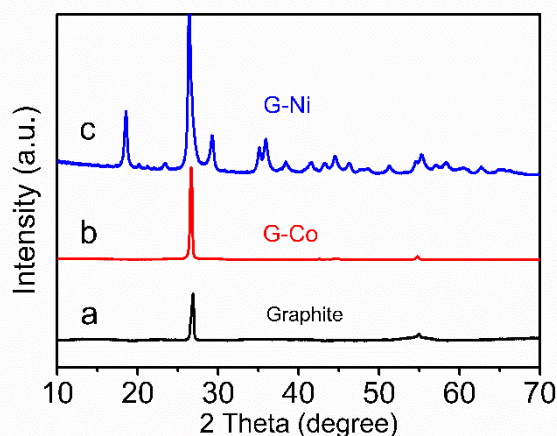


Figure 3.2. XRD pattern for Graphite, G-Co and G-Ni.

3.3.3 X-ray photoelectron spectroscopy

The X-Ray photoelectron spectroscopy (XPS) spectrum for G-Co, the XPS spectrum comprises Co $2p_{3/2}$ (781.7 eV) and Co $2p_{1/2}$ (797.6 eV). The C 1s spectrum demonstrates the sp^2 C (284.4 eV), sp^3 C (285.2 eV), C-O (285.7 eV) and C=O (289.2 eV) and the Cl 2p spectrum exists the Cl $2p_{3/2}$ (199.1 eV) and Cl $2p_{1/2}$ (200.7 eV) are shown in Figure 3.3.

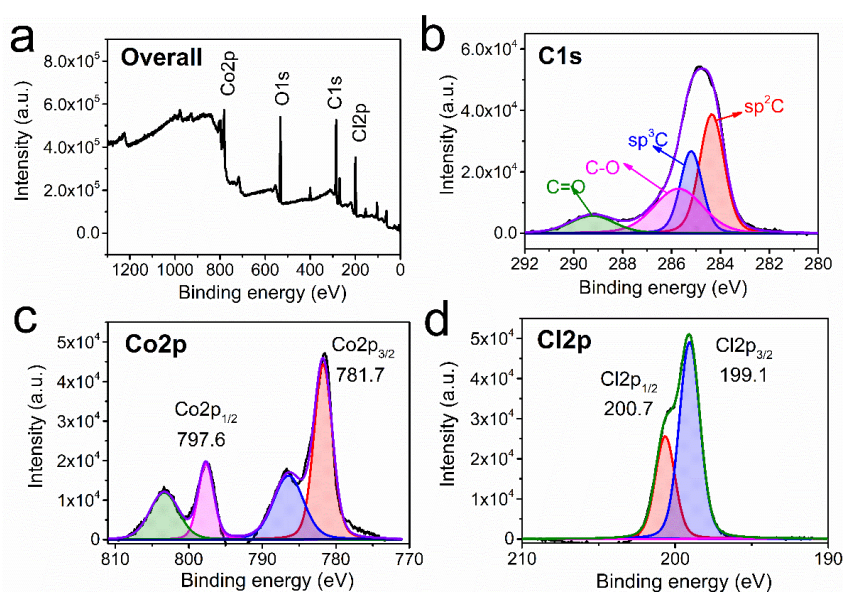


Figure 3.3. XPS spectra of G-Co (a), deconvolution curves of C1s (b), Co2p (c) and Cl2p (d) spectra.

For the G-Ni comprises the Ni 2p_{3/2} and Ni 2p_{1/2} spin orbits at 857.4 eV and 875.2 eV, respectively. The XPS spectrum of C 1s shows the existence of sp²C (284.2 eV), sp³C (285.3 eV), C-O (285.8 eV) and C=O (288.9 eV). Also, the S 2p spectrum consists of S 2p_{3/2} (162.6 eV) and S 2p_{1/2} (169.6 eV) and the O 1s spectrum consists of SO₄²⁻ (532.2 eV) and O-H (533.4 eV) as shown in Figure 3.4. The O-H peak is likely due to the moisture present in NiSO₄.

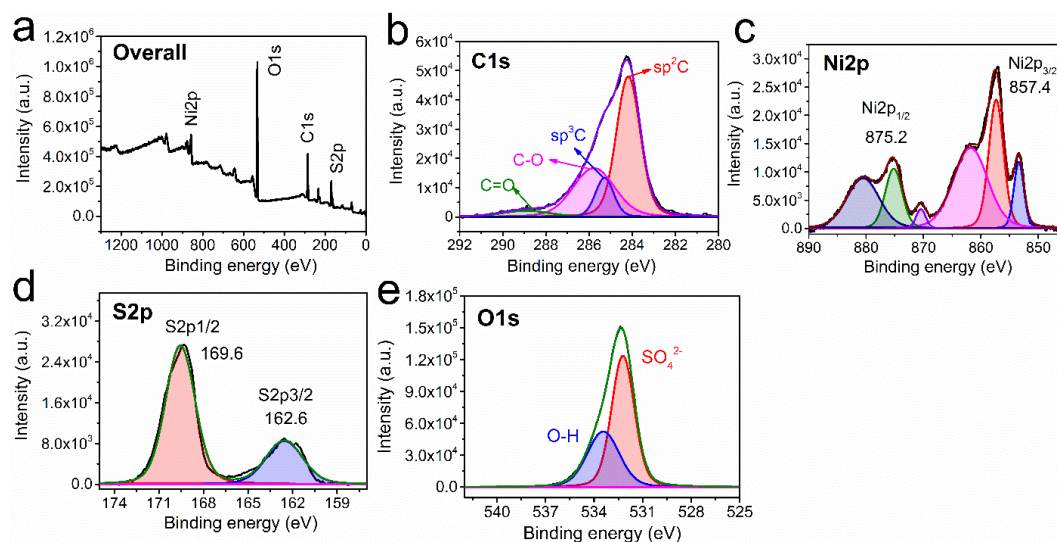


Figure 3.4. XPS survey of G-Ni (a), C1s (b) Ni2p (c) S2p (d) and O1s (e) spectra.

3.3.4 Transmission electron microscope

Transmission electron microscope (TEM) imaging was used to identify the number of Graphene layers present in Graphite, G-Ni, and G-Co. In Graphite, eighty Graphene layers were found (Figure 3.5a). In the case of G-Co, eight Graphene layers were found (Figure 3.5b). The EDAX images indicate that the cobalt cations exist as clusters in various places (Figure 3.6a). In the case of G-Ni, five layers of Graphene were found (Figure 3.5c). The EDAX images indicate that the Nickel cations are present as large clusters. In fact, the clusters are significantly larger than the cobalt clusters of G-Co (Figure 3.6b).

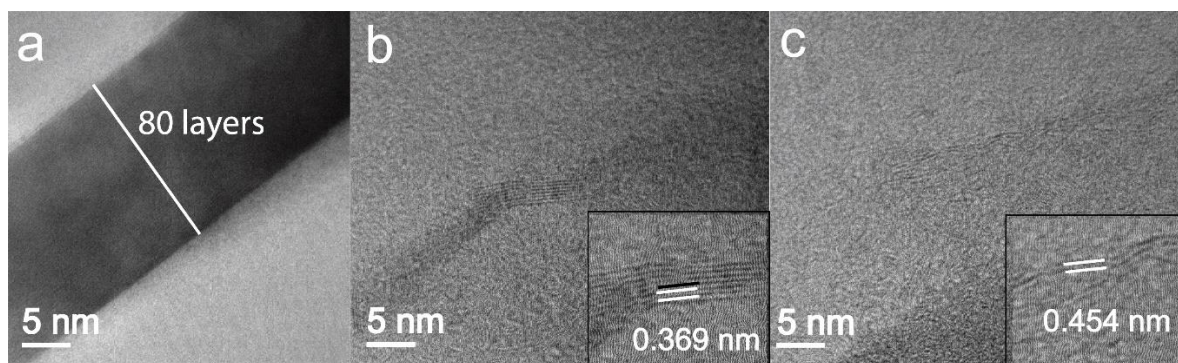


Figure 3.5. TEM imaging of Graphite (a) G-Co (b) and G-Ni (c).

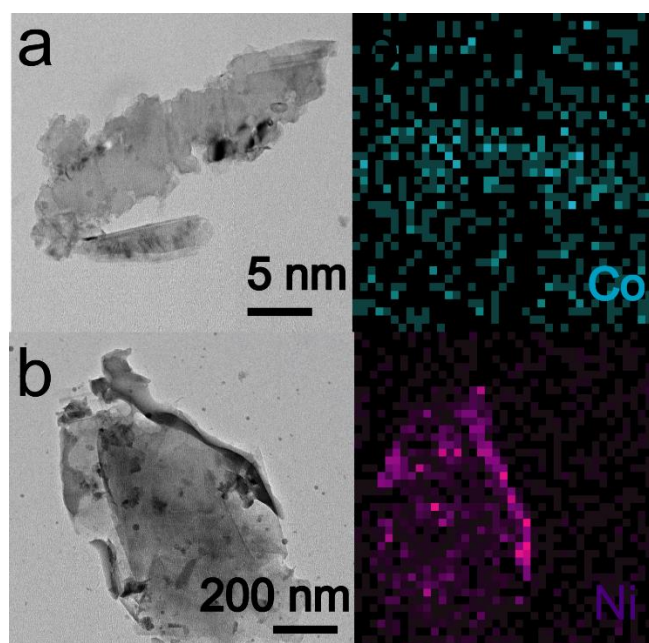


Figure 3.6. TEM imaging and mapping of G-Co and (a) TEM imaging and mapping of G-Ni (b).

3.3.5 Thermogravimetric analysis

Further, we proceeded to study the efficacy of sulfur loading on G-Co and G-Ni. The TGA experiment indicates the sulfur loading is 69.1% in the case of G-Ni and 62.8% for G-Co (Figure 3.7Figure 2.10).

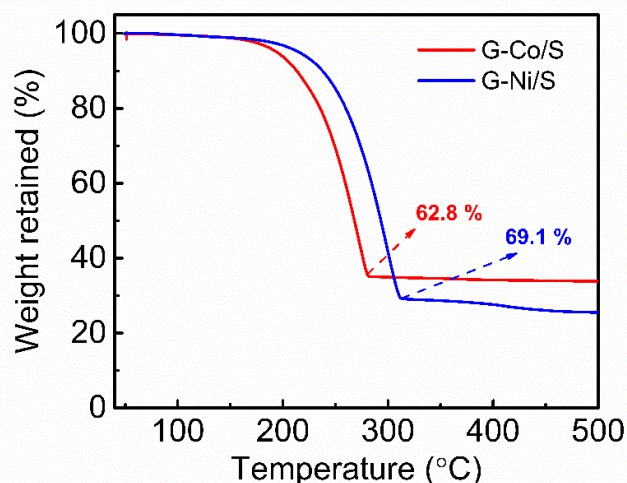


Figure 3.7. Thermogravimetric analysis of G-Co/S and G-Ni/S.

3.3.6 Polysulfide adsorption test

In order to study how efficiently the G-Co and G-Ni absorb polysulfides, a 5 ml solution of S_6^{2-} was added to 1 mg of G-Co and G-Ni. The de-coloration occurred in case of G-Ni, compared to others (insert photograph, Figure 3.9). Further, UV-vis absorption spectra were carried out to relatively quantify the amount of Li_2S_6 in the solution. The UV-vis absorption spectra of S_6^{2-} solution exhibited two peaks at 263 nm and 280 nm (Figure 3.9). As an internal standard, diketopyrrolopyrrole (DPP) (Figure 3.8) was added. This molecule exhibits absorption maxima at 509 nm and 547 nm. The UV-vis absorption spectra of the aliquots taken from all the vials showed the same absorbance. However, the aliquots taken after 24 hrs exhibited significantly different absorbance. The absorbance decreased in the following order $S_6^{2-} > (S_6^{2-} + \text{Graphite}) > (S_6^{2-} + \text{G-Co}) > (S_6^{2-} + \text{G-Ni})$. Thus, the Nickel cations show better adsorption of polysulfide compared to Cobalt cations. Please note that the absorbance of DPP remained constant, indicating the variation in the absorbance of S_6^{2-} is due to the absorption of the polysulfide on Graphite and exfoliated Graphenes such as G-Co and G-Ni. One of the objectives of this work is to study the electrocatalytic activity of metal cations.

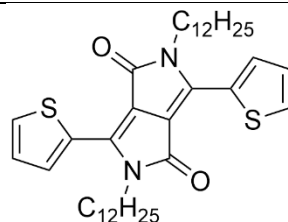


Figure 3.8. Chemical structure of Diketopyrrolopyrrole (DPP).

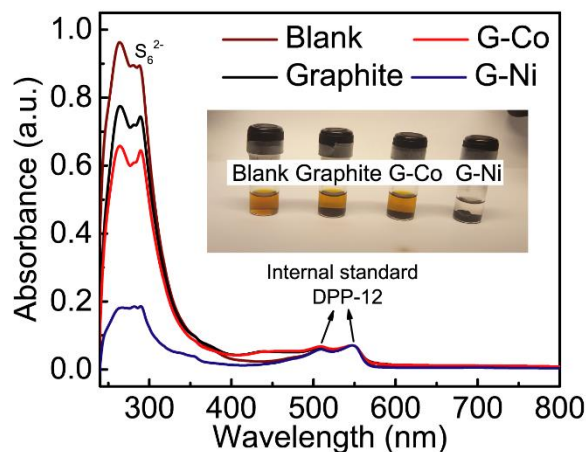


Figure 3.9. UV-Vis spectra of Li_2S_6 solution (Blank) with Graphite, G-Co and G-Ni. The insert shows the de-coloration of the solution due to attraction between Li_2S_6 and G-Ni.

3.4 Electrochemical studies

3.4.1 Electrode preparation

The slurry was prepared using sulfur encapsulated cation doped Graphene (G-Co/S or G-Ni/S) as an active material, Super P carbon and PVDF with the ratio of 7:2:1 in N-Methyl-2-pyrrolidone (NMP) solvent, grinded well and coated onto the carbon-coated aluminum foil and dried at 60 °C for 16 h.

3.4.2 Li-S cell fabrication

The Li-S cells were fabricated using the above-coated electrode as working electrode, Lithium metal as reference, and counter electrode. 1 M LiTFSI as an electrolyte and 0.2 M LiNO_3 as an additive in 1,3-dioxolane (DOL) and 1,2-dimethoxyethane (DME) (1:1 volume ratio) were used, and Celgard 2325 (Thickness 25 μm) as separator. The coin cells (2032 type) were fabricated in an argon filled glovebox (MBRAUN, $\text{O}_2 < 0.1$ ppm, $\text{H}_2\text{O} < 0.1$ ppm). All the electrochemical chemical testings were carried out with potential window of 1.7 – 2.8 V at 25 °C.

3.4.3 Cyclic voltammetry

Li-S batteries were fabricated using the exfoliated Graphenes, Sulfur, conducting carbon, and binder. The cyclic voltammetry techniques were carried out using multichannel Autolab MAC80038 instrument at a scan rate of 0.1 mV/s. In the forward scan of the battery comprising G-Co, two peaks were observed at 2.38 V and 2.41 V (Figure 3.10). These two peaks correspond to $\text{Li}_2\text{S}/\text{Li}_2\text{S}_2 \rightarrow \text{Li}_2\text{S}_n$ ($n = 4$ to 8) and Li_2S_n ($n = 4$ to 8) $\rightarrow \text{Li}_2\text{S}/\text{S}_8$. In the reverse scan, two peaks were observed at 2.04 V and 2.37 V (Figure 3.10). Similarly, two peaks were

observed at 2.4 V and 2.33 V during the forward scan and two peaks were also observed at 2.04 V and 2.34 V in the reverse scan while using G-Ni as electrode material (Figure 3.10). Usually, in the forward scan, one peak is observed due to poor electrocatalytic activity of the host material. In fact, we did observe only a single peak while using doped Graphene as electrode[27]. The two well-defined peaks in the forward scan while using G-Co and G-Ni as electrodes is an indication of efficient electrocatalysis of Sulfur redox reaction.

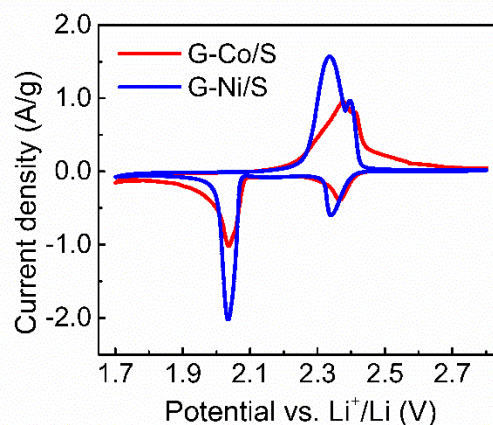


Figure 3.10. Cyclic voltammogram of Li-S cell with scan rate of 0.1 mV/s using G-Co/S and G-Ni/S.

3.4.4 Charge-discharge experiments

The Li-S battery prepared using G-Co was subjected to charge-discharge experiment. At 0.1 C, the specific capacity at the first cycle was 998 mAh/g. This is significantly higher than Graphene without metal ions. Upon charge-discharge cycling, the specific capacity decreased to 375 mAh/g at the 100th cycle (Figure 3.11a). The retention of specific capacity is 38%. Upon increasing the C rate, the specific capacity at the first cycle also decreased. The decrease in the specific capacity at the first cycle decreased in the following order, 0.1 C (998 mAh/g) > 0.2 C (912 mAh/g) > 0.5 C (885 mAh/g) > 1 C (528 mAh/g) > 2 C (494 mAh/g) (Figure 3.11b). At the 100th charge-discharge cycle, the specific capacity retention is as follows, 0.1 C (38%) > 0.2 C (37%) < 0.5 C (46%) < 1 C (72%) < 2 C (74%). From this data, it is clear that the fading is significantly lower upon increase in C rate. However, we must also keep in mind that the initial specific capacity is low at higher C rates. The rate performance of the Li-S battery was studied by changing the C rate of charge-discharge of a battery. At 0.1 C rate, the specific capacity was 940 mAh/g, which decreased upon increase in C rate. At 2 C rate, the specific capacity was 356 mAh/g. Subsequently, the battery's performance was studied at 0.1 C. The specific capacity increased to 714 mAh/g, which is ~230 mAh/g lower than the specific capacity observed at 0.1 C measured at the start of the experiment (Figure 3.11c). The

degradation of battery performance is due to the dissolution of sulfur/polysulfide in the electrolyte. The batteries were subjected to 500 charge-discharge cyclings. The specific capacity retention of the batteries as a function of C rates are 19% (0.2 C) 26% (0.5 C) 48% (1 C) 45% (2 C) (Figure 3.11d). The specific capacity retention is not impressive.

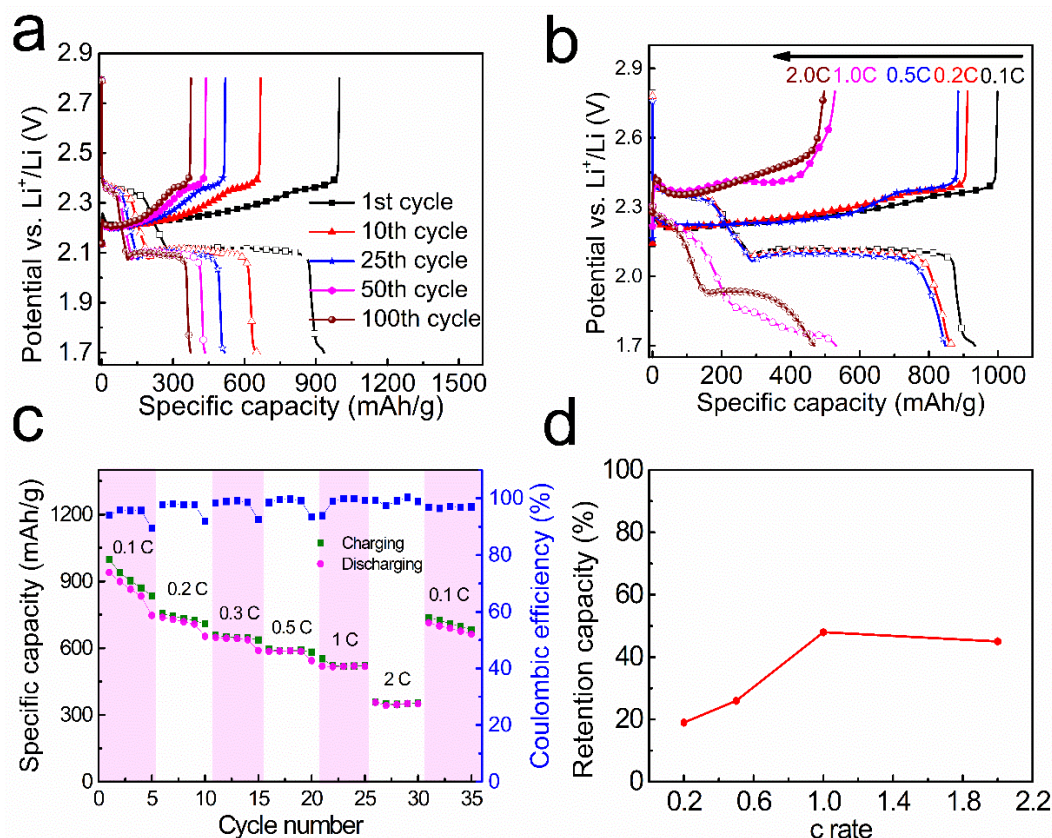


Figure 3.11. Charge/discharge profile of Li-S cell with G-Co/S at 0.1 C rate (a) and first cycle at various rates (0.1 C , 0.2 C , 0.5 C , 1 C and 2 C) (b), Rate performance studies (c), and percentage retention with respect to various C rates of Li-S battery using G-Co (d).

In the next set of experiments, Li-S batteries were fabricated using G-Ni as the host material. At 0.1 C , the specific capacity was 1022 mAh/g, which is higher than that was observed for batteries prepared using G-Co as the host material. At 100th cycle, the specific capacity decreased to 926 mAh/g (Figure 3.12a). The specific capacity retention is 91%, which is impressive. Furthermore, we measured the specific capacity of the battery at various C rates. The specific capacity at the first cycle as a function of various C rates varied as follows, 0.1 C (1022 mAh/g) > 0.2 C (996 mAh/g) > 0.5 C (960 mAh/g) > 1 C (797 mAh/g) > 2 C (738 mAh/g). At 100th cycle, the specific capacity retention as a function of C rates is 0.1 C (91%) > 0.2 C (78%) > 0.5 C (68%) < 1 C (75%) > 2 C (73%) (Figure 3.12b). From this data, it is clear that the specific capacity retention is comparable as a function of C rate variation except at 0.1 C . We proceeded to study the rate performance characteristics of the battery. The specific

capacity at 0.1 C was 1153 mAh/g, which decreased to 554 mAh/g while the battery was subjected to charge-discharge at 2 C rate. Subsequently, the battery's specific capacity was measured at 0.1 C . The specific capacity was found to be 991 mAh/g, which is comparable to the specific capacity measured at 0.1 C at the start of the experiment (Figure 3.12c). From this experiment, we conclude that the sulfur/polysulfide dissolution is insignificant while using G-Ni as a host material. Considering the battery's impressive performance, we studied the battery's stability as a function of 500 charge-discharge cyclings. The specific capacity retention at 500th cycle was 57% at 0.1 C . The specific retention was 49% and 38% for 0.2 C and 2 C , respectively (Figure 3.12d).

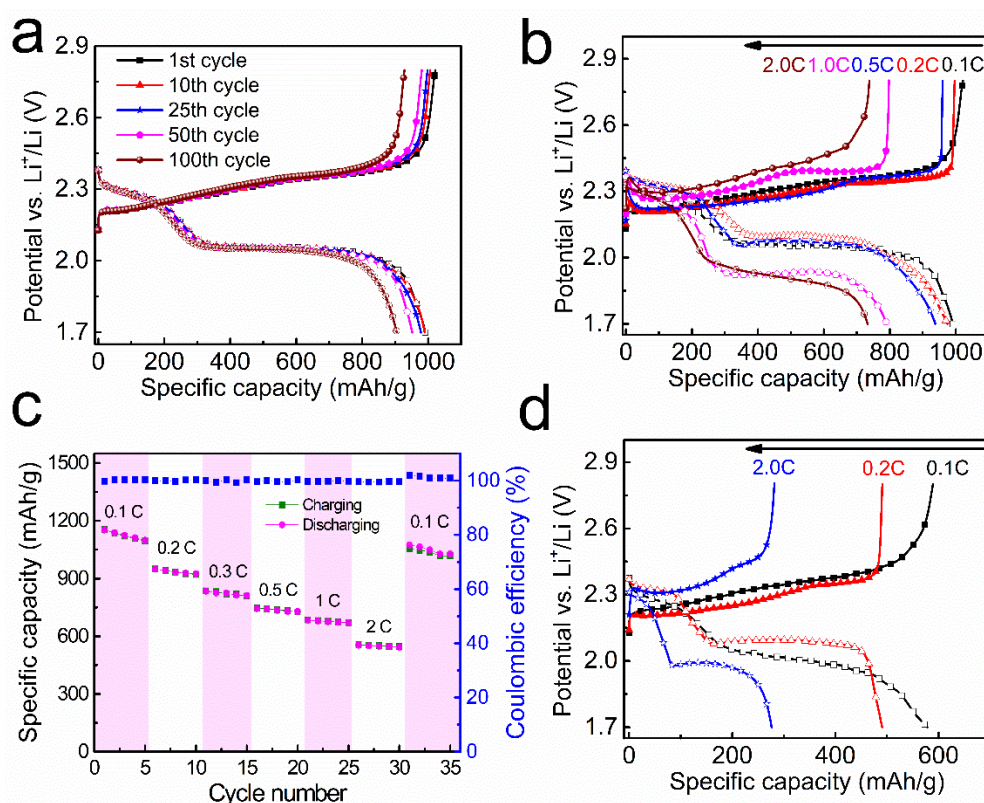


Figure 3.12. Charge/discharge profile of Li-S cell using G-Ni at 0.1 C rate for 100 cycles (a) and first cycle of different rates (0.1 C , 0.2 C , 0.5 C , 1 C and 2 C) (b), Rate performance studies of Li/S cell using G-Ni/S (c) Charge/Discharge profiles of Li-S cells at 500th cycle using G-Ni/S with different rates (0.1 C , 0.2 C and 2 C) (d).

Thus, the specific capacity retention, as well as the specific capacity of the batteries fabricated using G-Ni is better than G-Co. The other question is, does the adherence of metal cations on Graphene improve battery performance? For example, if the nickel salt is blended with Graphite (situation prior to ball milling of Graphite with nickel salts), will the battery perform as good as G-Ni? To test this, Graphite was mixed with NiSO₄ and this sample will be

mentioned as Graphite-Ni. Li-S batteries were fabricated using Graphite-Ni. All other experimental parameters are similar to the Li-S battery fabricated using G-Ni. The specific capacity of the battery was measured at two C rates. At $0.5 C$, the discharge capacity of the first cycle was 470 mAh/g (Figure 3.13), which is half of that observed for batteries fabricated using G-Ni. At 100th cycles, the specific capacity decreased to 234 mAh/g, which is about three times lower than that was observed for G-Ni based batteries. At $1 C$ rate, the specific capacity of the first cycle for Graphite-Ni batteries was 382 mAh/g (Figure 3.13), which is half that of the batteries with G-Ni batteries. A similar trend was observed at 100th cycles. Thus, it is essential to ball-mill Graphite with metal salts and obtain metal cation adhered Graphene to facilitate polyvalent interaction and electrocatalysis.

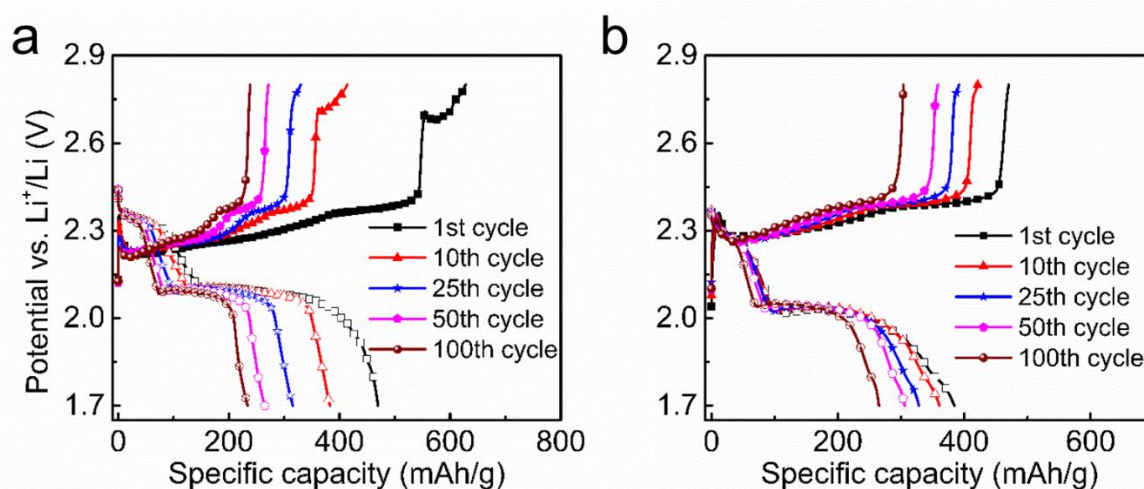


Figure 3.13. Charge/Discharge profiles of Li-S cells at $0.5 C$ (a) and $1 C$ (b) rate using Graphite-Ni (graphite and NiSO_4 mixed)/Sulfur composite.

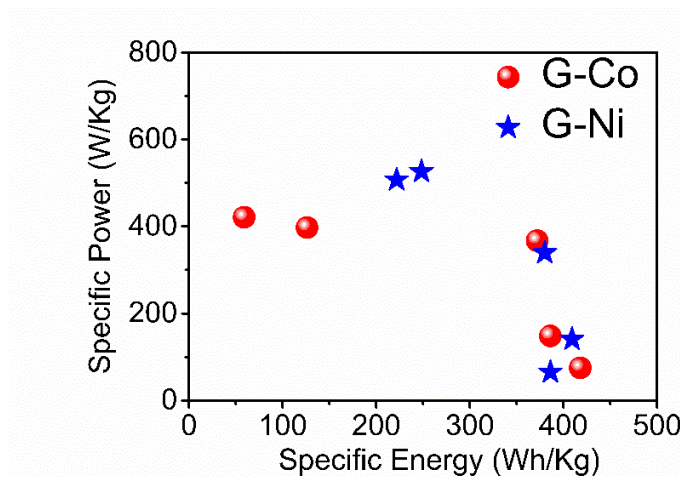


Figure 3.14. Ragone plot for Li-S cell using G-Co and G-Ni comprised sulfur electrodes.

The Ragone plot was computed with the specific energy and specific power (Figure 3.14). The G-Ni based batteries exhibited maximum specific energy of 409 Wh/kg and a maximum specific power of 526 W/kg.

3.4.5 Symmetric cell assembly and Tests

Further, to study the electrochemical aspect, symmetric cells were fabricated using either G-Ni as electrodes or G-Co as electrodes. This method has been well-established in the literature to study the electrocatalysis of sulfur[37-39]. The cyclic voltammogram of the cells was recorded between -1 V and +1 V (Figure 3.15). The first oxidation peak at 0.09 V for G-Ni and at 0.35 V for G-Co correspond to the conversion of Li_2S to Li_2S_6 . The second extremely weak oxidation peak at 0.53 V for G-Ni and at 0.56 V for G-Co correspond to the conversion of Li_2S_6 to S_8 . In the reverse scan, the first reduction peaks at -0.07 V (G-Ni) and -0.38 V (G-Co) are due to reduction of S_8 to Li_2S_6 . The second reduction peak at -0.55 V (G-Ni) and -0.76 V (G-Co) are due to reduction of Li_2S_6 to Li_2S .

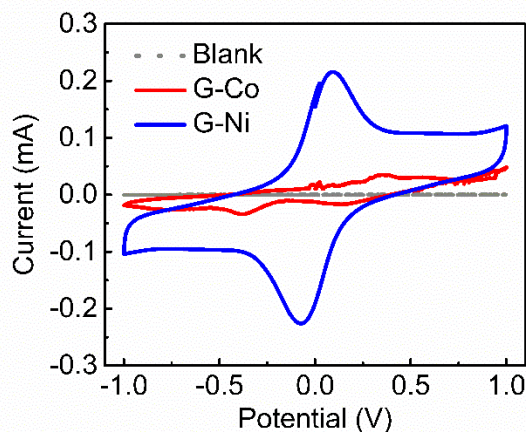


Figure 3.15. Cyclic voltammogram of symmetric cells comprising G-A, G-M, G-M-T (a), and G-NP (b). The dashed plots are the experiments carried out without Li_2S_6 .

3.5 Conclusion

In conclusion, we prepared cation-decorated Graphenes by ball milling NiSO_4 and CoCl_2 . The Nickel decorated Graphene (G-Ni) was found to attract polysulfide effectively, indicating its ability as a good host in Li-S battery. The cyclic voltammogram corroborated the electrocatalytic activity of G-Ni. The batteries fabricated using G-Ni exhibited a maximum specific capacity of 1022 mAh/g. The battery retained 91% of its initial specific capacity upon 100 charge-discharge cycles and 57% at the 500th cycle. The data clearly proved that the Nickel cations are capable of electrocatalysing the sluggish Sulfur redox reaction and suppressing the polysulfide dissolution in the battery electrolyte.

3.6 References

- [1] Manthiram, A.; Fu, Y.; Su, Y.-S. Challenges and Prospects of Lithium–Sulfur Batteries. *Acc. Chem. Res.* **2013**, *46*, 1125-1134.
- [2] Rosenman, A.; Markevich, E.; Salitra, G.; Aurbach, D.; Garsuch, A.; Chesneau, F. F. Review on Li-Sulfur Battery Systems: an Integral Perspective. *Adv. Energy Mater.* **2015**, *5*, 1500212.
- [3] Ji, X.; Nazar, L. F. Advances in Li–S batteries. *J. Mater. Chem.* **2010**, *20*, 9821-9826.
- [4] Manthiram, A.; Fu, Y.; Chung, S.-H.; Zu, C.; Su, Y.-S. Rechargeable Lithium–Sulfur Batteries. *Chem. Rev.* **2014**, *114*, 11751-11787.
- [5] Manthiram, A.; Chung, S.-H.; Zu, C. Lithium–Sulfur Batteries: Progress and Prospects. *Adv. Mater.* **2015**, *27*, 1980-2006.
- [6] Fan, X.; Sun, W.; Meng, F.; Xing, A.; Liu, J. Advanced chemical strategies for lithium–sulfur batteries: A review. *Green Energy Environ.* **2018**, *3*, 2-19.
- [7] Yang, L.; Li, Q.; Wang, Y.; Chen, Y.; Guo, X.; Wu, Z.; Chen, G.; Zhong, B.; Xiang, W.; Zhong, Y. A review of cathode materials in lithium-sulfur batteries. *Ionics* **2020**, *26*, 5299-5318.
- [8] Eftekhari, A.; Kim, D.-W. Cathode materials for lithium–sulfur batteries: a practical perspective. *J. Mater. Chem. A* **2017**, *5*, 17734-17776.
- [9] Kang, W.; Deng, N.; Ju, J.; Li, Q.; Wu, D.; Ma, X.; Li, L.; Naebe, M.; Cheng, B. A review of recent developments in rechargeable lithium–sulfur batteries. *Nanoscale* **2016**, *8*, 16541-16588.

- [10] Han, K.; Shen, J.; Hao, S.; Ye, H.; Wolverton, C.; Kung, M. C.; Kung, H. H. Free-Standing Nitrogen-doped Graphene Paper as Electrodes for High-Performance Lithium/Dissolved Polysulfide Batteries. *ChemSusChem* **2014**, *7*, 2545-2553.
- [11] Zhao, M.-Q.; Liu, X.-F.; Zhang, Q.; Tian, G.-L.; Huang, J.-Q.; Zhu, W.; Wei, F. Graphene/Single-Walled Carbon Nanotube Hybrids: One-Step Catalytic Growth and Applications for High-Rate Li-S Batteries. *ACS Nano* **2012**, *6*, 10759-10769.
- [12] Zhang, C.; Cui, L.; Abdolhosseinzadeh, S.; Heier, J. Two-dimensional MXenes for lithium-sulfur batteries. *InfoMat*. **2020**, *2*, 613-638.
- [13] Hong, X.-J.; Song, C.-L.; Wu, Z.-M.; Li, Z.-H.; Cai, Y.-P.; Wang, C.-X.; Wang, H. Sulfophilic and lithophilic sites in bimetal nickel-zinc carbide with fast conversion of polysulfides for high-rate Li-S battery. *Chem. Eng. J.* **2021**, *404*, 126566.
- [14] Peng, H.-J.; Zhang, G.; Chen, X.; Zhang, Z.-W.; Xu, W.-T.; Huang, J.-Q.; Zhang, Q. Enhanced Electrochemical Kinetics on Conductive Polar Mediators for Lithium-Sulfur Batteries. *Angew. Chem. Int. Ed.* **2016**, *55*, 12990-12995.
- [15] Ng, S.-F.; Lau, M. Y. L.; Ong, W.-J. Lithium-Sulfur Battery Cathode Design: Tailoring Metal-Based Nanostructures for Robust Polysulfide Adsorption and Catalytic Conversion. *Adv. Mater.* **2021**, *33*, 2008654.
- [16] Huang, K.-X.; Hua, J.; Chang, G.-G.; Li, Z.; Tian, G.; Chen, M.-J.; Li, J.-X.; Ke, S.-C.; Yang, X.-Y.; Chen, B. Confined Thermolysis for Oriented N-Doped Carbon Supported Pd toward Stable Catalytic and Energy Storage Applications. *Small* **2021**, *17*, 2002811.
- [17] Tsao, Y.; Gong, H.; Chen, S.; Chen, G.; Liu, Y.; Gao, T. Z.; Cui, Y.; Bao, Z. A Nickel-Decorated Carbon Flower/Sulfur Cathode for Lean-Electrolyte Lithium-Sulfur Batteries. *Adv. Energy Mater.* **2021**, *11*, 2101449.
- [18] Shaibani, M.; Mirshekarloo Meysam, S.; Singh, R.; Easton Christopher, D.; Cooray, M. C. D.; Eshraghi, N.; Abendroth, T.; Dörfler, S.; Althues, H.; Kaskel, S.; Hollenkamp Anthony, F.; Hill Matthew, R.; Majumder, M. Expansion-tolerant architectures for stable cycling of ultrahigh-loading sulfur cathodes in lithium-sulfur batteries. *Sci. Adv.* **2020**, *6*, eaay2757.
- [19] Li, Y.; Lin, S.; Wang, D.; Gao, T.; Song, J.; Zhou, P.; Xu, Z.; Yang, Z.; Xiao, N.; Guo, S. Single Atom Array Mimic on Ultrathin MOF Nanosheets Boosts the Safety and Life of Lithium-Sulfur Batteries. *Adv. Mater.* **2020**, *32*, 1906722.
- [20] Niu, S.; Lv, W.; Zhang, C.; Li, F.; Tang, L.; He, Y.; Li, B.; Yang, Q.-H.; Kang, F. A carbon sandwich electrode with graphene filling coated by N-doped porous carbon layers for lithium-sulfur batteries. *J. Mater. Chem. A* **2015**, *3*, 20218-20224.
- [21] Wu, Q.; Chen, Y.; Hao, X.; Zhu, T.; Cao, Y.; Wang, W. Insight into the Anchoring Effect of Two-Dimensional TiX_2 ($X = S, Se, Te$) Materials for Lithium-Sulfur Batteries: A DFT Study. *J. Electrochem. Soc.* **2021**, *168*, 120516.
- [22] Ye, H.; Lee, J. Y. Solid Additives for Improving the Performance of Sulfur Cathodes in Lithium-Sulfur Batteries—Adsorbents, Mediators, and Catalysts. *Small Methods* **2020**, *4*, 1900864.
- [23] Huang, Y.; Shaibani, M.; Gamot, T. D.; Wang, M.; Jovanović, P.; Dilusha Cooray, M. C.; Mirshekarloo, M. S.; Mulder, R. J.; Medhekar, N. V.; Hill, M. R.; Majumder, M. A saccharide-based binder for efficient polysulfide regulations in Li-S batteries. *Nat. Commun.* **2021**, *12*, 5375.
- [24] Du, Z.; Chen, X.; Hu, W.; Chuang, C.; Xie, S.; Hu, A.; Yan, W.; Kong, X.; Wu, X.; Ji, H.; Wan, L.-J. Cobalt in Nitrogen-Doped Graphene as Single-Atom Catalyst for High-Sulfur Content Lithium-Sulfur Batteries. *J. Am. Chem. Soc.* **2019**, *141*, 3977-3985.
- [25] Zheng, J.; Tian, J.; Wu, D.; Gu, M.; Xu, W.; Wang, C.; Gao, F.; Engelhard, M. H.; Zhang, J.-G.; Liu, J.; Xiao, J. Lewis Acid-Base Interactions between Polysulfides and Metal Organic Framework in Lithium Sulfur Batteries. *Nano Lett.* **2014**, *14*, 2345-2352.
- [26] Wang, S.; Huang, F.; Zhang, Z.; Cai, W.; Jie, Y.; Wang, S.; Yan, P.; Jiao, S.; Cao, R. Conductive metal-organic frameworks promoting polysulfides transformation in lithium-sulfur batteries. *J. Energy Chem.* **2021**, *63*, 336-343.
- [27] Kumar, S.; Krishnamoorthy, K. Concurrent Polyvalent Interaction and Electrocatalysis to Improve Lithium-Sulfur Battery Performance. *Batteries & Supercaps* **2021**, *5*, e202100229.
- [28] Hossain, M. A.; Tulaphol, S.; Thapa, A. K.; Rahaman, M. S.; Jasinski, J. B.; Wang, H.; Sunkara, M. K.; Syzdek, J.; Ozdemir, O. K.; Ornstein, J. M.; Sathitsuksanoh, N. Metal-Organic Framework

Separator as a Polyselenide Filter for High-Performance Lithium–Selenium Batteries. *ACS Appl. Energy Mater.* **2021**, *4*, 13450-13460.

[29] Niu, X.-Q.; Wang, X.-L.; Xie, D.; Wang, D.-H.; Zhang, Y.-D.; Li, Y.; Yu, T.; Tu, J.-P. Nickel Hydroxide-Modified Sulfur/Carbon Composite as a High-Performance Cathode Material for Lithium Sulfur Battery. *ACS Appl. Mater. Interfaces* **2015**, *7*, 16715-16722.

[30] Duan, H.; Wang, C.; Li, G.; Tan, H.; Hu, W.; Cai, L.; Liu, W.; Li, N.; Ji, Q.; Wang, Y.; Lu, Y.; Yan, W.; Hu, F.; Zhang, W.; Sun, Z.; Qi, Z.; Song, L.; Wei, S. Single-Atom-Layer Catalysis in a MoS₂ Monolayer Activated by Long-Range Ferromagnetism for the Hydrogen Evolution Reaction: Beyond Single-Atom Catalysis. *Angew. Chem. Int. Ed.* **2021**, *60*, 7251-7258.

[31] Kang, J.; Xue, Y.; Yang, J.; Hu, Q.; Zhang, Q.; Gu, L.; Selloni, A.; Liu, L.-M.; Guo, L. Realizing Two-Electron Transfer in Ni(OH)₂ Nanosheets for Energy Storage. *J. Am. Chem. Soc.* **2022**, *144*, 8969-8976.

[32] He, Y.; Liu, L.; Zhu, C.; Guo, S.; Golani, P.; Koo, B.; Tang, P.; Zhao, Z.; Xu, M.; Zhu, C.; Yu, P.; Zhou, X.; Gao, C.; Wang, X.; Shi, Z.; Zheng, L.; Yang, J.; Shin, B.; Arbiol, J.; Duan, H.; Du, Y.; Heggen, M.; Dunin-Borkowski, R. E.; Guo, W.; Wang, Q. J.; Zhang, Z.; Liu, Z. Amorphizing noble metal chalcogenide catalysts at the single-layer limit towards hydrogen production. *Nat. Catal.* **2022**, *5*, 212-221.

[33] Kang, J.; Qiu, X.; Hu, Q.; Zhong, J.; Gao, X.; Huang, R.; Wan, C.; Liu, L.-M.; Duan, X.; Guo, L. Valence oscillation and dynamic active sites in monolayer NiCo hydroxides for water oxidation. *Nat. Catal.* **2021**, *4*, 1050-1058.

[34] Zhao, G.; Zhu, H. Cation– π Interactions in Graphene-Containing Systems for Water Treatment and Beyond. *Adv. Mater.* **2020**, *32*, 1905756.

[35] León, V.; Rodríguez, A. M.; Prieto, P.; Prato, M.; Vázquez, E. Exfoliation of Graphite with Triazine Derivatives under Ball-Milling Conditions: Preparation of Few-Layer Graphene via Selective Noncovalent Interactions. *ACS Nano* **2014**, *8*, 563-571.

[36] Rodríguez, A. M.; González, V. J.; León, V.; Herrero, M. A.; Muñoz-García, A. B.; Pavone, M.; Prieto, P.; De La Hoz, A.; Vázquez, E. Molecular adsorption of iminotriazine derivatives on graphene. *J. Phys.: Mater.* **2020**, *3*, 034011.

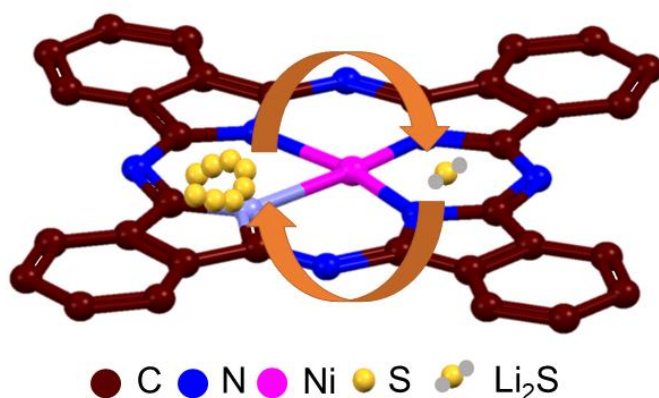
[37] Wang, R.; Luo, C.; Wang, T.; Zhou, G.; Deng, Y.; He, Y.; Zhang, Q.; Kang, F.; Lv, W.; Yang, Q.-H. Bidirectional Catalysts for Liquid–Solid Redox Conversion in Lithium–Sulfur Batteries. *Adv. Mater.* **2020**, *32*, 2000315.

[38] Liang, Z.; Yang, D.; Tang, P.; Zhang, C.; Jacas Biendicho, J.; Zhang, Y.; Llorca, J.; Wang, X.; Li, J.; Heggen, M.; David, J.; Dunin-Borkowski, R. E.; Zhou, Y.; Morante, J. R.; Cabot, A.; Arbiol, J. Atomically dispersed Fe in a C₂N Based Catalyst as a Sulfur Host for Efficient Lithium–Sulfur Batteries. *Adv. Energy Mater.* **2021**, *11*, 2003507.

[39] He, J.; Bhargav, A.; Manthiram, A. High-Energy-Density, Long-Life Lithium–Sulfur Batteries with Practically Necessary Parameters Enabled by Low-Cost Fe–Ni Nanoalloy Catalysts. *ACS Nano* **2021**, *15*, 8583-8591.

Chapter 4

4 Exploring the catalytic effect of Transition Metal Decorated Carbonized Phthalocyanine materials for Li-S Battery

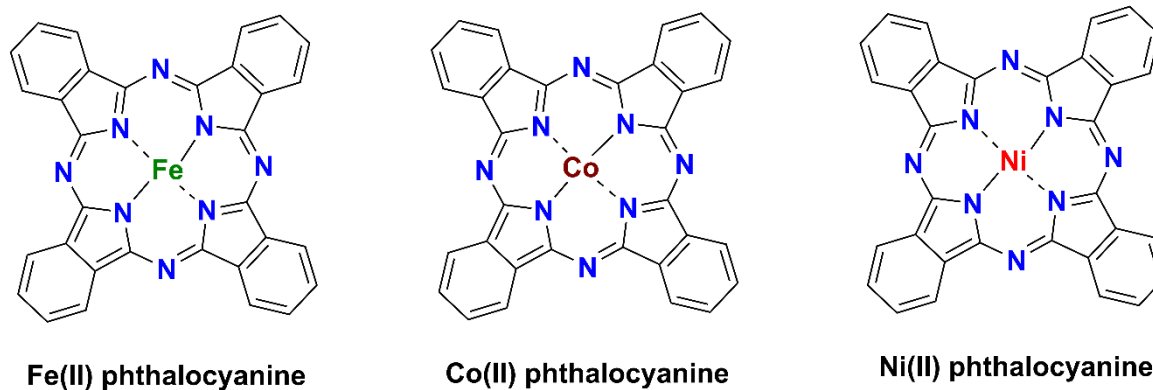


4.1 Introduction

Li-S batteries have received great attention due to their attractive specific capacity and energy density, cost effective and environment friendliness.[1-4] However, these Sulfur based batteries unable to replace the conventional batteries due to inadequate utilization of active sulfur and continuous capacity decay.[5] Unlike LIBs, the Li-S batteries undergo the conversation mechanisms of active material, and the Sulfur converts into Lithium polysulfides (LiPSs) (Li_2S_n , $n = 2$ to 8).[1] These polysulfides are highly soluble in liquid electrolyte, activates the so called “shuttling effect” and degrades the Li counter electrode. Moreover Sulfur and its discharge products are electrically insulating which creates internal resistance and consequently slows down the conversion kinetics.[6-9] To overcome these challenges, wide range of catalytic materials were introduced.[10] Since, Nazar et al. developed the carbon matrices as host for elemental Sulfur,[11] a wide range of research has been carried out in the conducting additives. The recent research is mainly focused on developing the Sulfur host to withhold the polysulfides.[12-15] The micro/meso porous carbon materials are effective host for the Sulfur.[16-20] Porous organic polymers, MOFs and COFs are developed as conductive materials for Li-S batteries.[21-23] The polymer-based materials are used as host/binders to suppress polysulfide dissolution. The graphene-based materials such as exfoliated graphene,[24-27] graphene oxide (GO),[28,29] heteroatom functionalized graphene,[30-33] metal decorated graphenes[34] are widely investigated for Li-S batteries. The heteroatoms (N, S, B, and P) decorated carbon matrices are prevent the polysulfide dissolution in electrolytes.[35-39] These heteroatoms are insufficient to hold the polysulfides in large quantity, hence the metal based materials are focused as an alternative promising materials.[21,40-45] The metals are inherently Lewis-acids (soft acids) and preferably interacts with S_n^{2-} . In addition, metal oxides and metal sulfides are enhance the cyclic performance, conversion kinetics by trapping the polysulfides.[21,46-50] We have also thoroughly examined in our previous chapters where Ni stands superior to reduce polysulfide dissolution. The question arises whether nickel is unique or other transitional metals also have such behaviour. To answer this, we designed different transition metal decorated phthalocyanines (M-Phs) as sulfur host. M-Phs are known to have obvious catalytic property and high chemical stability. Kim et.al. adopted Co centered fluorinated phthalocyanine as catalytic material to improve specific capacity in Li-S battery.[51]

Therefore, we have chosen various metals (M=Fe, Co, and Ni) incorporated into the Phthalocyanine core. Scheme 4.1 But, Phthalocyanines do not offer the pores in it. So, these

Metal-Phthalocyanines (M-Phs) are carbonized to attain a porous nature. We anticipate that the Lewis-acidic behaviour of these metals, along with ring-structured carbon from the Phthalocyanines, could efficiently withhold the LiPSs.[49]



Scheme 4.1. Structures of Metal-Phthalocyanines (Fe, Co, and Ni).

4.2 Experimental Section

4.2.1 Materials

The following chemicals were procured and used without any purification. Nickel-Phthalocyanine (Sigma-Aldrich), Iron-Phthalocyanine (Sigma-Aldrich), Cobalt-Phthalocyanine (Sigma-Aldrich), Dimethylformamide (DMF, Merck, AR grade), N-Methyl-2-pyrrolidone (NMP, Merck, AR grade), Super P carbon (Imerys Graphite & Carbon Switzerland Ltd., Switzerland), Poly(vinylidene fluoride) (PVDF, Kynar HSV900, Arkema Inc., USA), Li metal (Global nanotech), Celgard 2325 (Polypore, USA), Bis(trifluoromethane)sulfonimide lithium salt (LiTFSI, Sigma-Aldrich, 99.95%), Lithium nitrate (LiNO_3 , Sigma-Aldrich, 99.99%), 1,3-dioxolane (DOL, Sigma Aldrich, 99.8%), and 1,2-dimethoxyethane (DME, Sigma-Aldrich, 99.5 %).

4.2.2 Instrumentations

The X-ray diffraction spectra were recorded with a PANalytical instrument was operated using Cu $K\alpha$ radiation ($\lambda=1.542 \text{ \AA}$) at a scanning rate of 2° min^{-1} and a step size of 0.02° in 2θ with an operating voltage of 40 kV and operating current 30 mA to acquire the X-ray diffraction spectra. The X-ray photoelectron spectroscopy measurements were done on a Thermo Kalpha+ spectrometer using Al $K\alpha$ radiation with an energy of 1486.6 eV. All the spectra were charge-corrected with reference to C1s at 284.6 eV. The peak fittings were carried out using CasaXPS software. The FESEM imaging and EDAX were recorded with Nova Nano 450, FEI company. The samples for FESEM imaging were prepared by dispersing 1 mg of material in DMF, drop-

casted onto the Silicon wafer, and dried at 80 °C for 24 h. And the thermogravimetric analysis was carried out on an SDTQ600 TG-DTA analyzer in a nitrogen environment with a ramp of 5 °C min⁻¹ for all the samples.

4.2.3 Synthesis

Preparation of Fe-Ph, Co-Ph, and Ni-Ph:

The Fe-Phthalocyanine, Co-Phthalocyanine, and Ni-Phthalocyanine (500 mg each) were placed separately into the Alumina ceramic boat, and carbonization for all the samples carried out by thermal treatment at 950 °C with the ramping of 5 °C/min under an Argon atmosphere for 4 h. Further, it allowed it to cool down to RT. The samples were collected and labelled Fe-Ph, Co-Ph, and Ni-Ph, respectively.

Preparation of Fe-Ph/S, Co-Ph/S and Ni-Ph/S:

The elemental Sulfur was introduced into the above carbonized M-Ph materials via the melt-diffusion method. The Sulfur was grinded well with Fe-Ph, Co-Ph, and Ni-Ph, individually, with a mass ratio of 8:2, till a uniform mixture was obtained. Further, it was transferred to an alumina crucible and thermally treated at 155 °C under an argon atmosphere for 16 h. The materials were collected, labelled as Fe-Ph/S, Co-Ph/S, and Ni-Ph/S, respectively, and stored in a dry place.

4.3 Results and Discussion

The M-Phs consist of Metals in the central cavity of the phthalocyanine framework contributes to enhance the electrocatalytic activity of the sluggish redox reaction of elemental Sulfur and LiPSs. The phthalocyanine framework consists of four Nitrogen atoms with lone pairs of electrons, which have affinity toward LiPSs, and alleviate the dissolution of LiPSs.[51,52] Each of the metal(II) ions are individually bonding with phthalocyanine frameworks, which prevents the aggregation of metal(II) ions. Metal nanoparticles (NPs) are widely used in Li-S systems to prevent the PSs dissolution in the electrolyte.[45] Unfortunately, loading the high amount of elemental Sulfur in these metal NPs are challenging. It is envisioned that Our carbonized phthalocyanines help to load the Sulfur and Metal(II) ions at the centre[53] and facilitate the electrochemical conversion reactions of Sulfur and LiPSs.

4.3.1 X-ray diffraction analysis

The X-ray diffraction (XRD) pattern of Fe-Phthalocyanine, Co-Phthalocyanine, and Ni-Phthalocyanine shows the presence of β -phase (Figure 4.1a).[54,55] Further, the XRD analyses

were carried out post-carbonization process (Figure 4.1b). All the M-Ph powders were demonstrated (Figure 4.1a) almost the similar 002 phase and observed the better packing for pyrolyzed samples are shown in Figure 4.1b.

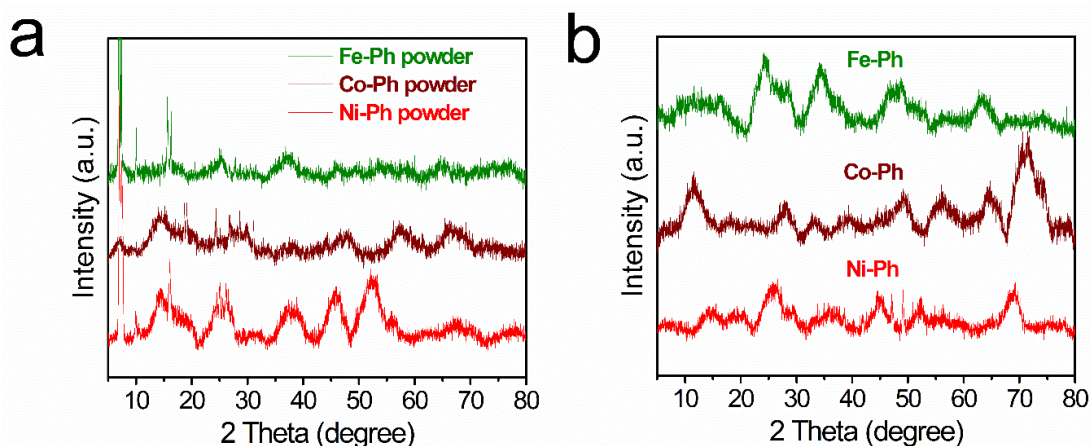


Figure 4.1. XRD pattern for Fe-Ph, Co-Ph, and Ni-Ph powders (a), and carbonized Fe-Ph, Co-Ph, and Ni-Ph samples.

4.3.2 X-ray photoelectron spectroscopy

The X-Ray photoelectron spectroscopy (XPS) spectra were recorded for the carbonized samples of Fe-Ph, Co-Ph, and Ni-Ph. The Fe-Ph sample demonstrates the Fe $2p_{3/2}$ (711.5) and Fe $2p_{1/2}$ (723.1 eV) orbits, with the existence of sp^2C (284.3 eV), sp^3C (284.9 eV), C-O (286.5 eV) and C=O (289.8 eV). Further, N 1s deconvolution spectra exhibit the Pyridinic N (23.48 %), Pyrrolic N (43.03 %), and Graphitic N (33.49 %) at 398.2 eV, 400.1 eV, 402 eV, respectively, as shown in Figure 4.2. In case of Co-Ph, the deconvoluted spectrum of C 1s exhibits the sp^2C (284.3 eV), sp^3C (285.0 eV), C-O (289.5 eV), and C=O (287.2 eV), combined with Co $2p_{3/2}$ (780.7 eV) and Co $2p_{1/2}$ (796.5 eV) orbits, and Pyridinic N (30.15 %) Pyrrolic N (47.52 %), and Graphitic N (22.33 %) at 398.2 eV, 400.1 eV, 402.5 eV, respectively (Figure 4.3).

Further, Ni-Ph demonstrates the Ni $2p_{3/2}$ (873.5 eV) and Ni $2p_{1/2}$ (855.7 eV) orbits, with the presence of sp^2C (284.3 eV), sp^3C (285.3 eV), C-O (286.5 eV) and C=O (289.2 eV), and N 1s deconvolution spectra show the presence of Pyridinic N (29.17 %), Pyrrolic N (37.48 %), and Graphitic N (33.35 %) at 398.4 eV, 400.2 eV, 400.8 eV, respectively (Figure 4.4).

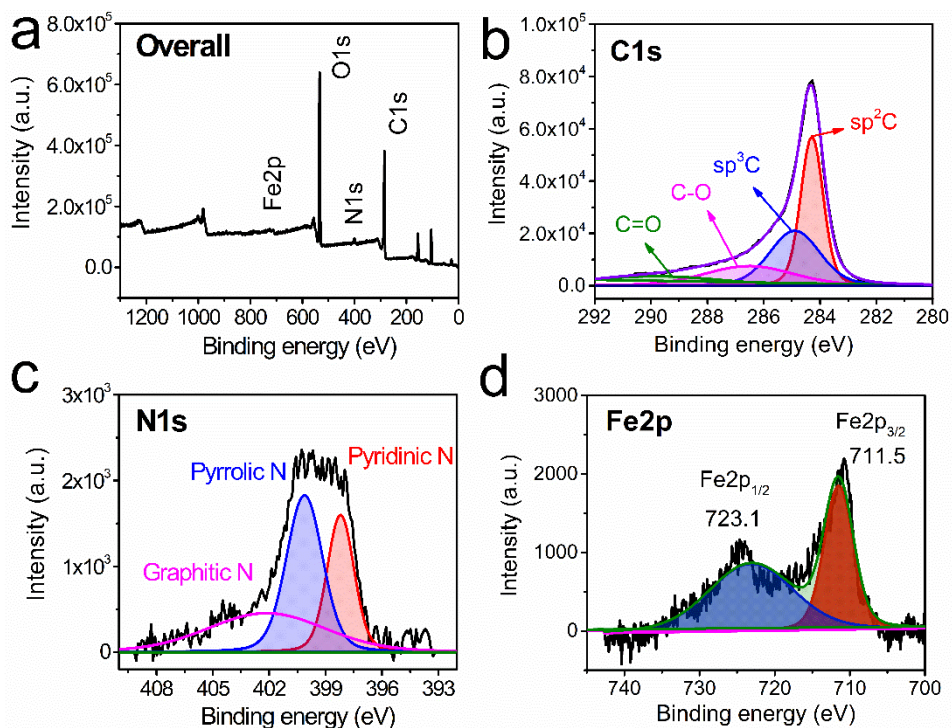


Figure 4.2. XPS survey of Fe-Ph (a), deconvolution curves of C1s (b), N1s (c), and Fe2p (d) spectra.

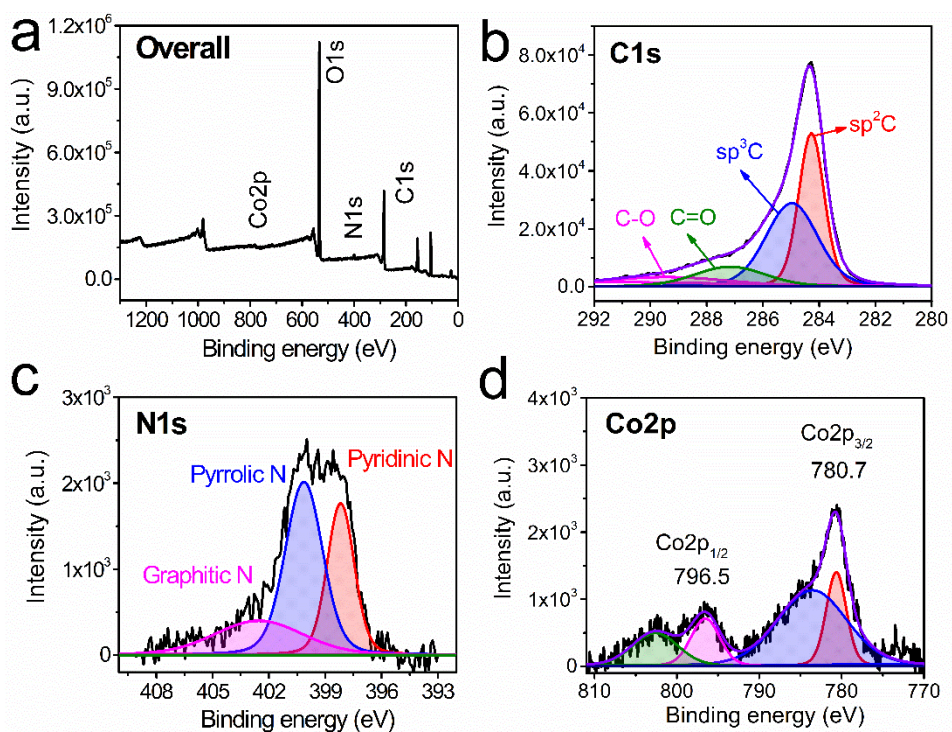


Figure 4.3. XPS survey of Co-Ph (a), deconvolution curves of C1s (b), N1s (c), and Co2p (d) spectra.

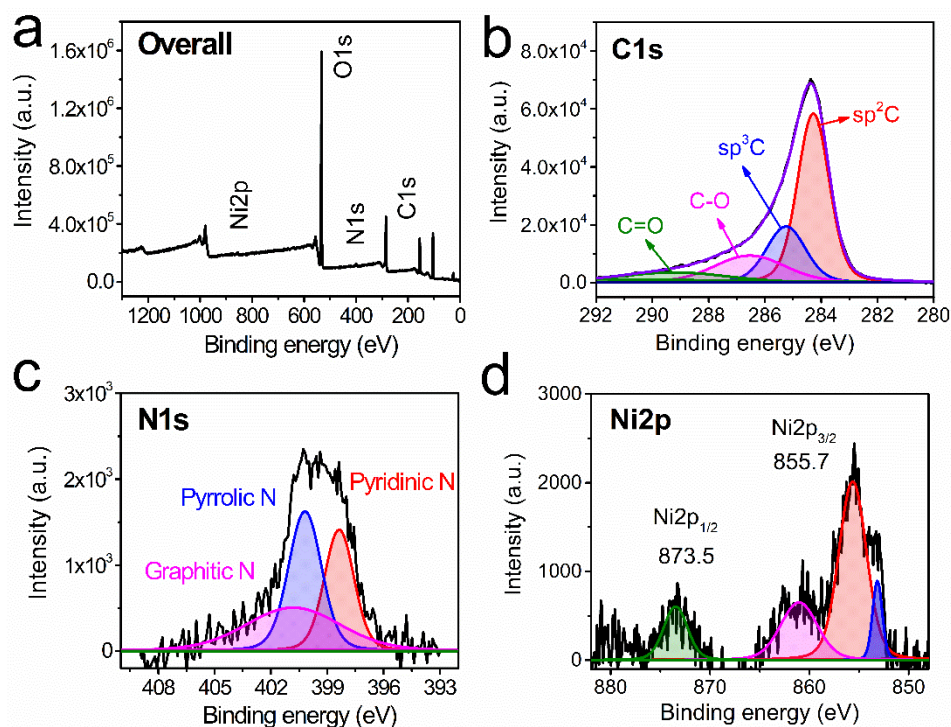


Figure 4.4. XPS survey of Ni-Ph (a), deconvolution curves of C1s (b), N1s (c), and Ni2p (d) spectra.

4.3.3 Scanning electron microscope

Figure 4.5-4.7 shows the morphologies of Fe-Ph, Co-Ph, and Ni-Ph. As Metal-Phthalocyanines contain the maximum backbone of carbon atoms, the highest percentage of carbon is present in all the materials, which is calculated from energy-dispersive X-ray spectroscopy (EDAX) analysis (Figure 4.8). Also, found that the Nitrogen and the respective metals are distributed evenly, confirmed by mapping analysis (Figure 4.5-4.7). The percentages of metals (Fe, Co, and Ni) present in the samples are 6.93 %, 4.15 %, and 4.13 %, respectively (Table 4.1).

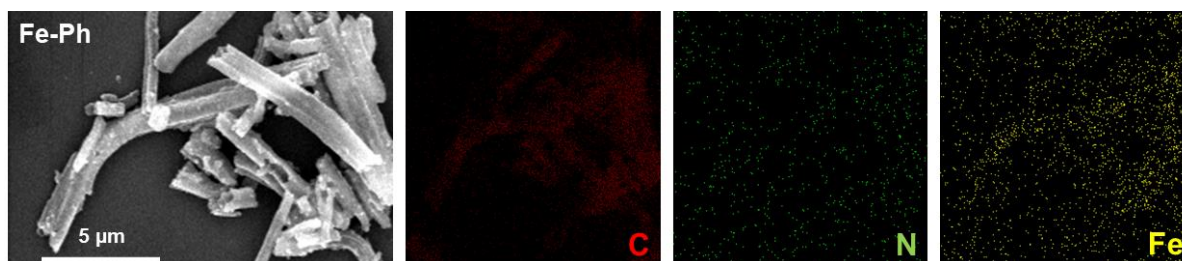


Figure 4.5. FE-SEM imaging of Fe-Ph and mapping of C, N, and Fe.

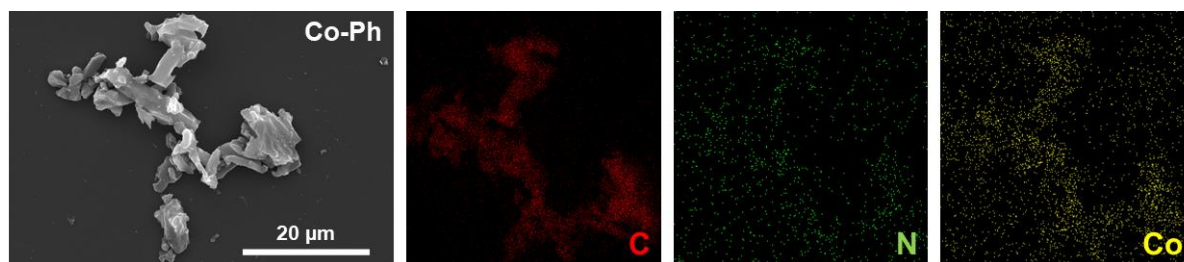


Figure 4.6. FE-SEM imaging of Co-Ph and mapping of C, N, and Co.

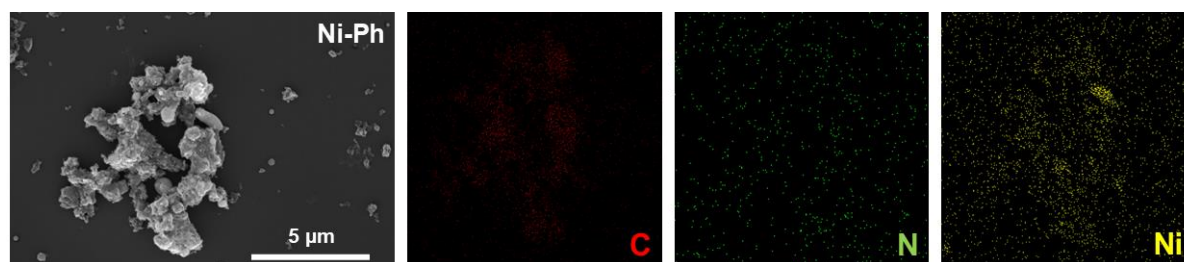


Figure 4.7. FE-SEM imaging of Ni-Ph and mapping of C, N, and Ni.

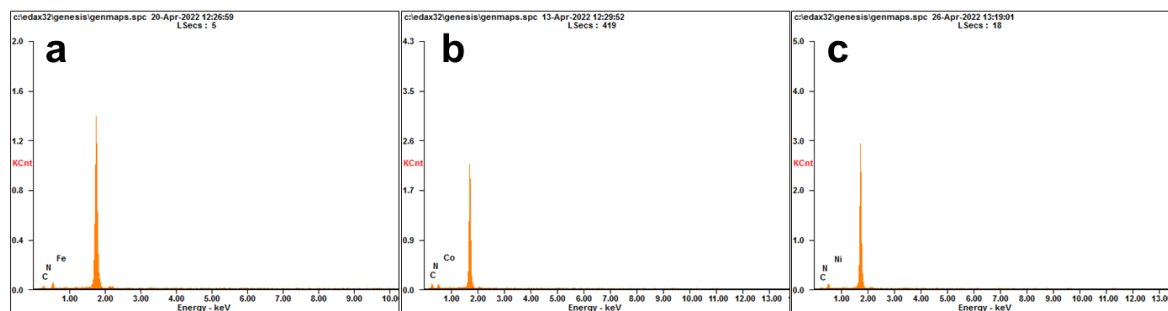


Figure 4.8. Energy-dispersive X-ray spectroscopy (EDAX) analysis of samples Fe-Ph (a), Co-Ph (b), and Ni-Ph (c).

Table 4.1. Chemical compositions of elements in M-Phs obtained from EDAX analysis

Samples	Percentage of elements (Atomic wt %)		
	Carbon	Nitrogen	Metal*
Fe-Ph	84.19	8.89	6.93
Co-Ph	77.41	18.44	4.15
Ni-Ph	64.52	31.35	4.13

* Iron (Fe) for Fe-Ph, Cobalt (Co) for Co-Ph, and Nickel (Ni) for Ni-Ph.

4.3.4 Thermogravimetric analysis

The Sulfur loaded M-Phs are subjected to thermogravimetric analysis (TGA) to quantify the Sulfur present in them. As shown in Figure 4.9, the percentage of Sulfur is 69 %, 73.2 %, and 78.1 % in Fe-Ph, Co-Ph, and Ni-Ph, respectively.

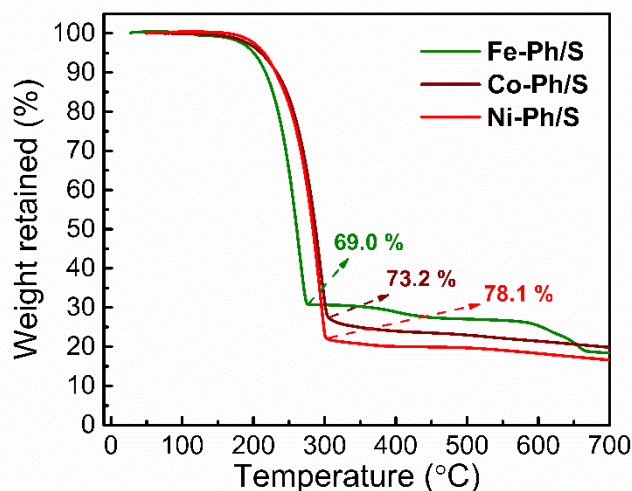


Figure 4.9. Thermogravimetric analysis of Fe-Ph/S, Co-Ph/S, and Ni-Ph/S.

4.4 Electrochemical studies

4.4.1 Electrode preparation

The slurry was prepared by using M-Ph/S (Fe-Ph/S or Co-Ph/S or Ni-Ph/S) as an active material with Super P carbon, and PVDF with the mass ratio of 7:2:1 and N-Methyl-2-pyrrolidone (NMP) as solvent, grinded well, and coated onto the carbon-coated aluminum foil and dried at 60 °C for 16 h.

4.4.2 Li-S cell fabrication

The Li-S cell fabrication was carried out using the M-Ph/S comprised electrodes as working electrodes, and Lithium metal foil served as reference and counter electrode. 1 M Bis(trifluoromethane)sulfonimide lithium salt (LiTFSI) as an electrolyte and 0.2 M LiNO₃ as an additive in 1,3-dioxolane (DOL) and 1,2-dimethoxyethane (DME) (1:1 volume ratio) were used, and Celgard 2325 (Thickness 25 μm) as a separator. The 2032-type coin cells were fabricated in an argon-filled glovebox (MBRAUN, O₂ < 0.1 ppm, H₂O < 0.1 ppm). All the electrochemical chemical tests were carried out with a potential window of 1.7 – 2.8 V at 25 °C.

4.4.3 Cyclic voltammetry

The above fabricated Li-S cells consisting of M-Ph/Ss (Fe-Ph/S or Co-Ph/S or Ni-Ph/S) were subjected to cyclic voltammetry techniques. The experiments were carried out using a multichannel Autolab MAC80038 instrument at a scan rate of 0.1 mV/s. For Fe-Ph/S comprised Li-S cells, the two reduction peaks have appeared at 2.26 V and 2.05, are responsible for the electrochemical conversion of elemental Sulfur to Li_2S_n ($n = 4$ to 8), and further conversion to $\text{Li}_2\text{S}_2/\text{Li}_2\text{S}$, respectively. A single oxidation peak has been observed at 2.43 V, which indicates the reversible conversion of $\text{Li}_2\text{S}_2/\text{Li}_2\text{S}$ to $\text{Li}_2\text{S}_8/\text{S}_8$, as shown in Figure 4.10a. In case of Co-Ph/S-based Li-S cells (Figure 4.10b), the two reduction peaks at 2.28 V and 2.01 V, which indicates the reduction of Sulfur. In the forward scan, two distinguish peaks were observed at 2.36 V and 2.41 V, which are responsible for $\text{Li}_2\text{S}_2/\text{Li}_2\text{S} \rightarrow \text{Li}_2\text{S}_n$ ($4 < n \leq 8$) and Li_2S_n ($4 < n \leq 8$) $\rightarrow \text{S}_8$. These two oxidation peaks are the indication of efficient conversion of LiPSs to Sulfur due to the electrocatalytic activity of the material.

About 75% of the overall capacity of Li-S batteries obtain from the conversion of Li_2S_4 to Li_2S . As a result, Li_2S liquid-solid precipitation process is essential for both its sulfur usage and specific capacity.[45] For Ni-Ph/S comprised Li-S cells, the two reduction, and two oxidation peaks occurred at 2.33 V, 2.05, 2.33 V, and 2.38 V, respectively (Figure 4.10c). These peaks are profound in Ni-Ph-S as compared to Fe-Ph/S and Co-Ph/S. It provides an indication about the electrochemical conversion reactions in Li-S cells based on Ni-Ph/S is efficient as well as maximum utilization of Sulfur.

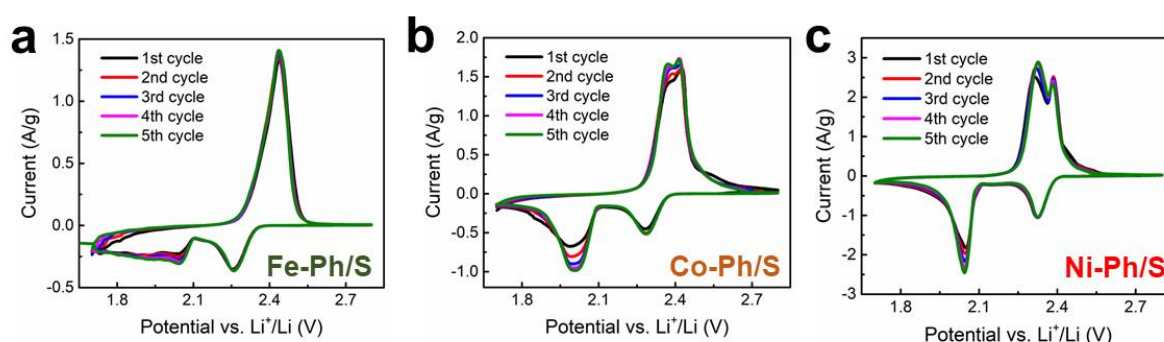


Figure 4.10. Cyclic voltammogram of Li-S cells comprising Fe-Ph/S (a), Co-Ph/S (b), and Ni-Ph/S (c) with a scan rate of 0.1 mV/s.

4.4.4 Charge-discharge experiments

The cyclic charge-discharge experiments were carried out for the Li-S cells comprised of M-Ph/S (Fe-Ph/S or Co-Ph/S or Ni-Ph/S). The Fe-Ph/S-based cell delivered a specific capacity of 877 mAh/g for the first cycle at the rate of 0.5 C. The capacity of this cell gradually faded to 793 mAh/g, 771 mAh/g, and 747 mAh/g on its twenty-fifth, fiftieth, and hundredth cycles, respectively, as shown in Figure 4.11a. The obtained specific capacity of this cell is only half of its theoretical capacity at first cycle. It indicates that Sulfur utilization is bisected in Li-S cells using Fe-Ph/S. The Co-Ph/S loaded Li-S battery exhibits a discharge capacity of 1038 mAh/g at 0.5 C rate (Figure 4.11b), with coulombic efficiency of 98 % for the first cycle, which is considerably higher than the batteries based on Fe-Ph/S. Further, 887 mAh/g and 771 mAh/g have been observed for the fiftieth and hundredth cycles. These losses of specific capacity indicate the lithium polysulfide dissolution and shuttle in the anode compartment.

Further, Ni-Ph/S-based Li-S cells were examined for charge-discharge experiments. At 0.5 C rate, it delivered the specific capacity of 1067 mAh/g for its first cycle (Figure 4.11c). Almost the same capacity (1061 mAh/g) was noticed at the tenth cycle. Further, the retention in specific capacity of 98 %, 96 %, and 88 % was observed at the twenty-fifth, fiftieth, and hundredth cycles. The discharging specific capacity of 939 mAh/g occurred at the hundredth cycle, which was even higher than the efficacy of Li-S cells using Fe-Ph/S at the first cycle. Also, ~99 % coulombic efficiency was observed for Li-S cells using Ni-Ph/S.

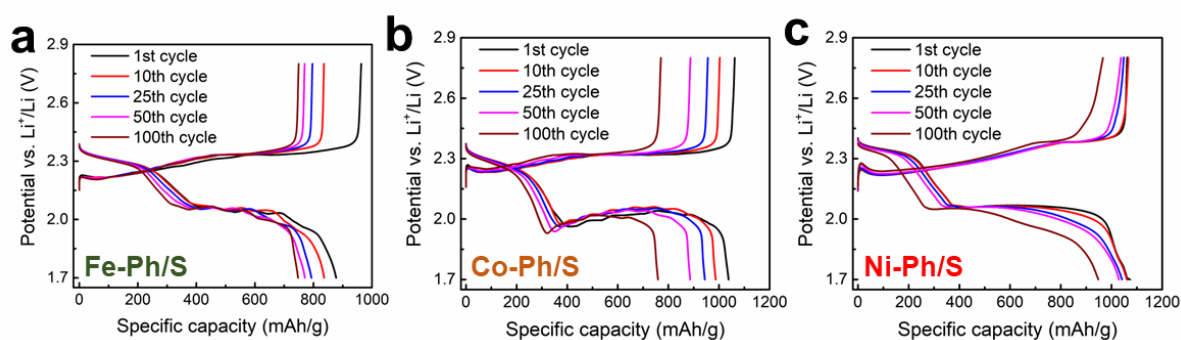


Figure 4.11. Charge/discharge profile of Li-S cells comprised using Fe-Ph/S (a), Co-Ph/S (b), and Ni-Ph/S (c) at 0.5 C rate.

Further, Li-S batteries using Ni-Ph/S were tested with different current rates of 0.1 C, 0.2 C, 1.0 C, and 2.0 C. The cell, at 0.1 C rate, exhibited the 1217 mAh/g of specific capacity for the first cycle, which is 72.7 % of the capacity of actually loaded Sulfur. The coulombic efficiency was 99 % for the above cell, as shown in Figure 4.12a. Later, 954 mAh/g was obtained at the

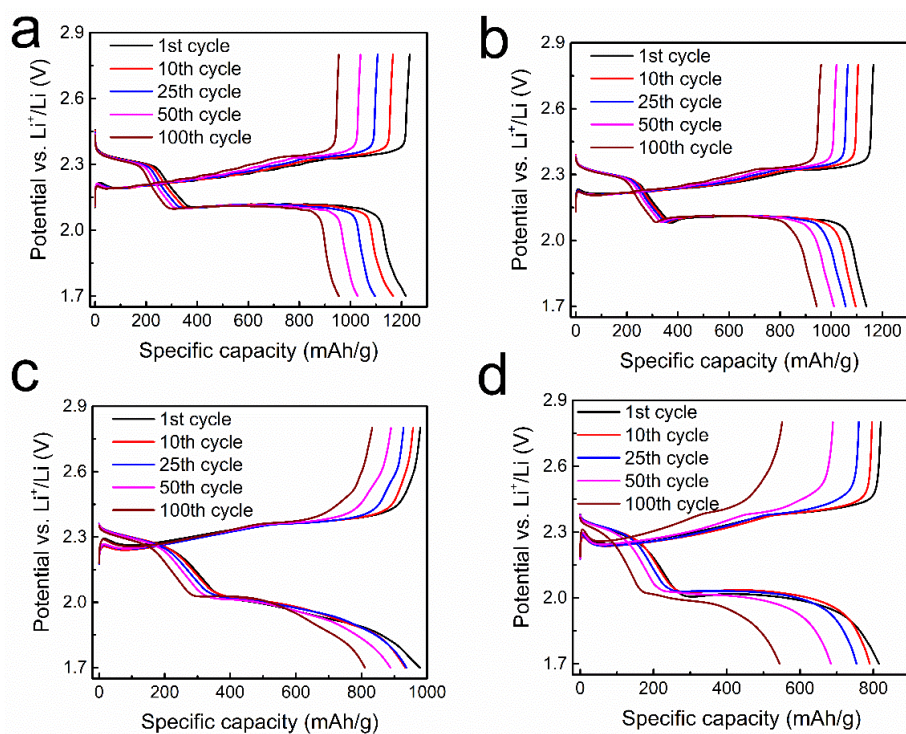


Figure 4.12. Charge/discharge profiles of Li-S cells using Ni-Ph/S-based material at the current rates of 0.1 C (a), 0.2 C (b), 1.0 C (c), and 2.0 C (d).

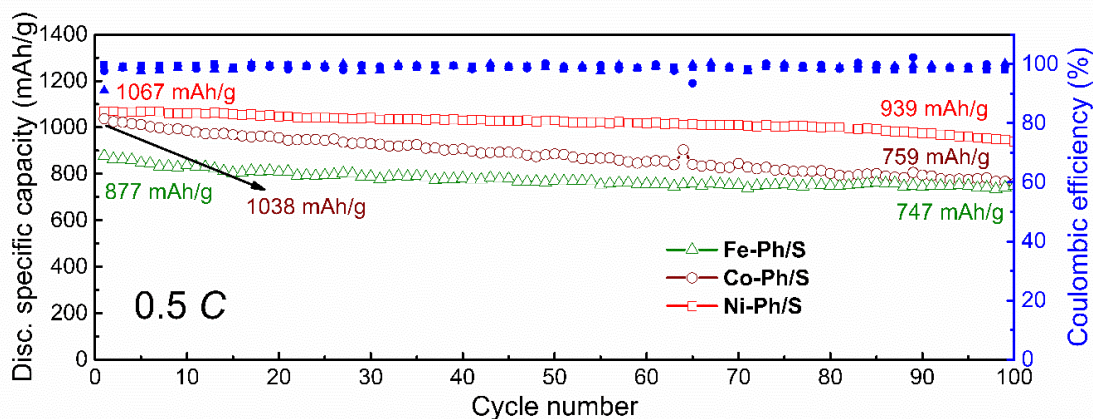


Figure 4.13. Cyclic performances of Li-S cells at 0.5 C, using Fe-Ph/S, Co-Ph/S, and Ni-Ph/S based electrodes.

100th cycle. At 0.2 C rate, the specific capacity of 1165 mAh/g and 960 mAh/g were noticed at 1st and 100th cycles. The significant retention capacity observed at the 100th cycle is 83 % (Figure 4.12b). Also, the cells at 1.0 C (Figure 4.12c), and 2.0 C (Figure 4.12d) rates, were demonstrated an excellent discharging specific capacity of 979 mAh/g and 815 mAh/g for the first cycle, respectively. For the same rates, 822 mAh/g and 553 mAh/g were obtained at the 100th cycle. The cyclic stability at 0.5 C rate for all the M-Phs/S based batteries were displayed in Figure 4.13.

4.5 Conclusion

In this chapter, we have chosen the transition metal-phthalocyanines (Fe, Co, and Ni), which are successfully pyrolyzed to attain the carbonized M-Phs. These materials exploited as cathode host for elemental Sulfur in Li-S battery systems. The porous nature of M-Phs accommodate the elemental Sulfur through the melt diffusion method. The metal cation prevents the battery from capacitive decay by detaining the polysulfide. Among all M-Phs, Nickel based material exhibited the best electrochemical reversibility of polysulfide conversion reactions with better kinetics. The Ni-Ph/S-based electrodes delivered the 1067 mAh/g at the initial cycle, while Fe-Ph/S and Co-Ph/S-based cells delivered at the rate of 0.5 C, 877 mAh/g and 1038 mAh/g, respectively. Further, Ni-Ph/S cells exhibited a remarkably high specific capacity of 939 mAh/g at hundredth cycle, while others delivered poor efficacies.

4.6 References

- [1] Bruce, P. G.; Freunberger, S. A.; Hardwick, L. J.; Tarascon, J.-M. Li–O₂ and Li–S batteries with high energy storage. *Nat. Mater.* **2012**, *11*, 19-29.
- [2] Manthiram, A.; Fu, Y.; Chung, S.-H.; Zu, C.; Su, Y.-S. Rechargeable Lithium–Sulfur Batteries. *Chem. Rev.* **2014**, *114*, 11751-11787.
- [3] Manthiram, A.; Chung, S.-H.; Zu, C. Lithium–Sulfur Batteries: Progress and Prospects. *Adv. Mater.* **2015**, *27*, 1980-2006.
- [4] Rosenman, A.; Markevich, E.; Salitra, G.; Aurbach, D.; Garsuch, A.; Chesneau, F. F. Review on Li-Sulfur Battery Systems: an Integral Perspective. *Adv. Energy Mater.* **2015**, *5*, 1500212.
- [5] Manthiram, A.; Fu, Y.; Su, Y.-S. Challenges and Prospects of Lithium–Sulfur Batteries. *Acc. Chem. Res.* **2013**, *46*, 1125-1134.
- [6] Kaiser, M. R.; Chou, S.; Liu, H.-K.; Dou, S.-X.; Wang, C.; Wang, J. Structure–Property Relationships of Organic Electrolytes and Their Effects on Li/S Battery Performance. *Adv. Mater.* **2017**, *29*, 1700449.
- [7] Di Donato, G.; Ates, T.; Adenusi, H.; Varzi, A.; Navarra, M. A.; Passerini, S. Electrolyte measures to prevent polysulfide shuttle in Li-S batteries. *Batteries & Supercaps* **2022**, *n/a*.
- [8] Brückner, J.; Thieme, S.; Grossmann, H. T.; Dörfler, S.; Althues, H.; Kaskel, S. Lithium–sulfur batteries: Influence of C-rate, amount of electrolyte and sulfur loading on cycle performance. *J. Power Sources* **2014**, *268*, 82-87.
- [9] Sun, K.; Wu, Q.; Tong, X.; Gan, H. Electrolyte with Low Polysulfide Solubility for Li–S Batteries. *ACS Appl. Energy Mater.* **2018**, *1*, 2608-2618.
- [10] Cheng, X.-B.; Huang, J.-Q.; Peng, H.-J.; Nie, J.-Q.; Liu, X.-Y.; Zhang, Q.; Wei, F. Polysulfide shuttle control: Towards a lithium-sulfur battery with superior capacity performance up to 1000 cycles by matching the sulfur/electrolyte loading. *J. Power Sources* **2014**, *253*, 263-268.
- [11] Ji, X.; Lee, K. T.; Nazar, L. F. A highly ordered nanostructured carbon–sulfur cathode for lithium–sulfur batteries. *Nat. Mater.* **2009**, *8*, 500-506.
- [12] Shaibani, M.; Mirshekarloo Meysam, S.; Singh, R.; Easton Christopher, D.; Cooray, M. C. D.; Eshraghi, N.; Abendroth, T.; Dörfler, S.; Althues, H.; Kaskel, S.; Hollenkamp Anthony, F.; Hill Matthew, R.; Majumder, M. Expansion-tolerant architectures for stable cycling of ultrahigh-loading sulfur cathodes in lithium-sulfur batteries. *Sci. Adv.* **2020**, *6*, eaay2757.
- [13] Li, Q.; Zhang, Z.; Guo, Z.; Zhang, K.; Lai, Y.; Li, J. Coaxial-cable structure composite cathode material with high sulfur loading for high performance lithium–sulfur batteries. *J. Power Sources* **2015**, *274*, 338-344.
- [14] Liang, C.; Dudney, N. J.; Howe, J. Y. Hierarchically Structured Sulfur/Carbon Nanocomposite Material for High-Energy Lithium Battery. *Chem. Mater.* **2009**, *21*, 4724-4730.

- [15] Liang, J.; Sun, Z.-H.; Li, F.; Cheng, H.-M. Carbon materials for Li–S batteries: Functional evolution and performance improvement. *Energy Storage Mater.* **2016**, *2*, 76-106.
- [16] Rehman, S.; Gu, X.; Khan, K.; Mahmood, N.; Yang, W.; Huang, X.; Guo, S.; Hou, Y. 3D Vertically Aligned and Interconnected Porous Carbon Nanosheets as Sulfur Immobilizers for High Performance Lithium-Sulfur Batteries. *Adv. Energy Mater.* **2016**, *6*, 1502518.
- [17] Qu, Y.; Zhang, Z.; Zhang, X.; Ren, G.; Lai, Y.; Liu, Y.; Li, J. Highly ordered nitrogen-rich mesoporous carbon derived from biomass waste for high-performance lithium–sulfur batteries. *Carbon* **2015**, *84*, 399-408.
- [18] Ren, G.; Li, S.; Fan, Z.-X.; Warzywoda, J.; Fan, Z. Soybean-derived hierarchical porous carbon with large sulfur loading and sulfur content for high-performance lithium–sulfur batteries. *J. Mater. Chem. A* **2016**, *4*, 16507-16515.
- [19] Xu, G.; Han, J.; Ding, B.; Nie, P.; Pan, J.; Dou, H.; Li, H.; Zhang, X. Biomass-derived porous carbon materials with sulfur and nitrogen dual-doping for energy storage. *Green Chem.* **2015**, *17*, 1668-1674.
- [20] Xu, M.; Jia, M.; Mao, C.; Liu, S.; Bao, S.; Jiang, J.; Liu, Y.; Lu, Z. Aspergillus flavus Conidia-derived Carbon/Sulfur Composite as a Cathode Material for High Performance Lithium–Sulfur Battery. *Sci. Rep.* **2016**, *6*, 18739.
- [21] Huang, K.-X.; Hua, J.; Chang, G.-G.; Li, Z.; Tian, G.; Chen, M.-J.; Li, J.-X.; Ke, S.-C.; Yang, X.-Y.; Chen, B. Confined Thermolysis for Oriented N-Doped Carbon Supported Pd toward Stable Catalytic and Energy Storage Applications. *Small* **2021**, *17*, 2002811.
- [22] Chen, C.-H.; Lin, S.-H.; Wu, Y.-J.; Su, J.-T.; Cheng, C.-C.; Cheng, P.-Y.; Ting, Y.-C.; Lu, S.-Y. MOF-derived cobalt Disulfide/Nitrogen-doped carbon composite polyhedrons linked with Multi-walled carbon nanotubes as sulfur hosts for Lithium-Sulfur batteries. *Chem. Eng. J.* **2022**, *431*, 133924.
- [23] Jiang, S.; Huang, S.; Yao, M.; Zhu, J.; Liu, L.; Niu, Z. Bimetal-organic frameworks derived Co/N-doped carbons for lithium-sulfur batteries. *Chin. Chem. Lett.* **2020**, *31*, 2347-2352.
- [24] Luque, G. L.; Para, M. L.; Primo, E. N.; Bracamonte, M. V.; Otero, M.; Otero, M.; del Carmen Rojas, M.; Soriano, F. J. G.; Lener, G.; Calderón, A., Graphene in Lithium-Ion/Lithium-Sulfur Batteries. In *Advanced Battery Materials*, **2019**; 399-449.
- [25] Zhao, M.-Q.; Liu, X.-F.; Zhang, Q.; Tian, G.-L.; Huang, J.-Q.; Zhu, W.; Wei, F. Graphene/Single-Walled Carbon Nanotube Hybrids: One-Step Catalytic Growth and Applications for High-Rate Li–S Batteries. *ACS Nano* **2012**, *6*, 10759-10769.
- [26] Tang, C.; Zhang, Q.; Zhao, M.-Q.; Huang, J.-Q.; Cheng, X.-B.; Tian, G.-L.; Peng, H.-J.; Wei, F. Nitrogen-Doped Aligned Carbon Nanotube/Graphene Sandwiches: Facile Catalytic Growth on Bifunctional Natural Catalysts and Their Applications as Scaffolds for High-Rate Lithium-Sulfur Batteries. *Adv. Mater.* **2014**, *26*, 6100-6105.
- [27] Ma, Z.; Tao, L.; Liu, D.; Li, Z.; Zhang, Y.; Liu, Z.; Liu, H.; Chen, R.; Huo, J.; Wang, S. Ultrafine nano-sulfur particles anchored on in situ exfoliated graphene for lithium–sulfur batteries. *J. Mater. Chem. A* **2017**, *5*, 9412-9417.
- [28] Zhou, W.; Chen, H.; Yu, Y.; Wang, D.; Cui, Z.; DiSalvo, F. J.; Abruña, H. D. Amylopectin Wrapped Graphene Oxide/Sulfur for Improved Cyclability of Lithium–Sulfur Battery. *ACS Nano* **2013**, *7*, 8801-8808.
- [29] Zhang, L.; Ji, L.; Glans, P.-A.; Zhang, Y.; Zhu, J.; Guo, J. Electronic structure and chemical bonding of a graphene oxide–sulfur nanocomposite for use in superior performance lithium–sulfur cells. *Phys. Chem. Chem. Phys.* **2012**, *14*, 13670-13675.
- [30] Liang, Z.; Yang, D.; Tang, P.; Zhang, C.; Jacas Biendicho, J.; Zhang, Y.; Llorca, J.; Wang, X.; Li, J.; Heggen, M.; David, J.; Dunin-Borkowski, R. E.; Zhou, Y.; Morante, J. R.; Cabot, A.; Arbiol, J. Atomically dispersed Fe in a C₂N Based Catalyst as a Sulfur Host for Efficient Lithium–Sulfur Batteries. *Adv. Energy Mater.* **2021**, *11*, 2003507.
- [31] Yu, M.; Zhou, S.; Wang, Z.; Wang, Y.; Zhang, N.; Wang, S.; Zhao, J.; Qiu, J. Accelerating polysulfide redox conversion on bifunctional electrocatalytic electrode for stable Li-S batteries. *Energy Storage Mater.* **2019**, *20*, 98-107.
- [32] Zhang, Z.; Kong, L.-L.; Liu, S.; Li, G.-R.; Gao, X.-P. A High-Efficiency Sulfur/Carbon Composite Based on 3D Graphene Nanosheet@Carbon Nanotube Matrix as Cathode for Lithium–Sulfur Battery. *Adv. Energy Mater.* **2017**, *7*, 1602543.

- [33] Han, K.; Shen, J.; Hao, S.; Ye, H.; Wolverton, C.; Kung, M. C.; Kung, H. H. Free-Standing Nitrogen-doped Graphene Paper as Electrodes for High-Performance Lithium/Dissolved Polysulfide Batteries. *ChemSusChem* **2014**, *7*, 2545-2553.
- [34] Cui, Z.; Zu, C.; Zhou, W.; Manthiram, A.; Goodenough, J. B. Mesoporous Titanium Nitride-Enabled Highly Stable Lithium-Sulfur Batteries. *Adv. Mater.* **2016**, *28*, 6926-6931.
- [35] Li, X.-Y.; Feng, S.; Zhao, C.-X.; Cheng, Q.; Chen, Z.-X.; Sun, S.-Y.; Chen, X.; Zhang, X.-Q.; Li, B.-Q.; Huang, J.-Q.; Zhang, Q. Regulating Lithium Salt to Inhibit Surface Gelation on an Electrocatalyst for High-Energy-Density Lithium-Sulfur Batteries. *J. Am. Chem. Soc.* **2022**, *144*, 14638-14646.
- [36] Wang, S.; Gao, F.; Ma, R.; Du, A.; Tan, T.; Du, M.; Zhao, X.; Fan, Y.; Wen, M. ZnO Nanoparticles Anchored on a N-Doped Graphene-Coated Separator for High Performance Lithium/Sulfur Batteries. *Metals* **2018**, *8*.
- [37] Balach, J.; Singh, H. K.; Gomoll, S.; Jaumann, T.; Klose, M.; Oswald, S.; Richter, M.; Eckert, J.; Giebeler, L. Synergistically Enhanced Polysulfide Chemisorption Using a Flexible Hybrid Separator with N and S Dual-Doped Mesoporous Carbon Coating for Advanced Lithium-Sulfur Batteries. *ACS Appl. Mater. Interfaces* **2016**, *8*, 14586-14595.
- [38] Cai, J.; Wu, C.; Zhu, Y.; Zhang, K.; Shen, P. K. Sulfur impregnated N, P co-doped hierarchical porous carbon as cathode for high performance Li-S batteries. *J. Power Sources* **2017**, *341*, 165-174.
- [39] Wu, F.; Li, J.; Tian, Y.; Su, Y.; Wang, J.; Yang, W.; Li, N.; Chen, S.; Bao, L. 3D coral-like nitrogen-sulfur co-doped carbon-sulfur composite for high performance lithium-sulfur batteries. *Sci. Rep.* **2015**, *5*, 13340.
- [40] Lu, Y.; Qin, J.-L.; Shen, T.; Yu, Y.-F.; Chen, K.; Hu, Y.-Z.; Liang, J.-N.; Gong, M.-X.; Zhang, J.-J.; Wang, D.-L. Hypercrosslinked Polymerization Enabled N-Doped Carbon Confined Fe₂O₃ Facilitating Li Polysulfides Interface Conversion for Li-S Batteries. *Adv. Energy Mater.* **2021**, *11*, 2101780.
- [41] Ma, S.; Wang, L.; Wang, Y.; Zuo, P.; He, M.; Zhang, H.; Ma, L.; Wu, T.; Yin, G. Palladium nanocrystals-embedded mesoporous hollow carbon spheres with enhanced electrochemical kinetics for high performance lithium sulfur batteries. *Carbon* **2019**, *143*, 878-889.
- [42] Tsao, Y.; Gong, H.; Chen, S.; Chen, G.; Liu, Y.; Gao, T. Z.; Cui, Y.; Bao, Z. A Nickel-Decorated Carbon Flower/Sulfur Cathode for Lean-Electrolyte Lithium-Sulfur Batteries. *Adv. Energy Mater.* **2021**, *11*, 2101449.
- [43] Khani, H.; Wipf, D. O. Iron Oxide Nanosheets and Pulse-Electrodeposited Ni-Co-S Nanoflake Arrays for High-Performance Charge Storage. *ACS Appl. Mater. Interfaces* **2017**, *9*, 6967-6978.
- [44] Wei, S.; Ma, L.; Hendrickson, K. E.; Tu, Z.; Archer, L. A. Metal-Sulfur Battery Cathodes Based on PAN-Sulfur Composites. *J. Am. Chem. Soc.* **2015**, *137*, 12143-12152.
- [45] He, J.; Bhargava, A.; Manthiram, A. High-Energy-Density, Long-Life Lithium-Sulfur Batteries with Practically Necessary Parameters Enabled by Low-Cost Fe-Ni Nanoalloy Catalysts. *ACS Nano* **2021**, *15*, 8583-8591.
- [46] Yang, X.; Luo, J.; Sun, X. Towards high-performance solid-state Li-S batteries: from fundamental understanding to engineering design. *Chem. Soc. Rev.* **2020**, *49*, 2140-2195.
- [47] Lian, Z.; Yang, M.; Jan, F.; Li, B. Machine Learning Derived Blueprint for Rational Design of the Effective Single-Atom Cathode Catalyst of the Lithium-Sulfur Battery. *J. Phys. Chem. Lett.* **2021**, *12*, 7053-7059.
- [48] Gao, X.; Sun, Q.; Yang, X.; Liang, J.; Koo, A.; Li, W.; Liang, J.; Wang, J.; Li, R.; Holness, F. B.; Price, A. D.; Yang, S.; Sham, T.-K.; Sun, X. Toward a remarkable Li-S battery via 3D printing. *Nano Energy* **2019**, *56*, 595-603.
- [49] Zhou, G.; Tian, H.; Jin, Y.; Tao, X.; Liu, B.; Zhang, R.; Seh, Z. W.; Zhuo, D.; Liu, Y.; Sun, J.; Zhao, J.; Zu, C.; Wu, D. S.; Zhang, Q.; Cui, Y. Catalytic oxidation of Li₂S on the surface of metal sulfides for Li-S batteries. *Proc. Natl. Acad. Sci. U.S.A.* **2017**, *114*, 840-845.
- [50] Yang, Y.; Wang, Y.; Xia, Y.; Huo, F.; He, H. Balancing Anchoring and Diffusion for Screening of Metal Oxide Cathode Materials in Lithium-Sulfur Batteries. *J. Phys. Chem. C* **2021**, *125*, 24318-24327.
- [51] Kim, J.; Shin, H.; Yoo, D.-J.; Kang, S.; Chung, S.-Y.; Char, K.; Choi, J. W. Cobalt(II)-Centered Fluorinated Phthalocyanine-Sulfur S_NAr Chemistry for Robust Lithium-Sulfur Batteries with Superior Conversion Kinetics. *Adv. Funct. Mater.* **2021**, *31*, 2106679.

- [52] Kumar, S.; Krishnamoorthy, K. Concurrent Polyvalent Interaction and Electrocatalysis to Improve Lithium-Sulfur Battery Performance. *Batteries & Supercaps* **2021**, *5*, e202100229.
- [53] Sanchez-Sanchez, A.; Izquierdo, M. T.; Mathieu, S.; Ghanbaja, J.; Celzard, A.; Fierro, V. Structure and electrochemical properties of carbon nanostructures derived from nickel(II) and iron(II) phthalocyanines. *J. Adv. Res.* **2020**, *22*, 85-97.
- [54] Robertson, J. M.; Woodward, I. An X-ray study of the phthalocyanines. Part III. Quantitative structure determination of nickel phthalocyanine. *J. Chem. Soc.* **1937**, 219-230.
- [55] Xiao, Y.; Zhang, M.-R.; Li, J.-J.; Pan, G.-B. Fabrication of nickel phthalocyanine free-standing film on ionic liquid surface and photoelectrical response. *Chem. Phys. Lett.* **2017**, *687*, 317-321.

Chapter 5

5 Summary and Future Directions

5.1 Summary

Graphene-based materials are versatile for energy storage systems. In chapter 1, discussed the significance and working principles of Li-S batteries. The factors of challenges in the systems. A detailed description had given of the components of Li-S batteries and reviewed the development achieved in the cathode part in the last decade. The types of Sulfur hosts developed to dates, such as carbon-based materials, inorganic composites (metal and metal oxides), organic frameworks, MXenes, and polymer materials, are discussed in detail. The other battery components, such as binder, anode, electrolytes, additives, and separator, are discussed in this chapter.

In chapter 2, we attempted the heteroatom(s) graphene materials as Sulfur hosts for Li-S batteries. The ball-milling approach was used to synthesize the few-layer graphene layers from pristine graphite. The melamine, 3-Thiopheneacetic acid, and Ni-Phthalocyanine were used as an intercalator. Anthracene was used for control experiments. In case of Ni-Phthalocyanine, we could obtain approximately four-layer graphenes'. Then, these graphenes were thermally treated to obtain the doped layer comprising Graphenes' (DLC-G). The elemental Sulfur was incorporated into these materials via a wet chemical process using Triton-X-100 as a surfactant. We could achieve a Sulfur loading of 86-90 % for all the materials. The G-NP comprised electrodes were delivered the 1218 mAh/g at the initial cycle and 748 mAh/g at the five hundredth cycle. Among all, G-NP based batteries exhibited tremendous energy and power densities. It is due to the presence of Ni cation and pyridinic nitrogen. The electrocatalytic activity of all the DLC-Gs were examined by polysulfide adsorption test and cyclic voltammogram of symmetric cells.

In third chapter, Graphene supported metal ions (Ni^{2+} or Co^{2+}) were designed and synthesized using the ball-milling method. The NiSO_4 and CoCl_2 served as exfoliators and the source for metal ions. These metal ions decorated Graphenes were examined for polysulfide adsorption studies and found that the G-Ni effectively attracted the polysulfide as compared to G-Co. The Sulfur loading was carried out via the melt diffusion method and obtained 62.8 % and 69.1 % for G-Co, and G-Ni, respectively. The G-Ni comprised Li-S batteries demonstrated the maximum specific capacity of 1022 mAh/g. Further, 91 % and 57 % retained capacity were observed at the hundredth and five hundredth cycles. We have proved that the Ni cation decorated Graphene effectively electrocatalyzed the sluggish Sulfur redox reactions and alleviated the polysulfide shuttle mechanisms.

In chapter 4, we chose the Metal-Phthalocyanines (Fe-Phthalocyanine, Co-Phthalocyanine, and Ni-Phthalocyanine), which were successfully carbonized to achieve the metal-decorated carbons. The Sulfur encapsulation was carried out for these samples through the melt-diffusion method, acquiring the 69.0 %, 73.2 %, and 78.1 % for Fe-Ph, Co-Ph, and Ni-Ph samples, respectively. Followed by, the Li-S cells were fabricated using these M-Phs and examined for cyclic voltammetry techniques. We observed the distinguish two reduction and two oxidation peaks for Co-Ph, and Ni-Ph comprised cells, while Fe-Ph based cells showed a single oxidation peak. It indicated the improved kinetics for the sluggish redox reactions and improved the utilization of active materials. Also, noticed that the Ni-Ph based cells exhibited the highest peak current density as compared to other M-Ph comprised systems. Also, it delivered the specific capacity of 1067 mAh/g at the initial cycle and 939 mAh/g (78.4 % of retention capacity) at the hundredth cycle.

5.2 Future Directions

In this thesis work, we have developed heteroatom(s) and/or transition metal or metal ion decorated materials as hosts for elemental Sulfur. In all the cases, Nickel illustrated materials exhibited better capacity with improved cycle life due to the electrocatalytic as well as potential towards the efficient withholding of the polysulfides. Furthermore, these soluble polysulfides also could arrest at the separator by modifying it. The monolayer polypropylene (Celgard 2400 type) separator contains a uniform micropore structure. The thickness of the Celgard 2400 separator is 25 μm , and the calculated porosity is 41 %. This membrane is known for better Li^+ ion transportation, which helps in Li-ion batteries. Unfortunately, in Li-S battery systems, the formed intermediates migrate toward the anode compartment with ease and lead to the permanent loss of active materials. Therefore, the separator modification is imperative. However, the LiPSs are negatively charge-bearing species; the metal-based materials could serve to attract the polysulfides, which are leach out from the cathode compartment. The Nickel, Palladium, Zinc, and other transition metals decorated materials could be used to modify the PP separator, and it would be a potential candidate to further suppress the polysulfide dissolutions.

ABSTRACT

Name of the Student: Kumar S**Registration No.: 10CC15J26019****Faculty of Study: Chemical Sciences****Year of Submission: 2022****AcSIR Academic Centre/CSIR Lab:
CSIR-National Chemical Laboratory****Name of the Supervisor(s):
Dr. K. Krishnamoorthy****Title of the thesis: Heteroatom Doped Materials for Li-S Battery Applications**

Li-S batteries have a great attraction due to its theoretical specific capacity of 1675 mAh g⁻¹ and energy density up to 2600 Wh kg⁻¹ are attractive energy storage devices. Overall, this thesis contains five chapters. The contents of the chapters are briefly highlighted in below. **Chapter 1** of this thesis focuses on overview of Li-S batteries. The working principles and challenges are explained in details. The components of Li-S batteries, especially the developments on cathode materials are discussed. **Chapter 2** deals with graphene with doped layer to electrocatalyze the sluggish sulfur redox reaction. The doped layer comprises heteroatoms such as either N or N and S. The doped layer also comprises cations of Ni. We have chosen a "doped layer on Graphene" over "doped Graphene" to avoid defects in the basal plane of graphene. We found the doped layer comprising Graphene (DLC-G) to electrocatalyze the polysulfide redox reaction. We found that cations in the layer electrostatically attract the polysulfides due to the polyvalent interaction. While using this material in the Li-S batteries, the specific capacity, energy density and power density were found to be 1345 mAh g⁻¹, 782 Wh kg⁻¹ and 4437 W kg⁻¹, respectively. **Chapter 3** deals with Nickel cations with other heteroatoms as a host in Li-S batteries. However, metal salts can either exhibit monovalent or divalent attraction with polysulfides. Those interactions are weak and we must have polyvalent interaction. Towards this objective, we have designed and synthesized a material that comprises multiple divalent cations that is also devoid of heteroatoms. The material was prepared by ball-milling Graphite in presence of either nickel sulfate or cobalt chloride. The Li-S batteries showed a maximum specific capacity of 1022 mAh/g. Among the metal cations, nickel cations showed better performance than cobalt cations. Thus, we demonstrate that metal cations immobilized on Graphene can efficiently electrocatalyze sluggish sulfur redox reaction and suppress the polysulfide dissolution. **Chapter 4** deals with the investigation of the carbonized Transition metal-phthalocyanine as a host for elemental Sulfur. Due to presence of different metals (M=Fe, Co and Ni) on the carbonized phthalocyanine. Among all M-Phs, Nickel based material exhibited the best electrochemical reversibility of polysulfide conversion reactions with better kinetics. The Ni-Ph/S cells exhibited a remarkably high specific capacity of 939 mAh/g at hundredth cycle, while others delivered poor efficacies. **Chapter 5** deals the key results of the all chapters. It also provides a concise summary of major findings of the work that has been presented in the thesis and future directions to achieve the better performances for Li-S cells.

Details of the publications emanating out of the thesis work

1. Kumar, S.; Krishnamoorthy, K., Concurrent Polyvalent Interaction and Electrocatalysis to Improve Lithium-Sulfur Battery Performance. *Batteries & Supercaps* 2021, 5, e202100229.

List of Poster presentation with abstract:

1. Poster presentation in MACRO Meet-2018, SPSI MACRO International Conference on Polymer Science and Technology, 19th-22nd December 2018, organized by IISER-Pune. Received the best poster award.

Topic: Conjugated Small Organic Molecules for Li-Ion Batteries

Abstract: The Lithium-ion batteries based on Organic molecules are attractive due to the possibility of fabricating lightweight batteries with high energy and power density, long life and environmental friendliness for mobile applications and flexible devices. However, the organic lithium batteries have high capacity and large serial-parallel numbers which coupled with such problems as safety, durability and cost. Often, the experimental specific capacity is very low during charging and discharging process as compared to theoretical capacity while discharging the battery at moderate and high C rates. To prevent this problem, we designed as many as maximum active sites with Perylene based small conjugated organic molecule. The fabricated Li-ion battery using Perylene hexa lithium salt exhibits 100% coulombic efficiency and specific capacity while discharging at 5 C. The control experiments confirm our hypothesis of using the maximum number of active sites in smaller organic molecule improve the performance of organic lithium battery.

2. Poster presentation Poster presentation in Innovation & Entrepreneurship: Role of Science & Technology, 31st January-2nd February 2019, organized by Humboldt Academy

Topic: N, S-rich carbon skin for Li S battery application

Abstract: The Batteries comprising Sulfur and Lithium has high theoretical capacity. However, the performance of Li-S battery is not impressive due to several issues such as (i) sluggish redox of polysulfide, (ii) dissolution of polysulfide in electrolyte and (iii)

crossover of sulfur complexes to the lithium electrode. To circumvent these issues, we report a rationally designed cathode material based on graphene. The modified graphene render the possibility of very high sulfur loading (87 wt%). The cathode exhibits high initial specific capacity of 900 mAh/g at 2C rate with insignificant decay even after 100 cycles. The battery exhibits a specific capacity of 650 mAh/g at 5C rate with ~95% Coulombic efficiency. Control experiments indicate that N and S comprising skin is essential to improve the battery performance.

3. Poster presentation in MACRO Meet-2022, SPSI MACRO International Conference on Polymer Science and Technology, 2nd-4th November 2022, organized by NCL-Pune.

Topic: Concurrent Polyvalent Interaction and Electrocatalysis to Improve Lithium-Sulfur Battery Performance

Abstract: Batteries with improved efficiency are desired. Li S batteries are attractive due to their high specific capacity and energy density. However, sluggish sulfur redox reaction and polysulfide dissolution are significant challenges in Li S batteries. In this work, we report graphene with doped layer to electrocatalyze the sluggish sulfur redox reaction. The doped layer comprises heteroatoms such as either N or N and S. The doped layer also comprises cations of Ni. We have chosen a “doped layer on graphene” over “doped graphene” to avoid defects in the basal plane of graphene. We found the doped layer comprising graphene (DLC G) to electrocatalyze the polysulfide redox reaction. However, the interaction between the doped layer and polysulfide is still weak, hence the dissolution is not suppressed. To circumvent the polysulfide dissolution, graphene with cationic layer was prepared. We found that cations in the layer electrostatically attract the polysulfides due to the polyvalent interaction. Thus, the dissolution is suppressed. While using this material in the Li S batteries, the specific capacity, energy density and power density were found to be 1345 mAh g⁻¹, 782 Wh kg⁻¹ and 4437 W kg⁻¹, respectively.

Concurrent Polyvalent Interaction and Electrocatalysis to Improve Lithium-Sulfur Battery Performance

Subramani Kumar (சுப்பிரமணி குமார்)^[a, b] and Kothandam Krishnamoorthy (கோதண்டம் கிருஷ்ணமூர்த்தி)^{*[a, b]}

Dedicated to Dr. S. Sivaram on the occasion of his 75th birthday.

Batteries with improved efficiency are desired. Li–S batteries are attractive due to their high specific capacity and energy density. However, sluggish sulfur redox reaction and polysulfide dissolution are significant challenges in Li–S batteries. In this work, we report graphene with doped layer to electrocatalyze the sluggish sulfur redox reaction. The doped layer comprises heteroatoms such as either N or N and S. The doped layer also comprises cations of Ni. We have chosen a “doped layer on graphene” over “doped graphene” to avoid defects in the basal plane of graphene. We found the doped layer comprising

graphene (DLC–G) to electrocatalyze the polysulfide redox reaction. However, the interaction between the doped layer and polysulfide is still weak, hence the dissolution is not suppressed. To circumvent the polysulfide dissolution, graphene with cationic layer was prepared. We found that cations in the layer electrostatically attract the polysulfides due to the polyvalent interaction. Thus, the dissolution is suppressed. While using this material in the Li–S batteries, the specific capacity, energy density and power density were found to be 1345 mAh g⁻¹, 782 Wh kg⁻¹ and 4437 W kg⁻¹, respectively.

1. Introduction

Battery systems with significantly improved energy and power density over the existing lithium-ion batteries are of great interest. Li–S batteries with a theoretical specific capacity of 1675 mAh g⁻¹ and energy density up to 2600 Wh kg⁻¹ are attractive energy storage devices.^[1,2] Despite the promise, Li–S batteries are plagued with issues such as poor electrical conductivity of sulfur (5 × 10⁻³⁰ S cm⁻¹), sluggish sulfur redox reaction and dissolution of polysulfide in the battery electrolyte.^[3] The poor electrical conductivity issue is tackled by preparing carbon composite electrodes.^[4] The sluggish redox reaction and dissolution of polysulfide remain as challenges.^[5] The two major approaches to circumvent the dissolution of polysulfide, which is commonly known as the shuttle effect can be classified into, i) membrane modification and ii) electrode modification. First, the separator membranes are modified with carbon allotropes, polymers and nanostructures. The modified membranes repel the polysulfides and suppress the deleterious shuttle effect.^[6,7] In the second approach, porous structures of organic and inorganic materials have been used to confine the sulfur. The pores that are used to load the sulfur also render

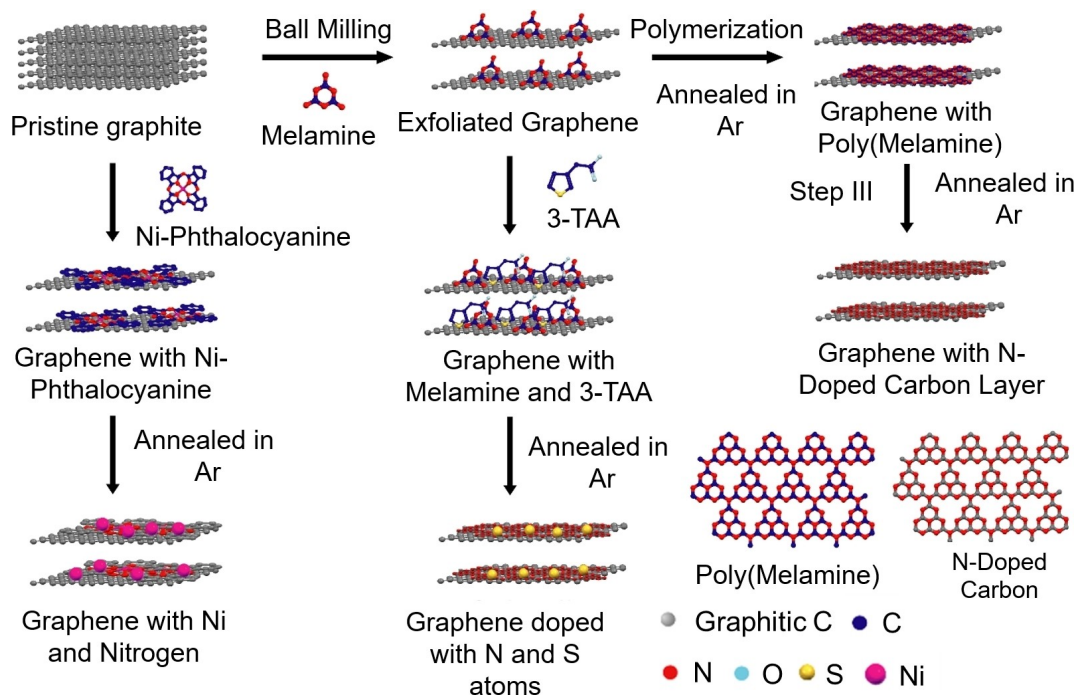
the possibility of diffusion of polysulfides from the confining material.^[8] Thus, the confinement approach has its limitations. Li–S battery metrics of various materials are summarized in Table S1 (Supporting Information).

Usually, the battery electrode is prepared by blending sulfur, polymer binder and conducting carbon.^[6] Neither the conducting carbon nor the binder is effective in suppressing the polysulfide dissolution.^[9] Thus, an additive is required. The additive should be a material with properties to withhold the polysulfide from dissolving in the electrolyte. With its excellent properties and easy synthesis, graphene seems to be an attractive candidate.^[10] However, the surface of graphene is hydrophobic; hence it is not suitable to withhold polysulfide.^[11] Therefore, modification of graphene is required. Doped graphene is an option.^[12] It has been used as an additive in the Li–S battery electrodes. All the doped graphene do not have the desired effect. For example, pyridinic and graphitic nitrogen comprising graphenes are better electrocatalysts than pyrrolic nitrogen-containing graphene.^[13] The pyridinic and pyrrolic nitrogens are Lewis base and they can attract Lewis acid such as polysulfides. However, it has been shown that the pyridinic nitrogens are present either on the edges or at the defect sites of graphene, which is a limitation. Thus, an approach that renders the possibility of preparing graphene without defect but with pyridinic and graphitic nitrogen is required. To accomplish this paradoxical objective, we resorted to an approach that mechanically peels off graphene from graphite in presence of exfoliator. The exfoliator molecules that adhere to the graphene surface have been judiciously chosen to have desired dopant atoms. The graphene preparation approach is mechanical; hence the graphene's basal plane is unaffected.^[14–16] In the first set of experiments, melamine (Scheme 1) was used as exfoliator. Graphite and melamine are

[a] S. Kumar (சுப்பிரமணி குமார்), Dr. K. Krishnamoorthy (கோதண்டம் கிருஷ்ணமூர்த்தி)
Polymer Science and Engineering Division
CSIR-National Chemical Laboratory
Pashan Road, Pune 411008, India

[b] S. Kumar (சுப்பிரமணி குமார்), Dr. K. Krishnamoorthy (கோதண்டம் கிருஷ்ணமூர்த்தி)
Academy of Scientific and Innovative Research
Kamla Nehru Nagar, Ghaziabad 201002, India
E-mail: k.krishnamoorthy@ncl.res.in

Supporting information for this article is available on the WWW under <https://doi.org/10.1002/batt.202100229>



Scheme 1. Cartoon showing the steps involved in the preparation of DLC-G.

ball-milled in planetary ball milling equipment. After exfoliation, the samples were subjected to thermal treatment. During this process, melamine undergoes thermal polymerization leading to a cross-linked polymer that can act as a source of nitrogen-doped carbon.^[17] Upon further heating, we envisioned graphenes with a layer comprising pyridinic and graphitic nitrogen (Scheme 1). We reiterate that a minimal amount of defects are anticipated in the basal plan of graphene because the exfoliation is mechanical. Dual doping can enhance electrocatalysis,^[18] hence we prepared graphene with layers comprising S and N atoms. These modified graphene samples are expected to electrocatalyze the sluggish polysulfide redox reaction.^[19] We understand that the N and S comprising graphene layer alter the surface properties, but the interaction between polysulfide and graphene is weak. The sulfur undergoes various structural changes; hence covalent immobilization is not an option. Therefore, we need to rely on non-covalent, yet strong interaction. The negative charges on polysulfide render the possibility to anchor them on the surface of graphene non-covalently. In order to achieve this objective, we must prepare graphene layer with positive charges. Our approach, mechanical exfoliation, renders the possibility of embedding cations on the layer of graphene. To embed cations on the layer of graphene, graphite was ball milled with Nickel Phthalocyanine (Scheme 1). During the milling process, Nickel Phthalocyanine molecules adhere to the surface of graphene. Subsequent heating of the sample resulted in the formation of graphene with a carbon layer comprising nickel ions and nitrogen. The nitrogen-doped carbon layer is expected to catalyze the sulfur redox reaction,^[20] concurrently the nickel ions are expected to suppress polysulfide dissolution due to electrostatic polyvalent interaction.^[21] Various interactions have

been used to suppress polysulfide dissolution in Li-S batteries. Electrostatic polyvalent interaction, which is a very strong interaction hasn't been used in Li-S batteries. Probably due to the difficulty in using cations that can have polyvalent electrostatic attractions with polysulfide. Herein, we report a method to immobilize cations on graphene that interact with polysulfide due to polyvalent electrostatic attraction. Indeed, the Ni cation and N containing carbon layer based graphene exhibits superior battery performance that is reported in this research work.

2. Results and Discussion

Graphite was ball milled with melamine (exfoliator) at various revolutions per minute (RPM). We also varied the duration of the ball milling. In another set of experiments, anthracene (control molecule, Scheme 1) was used as an exfoliator (Table S2, Supporting Information). Anthracene has been chosen as a control molecule due to the absence of heteroatoms. After the ball milling, the samples were washed with a copious amount of DMF to remove excess exfoliators. The results and discussions are divided into four sections. First, we discuss the characterization of graphene with an exfoliator. In the next section, the preparation and characterization of DLC-G are discussed. Subsequently, battery fabrication and testing are discussed. In the fourth section, we will discuss the preparation and characterization of DLC-G with Ni ions and battery performance using the same material. After ball milling and washing, the samples were subjected to Raman spectroscopic analysis. Intense G and 2D bands appeared at 1581 and 2676 cm^{-1} , respectively (Figure 1a). D band appeared at

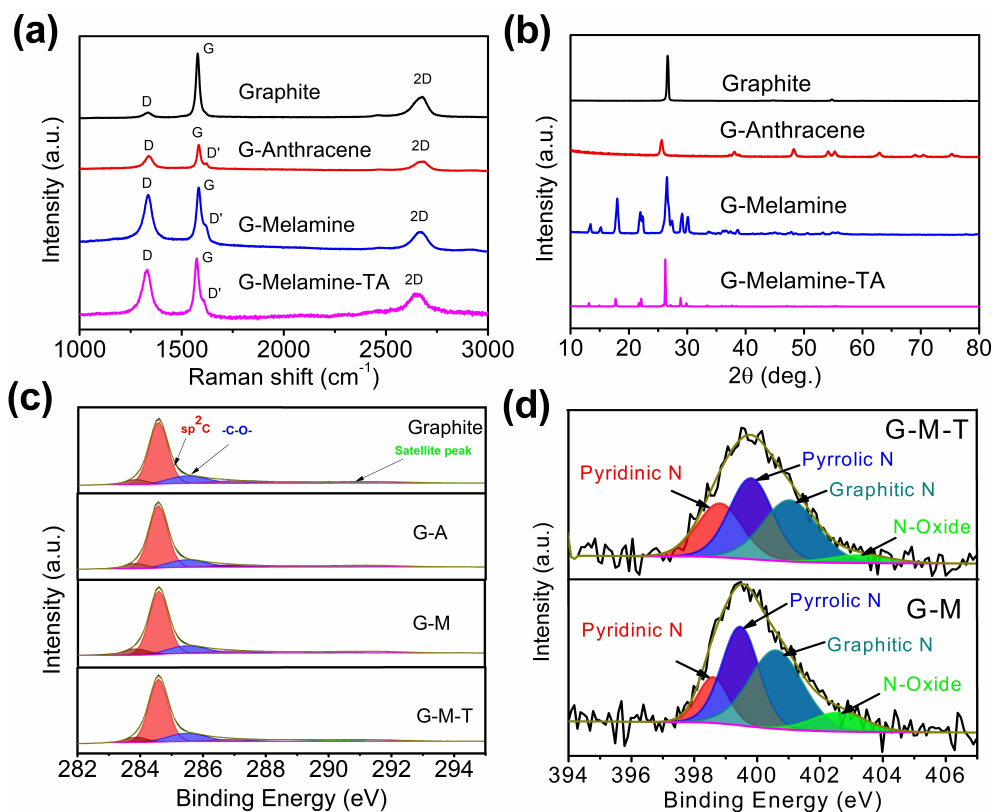


Figure 1. Raman spectra showing D, D', G and 2D bands of exfoliated graphene (a) and XRD pattern of exfoliated graphene (b). XPS spectra of pristine graphite, few-layer graphene G-A, G-M and G-M-T (c) and deconvoluted peaks of the nitrogen region for G-M and G-M-T (d).

1335 cm⁻¹ and D' shoulder appeared at 1616 cm⁻¹. The intensity of D and G bands (I_D/I_G) ratio provides information about the graphene layers.^[14,22] High I_D/I_G value is an indication of fewer layer graphenes. The highest I_D/I_G of 0.90 was found while melamine was used as exfoliator with RPM of 200. The duration of the milling was 60 min. All the parameters used for milling and the properties of resultant materials are listed in Table S2. The I_D/I_D' provides information about defects in the graphene. I_D/I_D' of 3.5 or lower indicates edge and boundary defects with no SP³ defects.^[23] All the samples showed I_D/I_D' less than 3.5 indicating the formation of high-quality graphene while using melamine and anthracene as exfoliators (Table S2). The samples were subjected to XRD analysis, which is an effective method to identify the formation of graphene from graphite through the mechanical exfoliation process. Graphene shows an intense peak at 2θ of 26.6° that corresponds to 002 plane (Figure 1b).^[15] The d-spacing for graphite was found to be 3.347 Å, which increased to 3.377 Å while using melamine as an exfoliator. This was further increased to 3.384 Å while using anthracene as an exfoliator. Thus, the exfoliators increase the distance between the layers of graphene. With this information in hand, we proceeded to synthesize DLC-G. The exfoliated graphene was heated at 600 °C in an inert atmosphere. Henceforth, the graphene prepared with anthracene as an exfoliator will be mentioned as G-A. The graphene prepared using melamine as an exfoliator will be mentioned as G-M. The G-M comprises nitrogen atoms in the layer. To prepare N and S

comprising DLC-G, the melamine exfoliated graphene was treated with 3-thiophene acetic acid (TAA) (Scheme 1). The carboxylic acid functionality of TAA interacts with pyridinic and amine moieties of melamine. Thermal treatment of this sample is envisioned to yield N and S comprising DLC-G. This sample will be mentioned as G-M-T in all the forthcoming discussions.

After heating, the samples were subjected to XPS analysis. The XPS spectra of graphite showed the presence of sp² C (284.6 eV) (Figure 1c). We also found a peak corresponding to -C-O- (285.6 eV) (Figure 1c). The small peak at 283.8 eV is due to disorder carbon.^[24] The G-A also showed these peaks indicating the absence of any new heteroatoms due to the lack of them in anthracene. The XPS spectra of G-M showed N1s peak at 399 eV and other characteristic peaks found for G-A. The G-M-T showed a peak at 165 eV that is characteristic of -C=S-C- moieties (Supporting Information, Figure S1). These experiments have proven that the DLC-G with various dopants can be synthesized by changing the exfoliator molecules. As mentioned in the introduction section, three types of nitrogens are present in doped graphenes. We anticipate those in the DLC-G. In the case of G-M, the pyridinic nitrogen is lowest at 24.8%, and the pyrrolic nitrogen is highest at 36.1% (Figure 1d). In the case of G-M-T, the graphitic nitrogen is highest at 40.9%, and the pyridinic nitrogen is 13.5%. The high graphitic nitrogen in G-M-T may lead to better electrocatalytic activity. Atomic mapping was carried out to corroborate the presence of heteroatoms in the samples. The G-A samples

showed the presence of carbon throughout the sample (Supporting Information, Figure S2). In the case of G–M, carbon and nitrogen were also present and they are distributed uniformly throughout the sample (Supporting Information, Figure S3). We noticed the presence of sulfur in the samples of G–M–T (Supporting Information, Figure S4). The TEM images showed a clear difference in morphology between the graphite and graphene. The graphite comprises about 80 layers of graphene (Supporting Information, Figure S5). About ten and five layers are found in G–M (Figure 2a) and G–M–T (Figure 2b), respectively. TEM imaging was carried out for samples blended with sulfur. The sulfur loading did make the graphene opaque (Figure 2c). The opaqueness is due to the presence of a large amount of sulfur along with DLC–G. We hypothesized that the DLC–G would withhold sulfur better than that of graphite. To test this hypothesis, the samples were subjected to TGA analysis. The sulfur loading was 85.8% while sulfur was blended with G–A. It increased to 87.2% and 89.5% for G–M and G–M–T, respectively (Figure 2d). Thus, the doped layer on the DLC–G increased the sulfur loading. We also carried out polysulfide adsorption experiment to find out the interaction between DLC–G and polysulfides. A 5 mM Li_2S_6 was prepared by following the reported procedure.^[25] In that solution, an internal standard diketopyrrolopyrrole (DPP) was added. From the stock solution, 5 mL was distributed into various glass vials. To that solution, 5 mg of DLC–G was added and the solution was left quiescent for 12 hrs. The color of the solution with G–A didn't vary significantly, indicating the weak interaction between polysulfide and G–A. To quantify the interaction, an aliquot was taken to record UV-vis absorption spectra. The Li_2S_6 solution

showed three peaks at 263, 281 and 338 nm. The solution with DPP (internal standard) showed two additional peaks at 510 and 547 nm. The UV-vis absorption spectra of the aliquot solution are shown in Figure 2e. The absorption maxima decreased in the following order G–A > G–M > G–M–T. This trend indicates that the G–A has weak and G–M–T has strong interaction with polysulfides. In case of G–A, there is no specific interaction between the hydrophobic surface of G–A and negative charge bearing polysulfides. On the other hand, polysulfide interacts with G–M due to Lewis acid base interaction. In case of G–M–T, Lewis acid base interaction and sulfur sulfur interaction is in operation. Due to the strong interaction, polysulfide adhered well on to the surface of G–M–T. This experiment corroborates our hypothesis that the layer with heteroatom increases the interaction between polysulfide and graphene. With this information in hand, we proceeded to fabricate Li–S batteries. The cells were used to record cyclic voltammetry between 3 and 1.5 V vs. Li^+/Li . The first peak appeared at 2.3 V, which corresponds to the conversion of S_8 to Li_2S_n ($4 < n \leq 8$).^[11] Subsequently, conversion of Li_2S_n to $\text{Li}_2\text{S}_2/\text{Li}_2\text{S}$ occurred at 2 V. In the reverse sweep, conversion of Li_2S to S_8 occurred at 2.4 V (Figure 3a).^[26] These are typical peaks observed in Li–S batteries. It is worth noting the variation in peak current intensity (i_p) as a function of cycle number. At the end of the 5th cycle, the i_p decreased by 25% while using G–A. The corresponding change was 10% while using G–M as electrode. Based on this trend, we anticipated a lower change while using G–M–T as electrode. Contrary to this expectation, the decrease was 29%, which is the highest among the DLC–G. This indicates that the polysulfide dissolution has increased

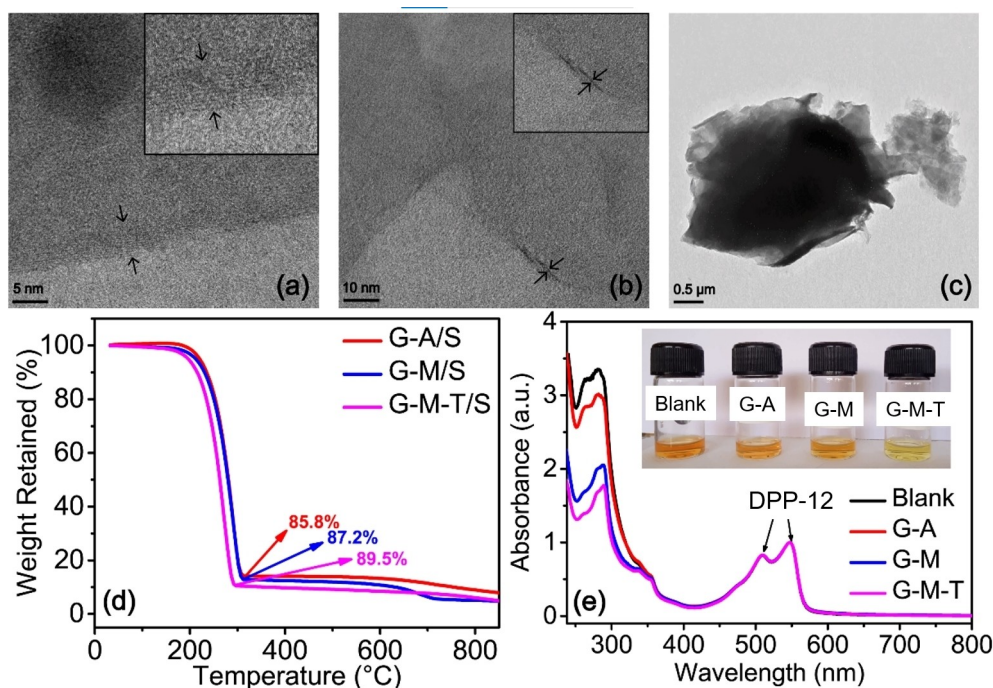


Figure 2. TEM images showing the few layers of graphene G–M (a) and G–M–T (b). TEM image of sulfur loaded G–M–T (c). TGA indicating the sulfur loading in G–A, G–M and G–M–T (d). UV-Vis spectra of Li_2S_6 solution in presence and absence of DLC–Gs (e). The insert is the photograph of Li_2S_6 solution in presence of DLC–Gs.

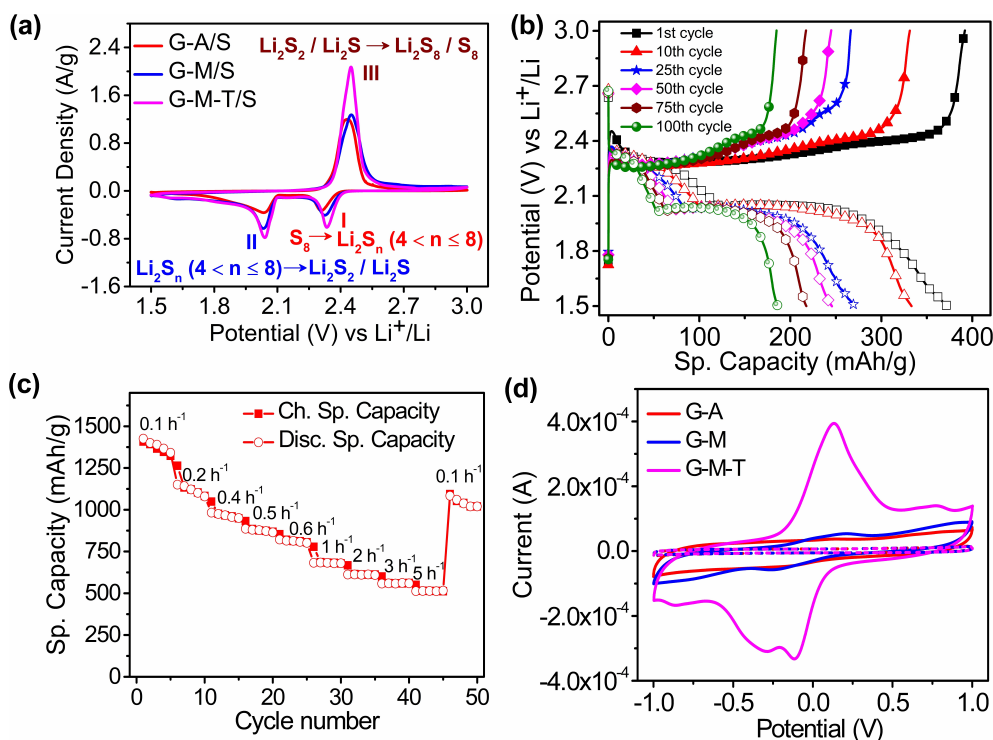


Figure 3. Cyclic voltammogram of Li-S battery comprising various DLC-Gat a scan rate of 0.1 mVs^{-1} (a). Charge-discharge curves at 0.2 h^{-1} , showing specific capacity fading while using G-A in Li-S battery electrode (b). Rate performance study of G-M-T based Li-S battery (c). Plot showing the cyclic voltammograms of symmetric cells with various DLC-G(d)

while the electrodes are prepared with G-M-T. Although the absorption studies (Figure 2e) indicate strong interaction between G-M-T and polysulfides in quiescent solution, the polysulfide dissolution is not suppressed during potential sweep. The i_p was found to be $1.08 \times 10^{-3} \text{ mA}$ for G-A, which increased to $1.15 \times 10^{-3} \text{ mA}$ for G-M and increased further to $1.87 \times 10^{-3} \text{ mA}$ for G-M-T. The significant increase in i_p of sulfur redox in G-M-T based electrodes is an indication of electrocatalysis. The batteries fabricated using DLC-G were subjected to charge-discharge experiments. The experiments were carried out between 1.5 and 3 V vs. Li^+/Li . The discharge curve showed two plateaus corresponding to the following reactions, $\text{S}_8 \rightarrow \text{Li}_2\text{S}_n (4 < n \leq 8)$, $\text{Li}_2\text{S}_n (4 < n \leq 8) \rightarrow \text{Li}_2\text{S}_2/\text{Li}_2\text{S}$ at 2.3 and 2.0 V, respectively.^[1] The reactions corresponding to various regions of the curve are shown in Figure 3a. The specific capacity of the first cycle of the battery with G-A was 372 mAh g^{-1} (0.2 h^{-1}) (Figure 3b). Please note that the specific capacity is a mere 22% of theoretical capacity (1675 mAh g^{-1}). This decreased to 186 mAh g^{-1} at 100th cycle, decreasing 54% compared to the first cycle. A similar decrease in specific capacity as a function of hundred charge-discharge cycles was observed for other C rates. The reduction in specific capacity compared to the first charge-discharge cycle was 35% (1 h^{-1}), 14% (2 h^{-1}) and 44% (5 h^{-1}). These experiments indicate the poor efficacy of DLC-G that is devoid of heteroatoms in Li-S batteries. Furthermore, the polarization of the discharge curve means poor electrocatalysis while using G-A as electrode material. In the case of G-M, the specific capacity of the first cycle was 535 mAh g^{-1} (0.2 h^{-1}), which is 163 mAh g^{-1} higher than that of G-A based

batteries (Supporting Information, Figure S6). We attribute the marginal performance increase to the presence of 24.8% of pyridinic nitrogen in G-M. The decrease in specific capacity as a function of hundred charge-discharge cycling was found to be 42% (311 mAh g^{-1} at 100th cycle). Thus, the performance of G-M (N doped layer comprising graphene) is better than G-A based batteries. The improved performance is attributed to heteroatoms that are present in G-M. At higher C rates, the decrease in specific capacity as a function of hundred charge-discharge cycling was found to be 25% (1 h^{-1}), 14% (2 h^{-1}) and 31% (5 h^{-1}). So far, a battery is subjected to charge-discharge cycling at a particular C rate for hundred cycles. To test a battery's efficacy as a function of various C rates, rate performance studies were conducted. In this experiment, a battery was subjected to charge-discharge cycling at 0.1 h^{-1} and the C rate was gradually increased up to 5 h^{-1} . While increasing the C rate, the specific capacity decreases. At 5 h^{-1} , the specific capacity decreased by 82% compared to 0.1 h^{-1} . This result raises the question, is the massive decrease due to sulfur dissolution? To test this, the battery that was discharged at 5 h^{-1} , was subjected to charge-discharge experiment at 0.1 h^{-1} . In this experiment, the specific capacity bounced back to 634 mAh g^{-1} , which is very close to the specific capacity observed at the start of the experiment (Supporting Information, Figure S7). Please recall the specific capacity at 5 h^{-1} was 124 mAh g^{-1} , which was observed in the previous experiment. Thus, the bounce-back of specific capacity at 0.1 h^{-1} indicates that the polysulfide dissolution is low during charge-discharge experiments, while using G-M.

In the next set of experiments, G–M–T was used to prepare the battery electrodes. The specific capacity of batteries prepared using G–M–T was 1270 mAh g^{-1} , while charge-discharge experiment was carried out at 0.2 h^{-1} (Supporting Information, Figure S8). This value is 898 mAh g^{-1} higher than the control experiment (G–A based batteries). The impressive performance enhancement is attributed to the presence of 40.9% pyridinic nitrogen. The decrease in specific capacity as a function of hundred charge-discharge cycling was found to be 39%. This data indicate the improvement in battery performance imparted by doping the carbon layer with N and S. The rate performance study was conducted by following the procedure adapted for G–M based batteries. At 0.1 h^{-1} , the specific capacity was found to be 1426 mAh g^{-1} . Upon increase in C rate, the specific capacity decreased. The lowest specific capacity of 513 mAh g^{-1} was found at 5 h^{-1} . The decrease is 64%. After the charge-discharge experiments at 5 h^{-1} , the batteries were cycled at 0.1 h^{-1} . The specific capacity was found to be 108 mAh g^{-1} (Figure 3c). This is 75% of the specific capacity observed at the same C rate (0.1 h^{-1}) during the start of the experiment. Thus, the battery didn't recover fully probably due to polysulfide dissolution. Thus, the polysulfide dissolution is higher in case of G–M–T based batteries compared to G–M based batteries. This correlates well with the observation of decrease in peak intensity in cyclic voltammograms of G–M–T based batteries (Figure 3a). To study the electrocatalytic properties of DLC–G based batteries, symmetric cells were fabricated. The working and counter electrodes comprise DLC–G, conducting carbon and binder. The electrolyte comprises Li_2S_6 . The cyclic voltammograms (CV) were recorded between -1 and $+1 \text{ V}$ at a scan rate of 5 mV s^{-1} . The CV of G–A showed extremely weak oxidation (0.11 V) and reduction (-0.11 V) wave. G–M also showed oxidation and reduction waves at 0.24 and -0.24 V , respectively (Figure 3d). This indicate poor electrocatalysis by these two DLC–G. Indeed, the CV of symmetric cells without Li_2S_6 in the electrolyte didn't show oxidation and reduction waves (Figure 3d). Thus, the oxidation and reduction waves in the CV of G–A and G–M based symmetric cells originate from Li_2S_6 . The CV of G–M–T showed a sharp oxidation peak at 0.12 V . This peak corresponds to the conversion of lithium sulfide to lithium polysulfide and sulfur. Two peaks were observed during the reverse scan at -0.12 and -0.29 V . The peak at -0.12 V corresponds to the conversion of Li_2S_6 to short chain lithium polysulfide. The peak at -0.29 V corresponds to the formation of lithium sulfide.^[27]

To test the hypothesis that DLC–G with Nickel ion and N as an efficient electrocatalyst, graphene was prepared by ball milling graphite with Nickel phthalocyanine. The sample was subsequently heated to get DLC–G with Ni ion and N. This sample will be mentioned as G–NP in the forthcoming discussions. The XPS spectra of the sample confirmed the presence of pyridinic nitrogen (38.9%), pyrrolic nitrogen (28.6%) and graphitic nitrogen (32.4%) (Supporting Information, Figure S9). The TEM image showed about five layers of graphene in the samples of G–NP (Figure 4a). The elemental mapping showed Ni ion and N are uniformly distributed throughout the sample (Supporting Information, Figure S10). The G–NP was

blended with sulfur and the sample was subjected to TGA analysis. The sulfur content was found to be 89.4%, which is the highest among DLC–G (Figure 4b). To test whether the G–NP has attractive interaction with polysulfides, 5 mg of G–NP was dropped into the 5 mM solution of Li_2S_6 . The solution was left quiescent for 12 hrs. The solution appeared colorless to the naked eyes indicating that the polysulfide is adhered to the positive charge bearing G–NP. An aliquot was taken to record UV-vis absorption spectra. The absorption peaks corresponding to S_6^{2-} showed the lowest absorption among all the DLC–G (Figure 4c). This corroborates our hypothesis of polyvalent interaction between the Ni cations of G–NP with that of polysulfides. In order to study the electrocatalysis of DLC–G, symmetric cells were fabricated. In these cells, the working and counter electrodes are prepared with same material. The cyclic voltammograms were recorded at a scan rate of 5 mV s^{-1} . In case G–NP based symmetric cells, two well defined oxidation and reduction peaks were observed (Figure 4d). The first oxidation peak centered at 0.09 V , indicates the oxidation of Li_2S to Li_2S_6 and the second oxidation peak at 0.25 V is due to the conversion of Li_2S_6 to sulfur. The two reduction peaks observed at -0.09 and -0.25 V are due to conversion of sulfur to Li_2S_6 and Li_2S_6 to Li_2S (Figure 4d).^[27,28] From these experiments, we can conclude that the G–NP is an efficient electrocatalyst. The batteries were fabricated using G–NP following the procedure used for other materials in this work. The cyclic voltammetry of the batteries fabricated using G–NP, sulfur, binder and conducting carbon showed typical redox peaks expected of sulfur. The decrease in peak current intensity (i_p) after five cycles is 5.8% (Supporting Information, Figure S11). This i_p decrease is the lowest among all the DLC–G studied in this work. The absorption solution studies and cyclic voltammetry studies of batteries confirm the suppression of polysulfide dissolution due to polyvalent electrostatic attraction between G–NP and polysulfides. The sharp peaks at 2.43 V in the cyclic voltammogram also indicates the electrocatalytic property of G–NP. The electrocatalytic activity is attributed to the presence of high percentage of pyridinic (38.9%) and graphitic nitrogen (32.4%). In the charge-discharge experiment, the specific capacity at the first cycle was 1345 mAh g^{-1} (0.2 h^{-1}). This specific capacity is 80% of theoretical maximum (Figure 5a). At the 100th cycle, the specific capacity decreased to 1084 mAh g^{-1} . The decrease is mere 20%. Unlike other DLC–G, the specific capacity of the first cycle remained above 1000 mAh g^{-1} at high C rates such as 2 h^{-1} (1218 mAh g^{-1}). Furthermore, the decrease in specific capacity as a function of hundred charge-discharge cycles varied as follows, 13% (0.5 h^{-1}), 21% (1 h^{-1}), 20% (2 h^{-1}), 7% (5 h^{-1}). The lowest specific capacity of 815 mAh g^{-1} was found for batteries cycled at 5 h^{-1} . This impressive performance is due to polyvalent attraction between Ni ions on the layer of graphene with polysulfide. Please note that the discharge curves don't show any polarization due to electrocatalysis and suppressed dissolution of polysulfide. To further test the efficacy of batteries comprising G–NP, rate performance experiments were conducted. The specific capacity was 1279 mAh g^{-1} (0.1 h^{-1}) at the start of the experiment, which decreased to 324 mAh g^{-1}

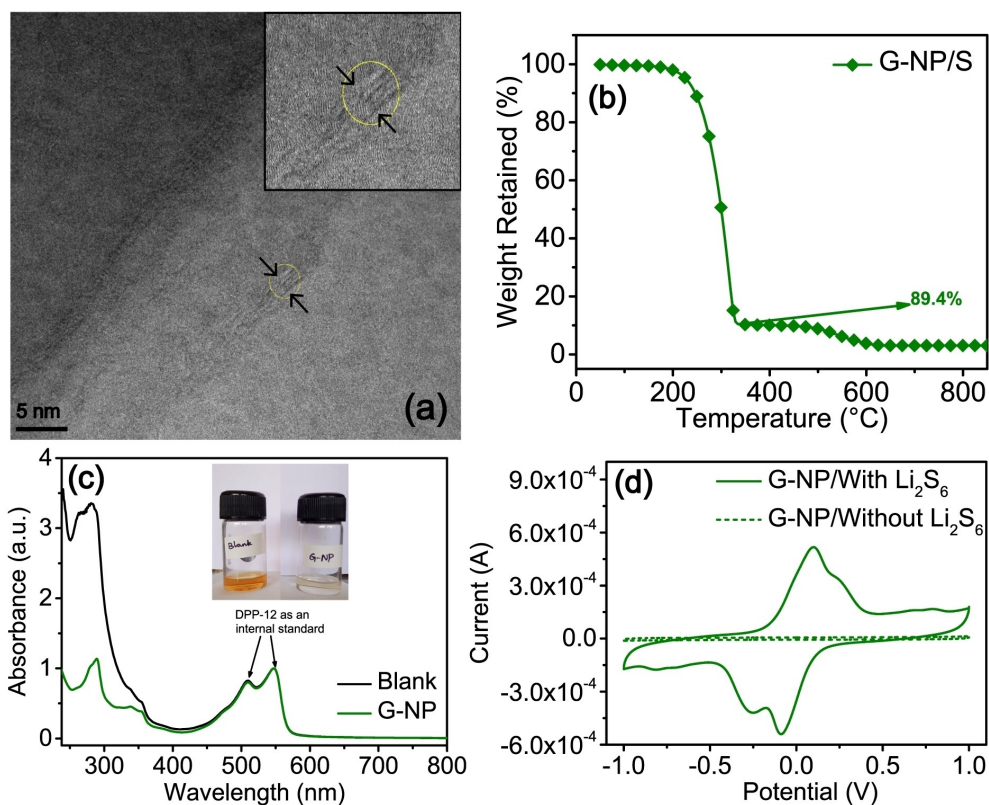


Figure 4. TEM image of G-NP showing few layer graphene (a). Thermogram of sulfur loaded G-NP (b). UV-vis absorption spectra of Li₂S₆ in presence and absence of G-NP. The insert shows colorless solution due to adherence of Li₂S₆ on G-NP. The yellow color solution doesn't comprise G-NP (c). Cyclic voltammogram of symmetric cells comprising G-NP with and without Li₂S₆ (d).

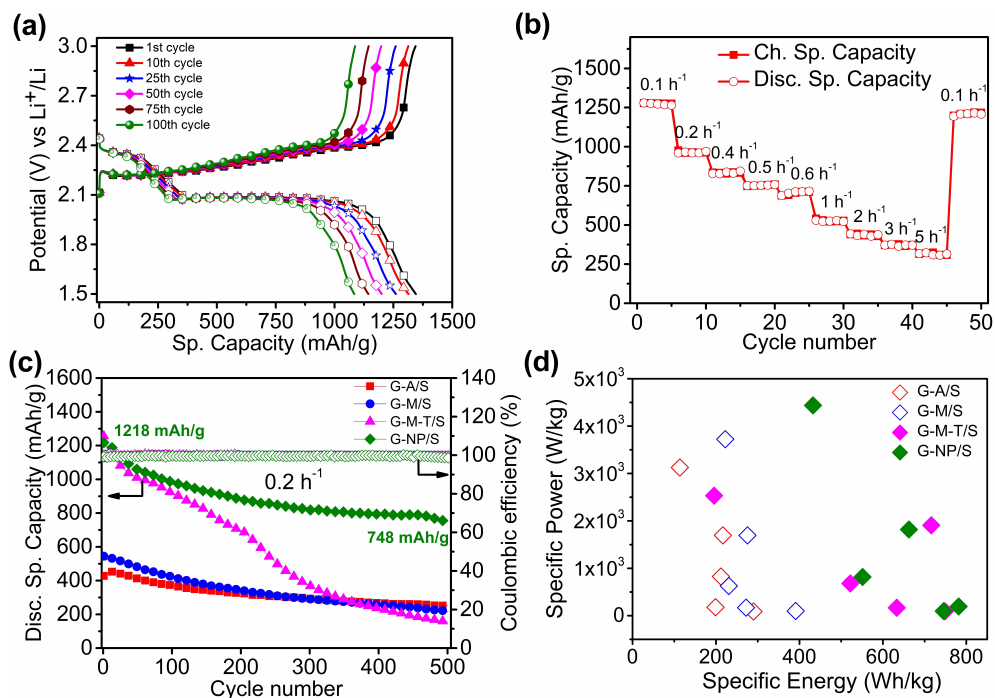


Figure 5. Charge-discharge profile at 0.2 h⁻¹ (a) and rate performance of Li-S cell comprising G-NP (b). Plot showing variation in specific capacity for 500 cycles 0.2 h⁻¹ (c). Ragone plot of Li-S batteries with various DLC-Gs (d).

(5 h⁻¹). Immediately after cycling at 5 h⁻¹, the experiment was conducted at 0.1 h⁻¹. In this experiment, the specific capacity bounced back to 1214 mAh g⁻¹ (Figure 5b). The loss of specific capacity is a mere 6% while going from 0.1 to 0.1 h⁻¹ through 0.2, 0.4, 0.5, 0.6, 1, 2, 3 and 5 h⁻¹. The data corroborates our hypothesis that the Ni ions on the layer of graphene withhold the polysulfide during the charge-discharge cycling experiments. To further study the cycling stability of G-NP based batteries, they were subjected to five hundred charge-discharge cycles. The G-NP based batteries' specific capacity decreased by 39% and the exact value of specific capacity was 748 mAh g⁻¹ (Figure 5c). Contrary to this, G-M-T based batteries exhibited initial specific capacity comparable to that of G-NP based batteries. However, at the end of five hundred charge-discharge cycles, the absolute specific capacity was 156 mAh g⁻¹, which is 4.7 times lower than that observed for G-NP based batteries. The decrease is a massive 88% for G-M-T based batteries. In the case of G-M and G-A based batteries, the initial specific capacity was low. Their specific capacity fading over 500 charge-discharge cycling is also comparable. G-M batteries show a slightly better performance than the G-A based batteries. The performance enhancement in case of G-M-T based batteries at the beginning of charge discharge experiment is impressive. But the fading in specific capacity as a function of cycle number is very high. Thus, the overall battery performance of G-M-T batteries is moderate. However, the overall performance of G-NP based batteries is very impressive. From the available data, we computed Ragone plot by calculating specific power and energy. The G-A and G-M based batteries showed very high specific power but exhibited poor specific energy. Contrary to this, the G-M-T and G-NP based batteries exhibited high specific energy. Specific energy equals the multiplication of cell voltage and amount of charge stored. The cell voltage is very close for all the batteries. However, the amount of charge stored is high for G-M-T and G-NP. Therefore, the batteries based on G-M-T and G-NP also showed high specific energy (Figure 5d). In addition, the batteries with G-NP exhibited high specific power (4437 W kg⁻¹) also. The specific energy is 782 Wh kg⁻¹ (Figure 5d).

3. Conclusions

In conclusion, we have developed an approach to prepare graphene with a layer comprising heteroatoms by employing a mechanical exfoliation process. The process utilizes exfoliators during the exfoliation of graphene from the pristine graphite. By judicious choice of exfoliator, DLC-G with nitrogen and DLC-G with nitrogen and sulfur are prepared. The battery with DLC-G comprising nitrogen and sulfur showed improved specific capacity compared to battery comprising DLC-G with nitrogen alone. However, the polysulfide dissolution is not suppressed. The DLC-G with Ni cations and nitrogen showed impressive specific capacity, power and energy density. This has been attributed to electrocatalysis facilitated by high percentage of pyridinic nitrogen. The suppression of sulfur dissolution is

attributed to electrostatic polyvalent attraction between Ni cations and polysulfide.

Experimental Section

Chemicals and materials

Graphite powder (Sigma-Aldrich, < 20 μm), Melamine (Alfa Aesar, 99%), Anthracene (Alfa Aesar, 99%), Ni-Phthalocyanine (Sigma-Aldrich, Dye content ca. 85%), 3-Thiopheneacetic acid (Sigma-Aldrich, 99%), Dimethylformamide (DMF, Merck, AR grade), Triton X-100 (Sigma-Aldrich, LR grade), Sodium thiosulfate (anhydrous, 99%), Hydrochloric acid (HCl, Merck, AR grade, 37%), Super P carbon (Imerys Graphite & Carbon Switzerland Ltd., Switzerland), polyvinylidene fluoride (PVDF, Kynar HSV900, Arkema Inc., USA), N-Methyl-2-pyrrolidone (NMP, Merck, AR grade), Celgard 2325 (Polypore, USA), Bis(trifluoromethane)sulfonimide lithium salt (LiTFSI, Sigma-Aldrich, 99.95%), Lithium nitrate (LiNO₃, Sigma-Aldrich, 99.99%), 1,3-dioxolane (DOL, Sigma-Aldrich, 99.8%), 1,2-dimethoxyethane (DME, Sigma-Aldrich, 99.5%) and Chloroform (Merck, AR grade) were purchased and used without further purification.

Exfoliation of graphite

The few-layer Graphene was prepared through a mechanical exfoliation process using the planetary mill (FRITSCH, PULVERISETTE 6). The graphite powder was exfoliated using various exfoliating agents such as Melamine, Anthracene and Ni-Phthalocyanine (Scheme S1).

Samples 1–4

Graphite powder (1.5 g) and Melamine (7.5 g) were placed in an Agate ball mill grinder (250 mL) with six balls (1 cm diameter). The ball milling conditions are mentioned in Table S2 for respective samples. The as-prepared material was washed with a copious amount of Dimethylformamide (DMF) for an hour to remove the excess amount of melamine present in it and filtered and dried at 60 °C under vacuum for 16 h.

Samples 5–8

Graphite powder (1.5 g) and Anthracene (7.5 g) were chosen and followed the same procedure, and the milling conditions were mentioned in Table S2.

Samples 9–12

Graphite powder (1.5 g) and Ni-Phthalocyanine (7.5 g) were used and followed the same procedure and the milling conditions were mentioned in Table S2.

Synthesis of G-M, G-M-T, G-A and G-NP

G-M was obtained by carbonizing sample 4 at 600 °C under an Argon atmosphere for 4 h with the heat flow of 5 °C min⁻¹. For G-M-T, Sample 4 (9 g) was further ball milled with 3-Thiophene acetic acid (4.5 g) for 60 min with the speed of 200 rpm, washed with DMF, filtered and dried at 60 °C under vacuum for 16 h. Then carried out for carbonization at 600 °C under an Argon atmosphere for 4 h with the heat flow of 5 °C min⁻¹. G-A was obtained by carbonizing sample 8 at 600 °C under an Argon atmosphere for 4 h

with heat flow of $5^{\circ}\text{C min}^{-1}$. For G-NP, Sample 12 was carbonized at 600°C under an Argon atmosphere for 4 h with the heat flow of $5^{\circ}\text{C min}^{-1}$.

Synthesis of sulfur composite materials

The Sulfur particles were synthesized by the wet chemical process. In this method, 9 mL of Triton X-100 (1 wt%) was added into aqueous sodium thiosulfate (300 mL, 0.05 M) and the solution was heated at 70°C , followed by 10% HCl solution (30 mL) was slowly added into the above solution under vigorous magnetic stirring. The suspension of doped layer comprising graphene (DLC-G) (72 mg) in 100 mL of de-ionized water, was added drop-wise under magnetic stirring. After 15 min, the solution was cooled down to room temperature, filtered under vacuum with a copious amount of de-ionized water, dried at 60°C for 16 h.

Material characterizations

The TEM images were recorded with Tecnai G2 20 S-TWIN transmission electron microscope and HRTEM images were recorded with a Jeol 1200 EX transmission electron microscope. The carbon-coated copper grids (400 grids) were obtained from Ted Pella. E-SEM images were recorded using Quanta 200 and FESEM images were recorded with Nova Nano 450, both the instruments from the FEI company. The sample preparation for TEM and SEM were performed by preparing the 1 mg of sample dispersed in DMF and drop cast on the carbon-coated copper grid and silicon wafer are respectively. After the solvent evaporation, the substrates were kept at 40°C for 12 h and then performed the characterizations. The Raman spectroscopy measurements were performed with the help of a LabRam spectrometer (HJY, France) equipped with a laser wavelength of 632 nm. PANalytical instrument was operated using $\text{Cu } K_{\alpha}$ radiation ($\lambda = 1.542 \text{ \AA}$) at a scanning rate of $2^{\circ} \text{ min}^{-1}$ and a step size of 0.02° in 2θ with operating voltage 40 kV and operating current 30 mA to acquire the X-ray diffraction spectra. XPS measurements for the materials were done on Thermo Kalpha+ spectrometer using $\text{Al } K_{\alpha}$ radiation with an energy of 1486.6 eV. All the spectra were charge corrected with reference to C1s at 284.6 eV. The peak fittings were carried out using CasaXPS software. Thermogravimetric analyzes were carried out on SDTQ600 TG-DTA analyzer in a nitrogen environment with a ramp of $5^{\circ}\text{C min}^{-1}$.

Electrochemical measurements

The sulfur composite materials were used for battery application. The slurry for the cathode was prepared using the DLC-G, Super P carbon and PVDF are mixed with the mass ratio of 60:30:10, in N-methyl-2-pyrrolidone (NMP) solvent. The slurry was coated onto carbon-coated aluminium foil, allowed to dry at room temperature and dried at 60°C for 16 h. The above-prepared electrode was used as a working electrode, Li foil as counter and reference electrode and Celgard 2325 as separator (Thickness $25 \mu\text{m}$). 1.0 M LiTFSI in 1,3-dioxolane and 1,2-dimethoxyethane (volume ratio 1:1) and 0.4 M LiNO_3 was used as an electrolyte. The 2032 type coin cells were fabricated in an Argon filled glovebox (MBRAUN, $\text{O}_2 < 0.1 \text{ ppm}$, $\text{H}_2\text{O} < 0.1 \text{ ppm}$). The cyclic voltammetry was carried out using a multichannel Autolab MAC80038 instrument with the potential range of 1.5–3.0 V and the charge-discharge at the various current rate was carried out using the Neware battery testing system. All the electrochemical tests were carried out at 25°C . Graphically, the Specific energy (Wh kg^{-1}) was calculated from area under the discharge curve and Specific power (W kg^{-1}) was calculated by specific energy/time (h) of the discharge curve.

Symmetrical cell assembly and tests

A 0.2 M Li_2S_6 solution was prepared by dissolving elemental sulfur and Li_2S (5:1 molar ratio) in a mixture of DOL and DME (volume ratio of 1:1) under vigorous stirring at 50°C . The symmetrical cells were fabricated using identical DLC-Gs. The cells were assembled inside an Argon filled glovebox and CV tests were conducted for the symmetric cells with potential window of -1 to 1 V at 5 mV s^{-1} .

Acknowledgements

K.K. thanks Science and Engineering Research Board for financial support (EMR/2016/004732). S.K. thanks Department of Science and Technology for Inspire fellowship.

Conflict of Interest

The authors declare no conflict of interest.

Keywords: Electrocatalysis · graphene · mechanical exfoliation · polyvalent interaction · lithium-sulfur battery

- [1] P. g. Bruce, S. A. Freunberger, L. J. Hardwick, J.-M. Tarascon, *Nat. Mater.* **2012**, *11*, 19–29.
- [2] a) A. Manthiram, S.-H. Chung, C. Zu, *Adv. Mater.* **2015**, *27*, 1980–2006; b) A. Manthiram, Y. Fu, S.-H. Chung, C. Zu, Y.-S. Su, *Chem. Rev.* **2014**, *114*, 11751–11787; c) Y.-X. Yin, S. Xin, Y.-G. Guo, L.-J. Wan, *Angew. Chem. Int. Ed.* **2013**, *52*, 13186–13200; *Angew. Chem.* **2013**, *125*, 13426–13441; d) J. Kim, D.-J. Lee, H.-G. Jung, Y.-K. Sun, J. Hassoun, B. Scrosati, *Adv. Funct. Mater.* **2013**, *23*, 1076–1080; e) A. Rosenman, E. Markevich, G. Salitra, D. Aurbach, A. Garsuch, F. F. Chesneau, *Adv. Energy Mater.* **2015**, *5*, 1500212; f) F. Cerdas, P. Titscher, N. Bognar, R. Schmich, M. Winter, A. Kwade, C. Herrmann, *Energies* **2018**, *11*, 150; g) Y. Zhang, P. Zhang, S. Zhang, Z. Wang, N. Li, S. R. P. Silva, G. Shao, *InfoMat.* **2021**, *3*, 790–803; h) C. Zhang, L. Cui, S. Abdolhosseinzadeh, J. Heier, *InfoMat.* **2020**, *2*, 613–638; i) Y.-X. Yao, X.-Q. Zhang, B.-Q. Li, C. Yan, P.-Y. Chen, J.-Q. Huang, Q. Zhang, *InfoMat.* **2020**, *2*, 379–388; j) Z. Wei, Y. Ren, J. Sokolowski, X. Zhu, G. Wu, *InfoMat.* **2020**, *2*, 483–508; k) Y. Dai, W. Zheng, X. Li, A. Liu, W. Zhang, X. Jiang, X. Wu, J. Tao, G. He, *ACS Appl. Mater. Interfaces* **2021**, *13*, 2521–2529; l) X. Li, Y. Zhang, S. Wang, Y. Liu, Y. Ding, G. He, N. Zhang, G. Yu, *Nano Lett.* **2020**, *20*, 701–708; m) Y. Liu, X. Li, Y. Liu, W. Kou, W. Shen, G. He, *Chem. Eng. J.* **2020**, *382*, 122858.
- [3] a) C. Liang, N. J. Dudney, J. Y. Howe, *Chem. Mater.* **2009**, *21*, 4724–4730; b) S. S. Zhang, *J. Power Sources* **2013**, *231*, 153–162.
- [4] a) J. Liang, Z.-H. Sun, F. Li, H.-M. Cheng, *Energy Storage Mater.* **2016**, *2*, 76–106; b) S. Jeong, D. Bresser, D. Buchholz, M. Winter, S. Passerini, *J. Power Sources* **2013**, *235*, 220–225; c) J. Schuster, G. He, B. Mandlmeier, T. Yim, K. T. Lee, T. Bein, L. F. Nazar, *Angew. Chem. Int. Ed.* **2012**, *51*, 3591–3595; *Angew. Chem.* **2012**, *124*, 3651–3655; d) X. Ji, K. T. Lee, L. F. Nazar, *Nat. Mater.* **2009**, *8*, 500–506.
- [5] a) A. Manthiram, Y. Fu, Y.-S. Su, *Acc. Chem. Res.* **2013**, *46*, 1125–1134; b) M. Li, J. E. Frerichs, M. Kolek, W. Sun, D. Zhou, C. J. Huang, B. J. Hwang, M. R. Hansen, M. Winter, P. Bieker, *Adv. Funct. Mater.* **2020**, *30*, 1910123; c) Y. V. Mikhaylik, J. R. Akridge, *J. Electrochem. Soc.* **2004**, *151*, A1969.
- [6] S.-H. Chung, A. Manthiram, *Adv. Mater.* **2014**, *26*, 7352–7357.
- [7] H. Yao, K. Yan, W. Li, G. Zheng, D. Kong, Z. W. Seh, V. K. Narasimhan, Z. Liang, Y. Cui, *Energy Environ. Sci.* **2014**, *7*, 3381–3390.
- [8] a) H. M. Kim, H.-H. Sun, I. Belharouak, A. Manthiram, Y.-K. Sun, *ACS Energy Lett.* **2016**, *1*, 136–141; b) B. Zhang, X. Qin, G. R. Li, X. P. Gao, *Energy Environ. Sci.* **2010**, *3*, 1531–1537; c) N. Jayaprakash, J. Shen, S. S. Moganty, A. Corona, L. A. Archer, *Angew. Chem. Int. Ed.* **2011**, *50*, 5904–5908; *Angew. Chem.* **2011**, *123*, 6026–6030.
- [9] a) X. Liang, C. Hart, Q. Pang, A. Garsuch, T. Weiss, L. F. Nazar, *Nat. Commun.* **2015**, *6*, 5682; b) Y. Tsao, Z. Chen, S. Rondeau-Gagné, Q.

- Zhang, H. Yao, S. Chen, G. Zhou, C. Zu, Y. Cui, Z. Bao, *ACS Energy Lett.* **2017**, *2*, 2454–2462; c) Y. Yang, G. Yu, J. J. Cha, H. Wu, M. Vosgueritchian, Y. Yao, Z. Bao, Y. Cui, *ACS Nano* **2011**, *5*, 9187–9193.
- [10] Z. Wu, W. Wang, Y. Wang, C. Chen, K. Li, G. Zhao, C. Sun, W. Chen, L. Ni, G. Diao, *Electrochim. Acta* **2017**, *224*, 527–533.
- [11] a) G. Zheng, Q. Zhang, J. J. Cha, Y. Yang, W. Li, Z. W. Seh, Y. Cui, *Nano Lett.* **2013**, *13*, 1265–1270; b) H. Wang, Y. Yang, Y. Liang, J. T. Robinson, Y. Li, A. Jackson, Y. Cui, H. Dai, *Nano Lett.* **2011**, *11*, 2644–2647.
- [12] a) C. Zu, A. Manthiram, *Adv. Energy Mater.* **2013**, *3*, 1008–1012; b) J. S. Lee, A. Manthiram, *J. Power Sources* **2017**, *343*, 54–59; c) H. Chen, C. Wang, Y. Dai, S. Qiu, J. Yang, W. Lu, L. Chen, *Nano Lett.* **2015**, *15*, 5443–5448; d) P. Shi, Y. Wang, X. Liang, Y. Sun, S. Cheng, C. Chen, H. Xiang, *ACS Sustainable Chem. Eng.* **2018**, *6*, 9661–9670; e) Y. Xie, Z. Meng, T. Cai, W.-Q. Han, *ACS Appl. Mater. Interfaces* **2015**, *7*, 25202–25210; f) D. Liu, C. Zhang, G. Zhou, W. Lv, G. Ling, L. Zhi, Q.-H. Yang, *Adv. Sci.* **2018**, *5*, 1700270.
- [13] a) A. Gomez-Martin, J. Martinez-Fernandez, M. Rutttert, M. Winter, T. Placke, J. Ramirez-Rico, *Carbon* **2020**, *164*, 261–271; b) P. Zhu, J. Song, D. Lv, D. Wang, C. Jaye, D. A. Fischer, T. Wu, Y. Chen, *J. Phys. Chem. C* **2014**, *118*, 7765–7771; c) F. Pei, T. An, J. Zang, X. Zhao, X. Fang, M. Zheng, Q. Dong, N. Zheng, *Adv. Energy Mater.* **2016**, *6*, 1502539.
- [14] V. León, M. Quintana, M. A. Herrero, J. L. g. Fierro, A. d l Hoz, M. Prato, E. Vázquez, *Chem. Commun.* **2011**, *47*, 10936–10938.
- [15] V. León, A. M. Rodriguez, P. Prieto, M. Prato, E. Vázquez, *ACS Nano* **2014**, *8*, 563–571.
- [16] a) C. Teng, D. Xie, J. Wang, Z. Yang, G. Ren, Y. Zhu, *Adv. Funct. Mater.* **2017**, *27*, 1700240; b) Y. Dong, S. Zhang, X. Du, S. Hong, S. Zhao, Y. Chen, X. Chen, H. Song, *Adv. Funct. Mater.* **2019**, *29*, 1901127.
- [17] Q. Pang, L. F. Nazar, *ACS Nano* **2016**, *10*, 4111–4118.
- [18] a) G. Zhou, E. Paek, G. S. Hwang, A. Manthiram, *Nat. Commun.* **2015**, *6*, 7760; b) J. Balach, H. K. Singh, S. Gomoll, T. Jaumann, M. Klose, S. Oswald, M. Richter, J. Eckert, L. Giebeler, *ACS Appl. Mater. Interfaces* **2016**, *8*, 14586–14595; c) X. Y. Zhou, Q. C. Liao, T. Bai, J. Yang, *J. Mater. Sci.* **2017**, *52*, 7719–7732.
- [19] L. Kong, B.-Q. Li, H.-J. Peng, R. Zhang, J. Xie, J.-Q. Huang, Q. Zhang, *Adv. Energy Mater.* **2018**, *8*, 1800849.
- [20] a) S. Niu, W. Lv, C. Zhang, F. Li, L. Tang, Y. He, B. Li, Q.-H. Yang, F. Kang, *J. Mater. Chem. A* **2015**, *3*, 20218–20224; b) M. Zhang, C. Yu, J. Yang, C. Zhao, Z. Ling, J. Qiu, *J. Mater. Chem. A* **2017**, *5*, 10380–10386; c) J.-L. Shi, C. Tang, J.-Q. Huang, W. Zhu, Q. Zhang, *J. Energy Chem.* **2018**, *27*, 167–175.
- [21] D. M. Koshy, S. Chen, D. U. Lee, M. B. Stevens, A. M. Abdellah, S. M. Dull, G. Chen, D. Nordlund, A. Gallo, C. Hahn, D. C. Higgins, Z. Bao, T. F. Jaramillo, *Angew. Chem. Int. Ed.* **2020**, *59*, 4043–4050; *Angew. Chem.* **2020**, *132*, 4072–4079.
- [22] A. Eckmann, A. Felten, A. Mishchenko, L. Britnell, R. Krupke, K. S. Novoselov, C. Casiraghi, *Nano Lett.* **2012**, *12*, 3925–3930.
- [23] a) G. George, S. B. Sisupal, T. Tomy, B. A. Pottammal, A. Kumaran, V. Suvekbala, R. Gopimohan, S. Sivaram, L. Ragupathy, *Carbon* **2017**, *119*, 527–534; b) G. George, S. B. Sisupal, T. Tomy, A. Kumaran, P. Vadivelu, V. Suvekbala, S. Sivaram, L. Ragupathy, *Sci. Rep.* **2018**, *8*, 11228.
- [24] R. Blume, D. Rosenthal, J.-P. Tessonnier, H. Li, A. Knop-Gericke, R. Schlögl, *ChemCatChem* **2015**, *7*, 2871–2881.
- [25] a) W. Li, J. Qian, T. Zhao, Y. Ye, Y. Xing, Y. Huang, L. Wei, N. Zhang, N. Chen, L. Li, F. Wu, R. Chen, *Adv. Sci.* **2019**, *6*, 1802362; b) J. He, Y. Chen, A. Manthiram, *iScience* **2018**, *4*, 36–43.
- [26] D. Tian, X. Song, M. Wang, X. Wu, Y. Qiu, B. Guan, X. Xu, L. Fan, N. Zhang, K. Sun, *Adv. Energy Mater.* **2019**, *9*, 1901940.
- [27] L. Zhang, D. Liu, Z. Muhammad, F. Wan, W. Xie, Y. Wang, L. Song, Z. Niu, J. Chen, *Adv. Mater.* **2019**, *31*, 1903955.
- [28] a) R. Wang, C. Luo, T. Wang, G. Zhou, Y. Deng, Y. He, Q. Zhang, F. Kang, W. Lv, Q.-H. Yang, *Adv. Mater.* **2020**, *32*, 2000315; b) Z. Liang, D. Yang, P. Tang, C. Zhang, J. Jacas Biendicho, Y. Zhang, J. Llorca, X. Wang, J. Li, M. Heggen, J. David, R. E. Dunin-Borkowski, Y. Zhou, J. R. Morante, A. Cabot, J. Arbiol, *Adv. Energy Mater.* **2021**, *11*, 2003507; c) J. He, A. Bhargava, A. Manthiram, *ACS Nano* **2021**, *15*, 8583–8591.

Manuscript received: August 28, 2021

Revised manuscript received: October 18, 2021

Accepted manuscript online: October 25, 2021

Version of record online: November 15, 2021